Università degli Studi di Pisa

Facoltà di Scienze Matematiche, Fisiche e Naturali

Scuola di Dottorato in Fisica "G. Galilei"

Phd Thesis

Study of the decay channel $K^{\pm} \to e^{\pm}\nu\pi^0\gamma$ at NA48/2

SUPERVISOR

Prof. **Flavio Costantini**

CANDIDATE

Stefano Venditti

(XX Ciclo)

Academic year 2007-2008

It is a capital mistake to theorize before one has data. Insensibly one begins to twist facts to suit theories, instead of theories to suit facts.

Sir Arthur Conan Doyle, *A scandal in Bohemia*, 1891.

Contents

Introduction

Since the discovery of the K meson in the '40s, the kaon system has played a fundamental role in modern particle physics. In the neutral kaon (K_L, K_S) system CP violation in the mixing was observed for the first time in 1964, by Christenson, Cronin, Fitch and Turlay [1], while starting from the 90's the NA31 [2] and afterwards the NA48 [3] and KTeV [4] experiments detected and measured for the first time a CP violation in the decay amplitude $(\epsilon^{'}/\epsilon)$, also known as direct CP violation. More recently a new upper limit on direct CP violation in the charged kaon system was established by the NA48/2 Collaboration.

Besides CP violation effects, whose presence was also detected in the B system by the BaBar and Belle collaborations [5][6] in the late 90's, many other measurements can be carried out in the neutral and charged kaon systems. The recent high-statistics experiments, in fact, allow precise measurements of the branching ratios (BR) and decay form factors of many decays and the estimation of fundamental parameters of the Standard Model (SM), as CKM matrix elements. Predictions of theories beyond the SM can also be tested, thus beginning a task which will be exhaustively addressed by LHC's experiments in the next future.

The perspectives of kaon physics go towards the measurement of ultra-rare decays, as $K^{\pm} \to \pi^{\pm}\nu\bar{\nu}$ and $K_L \to \pi^0\nu\bar{\nu}$: since these two decays can be evaluated with a high precision from a theoretical point of view, their measurement would allow to perform a stringent test on the validity of the SM and, at the same time, to have the first measurement of the V_{td} element of the CKM matrix [7].

A new experiment focused on $K^{\pm} \to \pi^{\pm}\nu\bar{\nu}$ decay, recently named NA62 and previously known as P326, is in the R&D phase, the bulk of the collaboration being that of NA48/2.

The present thesis is focused on the analysis of the decay $K^{\pm} \to e^{\pm}\nu\pi^0\gamma$. The data analyzed were collected by the NA48/2 experiment in 2003 and 2004, using simultaneous high intensity K^+ and K^- beams. The statistics available using these data allows a significative improvement on the BR measurement and on the parameters correlated to this channel. In particular a test on the validity of T symmetry can be performed once the momenta of the three detectable particles are reconstructed.

This thesis is organized as follows:

- In Chapt. 1 the aim of the present work is described. The first part recalls discrete symmetries in particle physics and the description of the most important experiments which led to the discovery of P and CP violation in weak decays; in the second part the quantities to be measured will be introduced from a theoretical point of view;

- Chapt. 2 is devoted to the description of NA48/2 experimental apparatus, the trigger chain and the data-taking periods;
- In Chapt. 3 the quantities already introduced in Chapt. 1 are related to the experimental quantities which can be measured using NA48/2 data and the corresponding Monte Carlo (MC) simulation;
- Chapt. 4 describes the selection cuts applied to tag the Ke3γ and Ke3 events; the cuts specifically used to isolate the signal from the background will be discussed in Chapt. 6, where a precise estimation of the residual background is also performed;
- In Chapt. 5 the NA48/2 MC is described: here the generation procedure of MC events used in the analysis is described and MC distributions are compared to real data, to cross-check the simulation;
- Chapt. 7 is devoted to the trigger issues related to the measurements performed, while in Chapt. 8 the estimation of systematic effects is discussed;
- Finally, in Chapt. 9 the obtained results are presented.

Chapter 1

Physical motivations

The first topic addressed in this chapter is the definition of the discrete symmetries C, P and T in particle physics; the attention will then focus on the violation of the CP symmetry in the SM and in particular in the kaon system. The physics goals of the NA48/2 experiment will be then discussed. The attention will finally focus on the decay mode investigated in this thesis, i.e. the channel $K^{\pm} \to e^{\pm}\nu\pi^{0}\gamma$, and on the physical quantities that can be measured by selecting these events among the data collected by NA48/2 in 2003-2004.

1.1 Continuous and discrete symmetries

The main aim of physics has always been to find laws that could synthesize in the simplest way the widest number of observed phenomena, even if at a first glance they could appear different among them. The idea of synthesis was first conceived in Greek philosophy. Heraclitus, for example:

Joints are at once a unitary whole and not a unitary whole. To be in agreement is to differ, the concordant is the discordant. From many things comes oneness, and out of oneness come the many things.

The presence of a continuous symmetry in a theory, i.e. the invariance of the theory with respect to one of its variables, represents one of the finest examples of this synthesis: indeed it can be shown through the Noether theorem that the conservation of a physical quantity stems out from this invariance, and characterizes the evolution of the whole system, even if the initial and final physical states are totally different. So, for example, the invariance of a theory with respect to space translations gives as a consequence the conservation of momentum for every system which can be interpreted according to that theory; in the same way invariance with respect to time translations leads to the conservation of energy. The concept of continuous symmetry, first conceived in the framework of classical physics, can be easily adapted to quantum physics, where the Noether theorem still holds.

A difference arises when one considers *discrete symmetries*, which are by definition not continuously connected with the identity transformation I, i.e. one cannot find for them an infinitesimal transformation $T(\epsilon)$ such that, for $\epsilon \to 0$, $T(\epsilon) \to I$. In this case no physical quantity is conserved in the evolution of the system, but the system can be associated with a quantum number which does not change if the symmetry is conserved.

We shall now briefly review three important discrete symmetries that can be defined in particle physics:

- **P Symmetry**: The parity operation involves the inversion of the spatial coordinates: $\vec{x} \to -\vec{x}$. Vectors and scalars can be classified according to their behaviour with respect to this transformation: a *pseudo-vector* is a vector whose sign is left unchanged by the parity operation, while a *vector* changes its sign. An example of a pseudo-vector is the angular momentum $\vec{L} = \vec{R} \wedge \vec{P}$, where $\vec{P}$ is the momentum, while the position $\vec{R}$ is the simplest example of a vector. In the same way a *pseudo-scalar* is a scalar changing sign under the parity operation, while a *scalar* is unaffected.

  In particle physics, particles are classified as scalars, pseudoscalars, vectors or pseudovectors. These names refer to the quantum fields which represent the particles and that can be either scalar or vector fields, showing the behaviour described above under parity.

  Parity was shown to be a good symmetry for strong and electromagnetic interactions, i.e. the physics of these processes is invariant under the parity operation. However parity is violated in weak interactions, as will be discussed further on.

- **C Symmetry**: This symmetry has not an equivalent in classical physics, as it involves the exchange of a particle with its antiparticle, whose existence cannot be accounted for outside the framework of quantum field theory. A theory which is invariant under C symmetry implies that the equations of motion are invariant if the place of the particle's quantum field is taken by that of its antiparticle. The C operation involves the change of several quantum numbers, like charge, baryon and lepton number or strangeness: not all neutral particles, but only some of them, coincide with their antiparticles. In this case not only the equations of motion are left unaffected by the C symmetry, but also the fields. Examples of particles coinciding with their antiparticles are the π^0 meson and the photon.

  The charge conjugation symmetry is conserved by electromagnetic and strong interactions, but is again violated by weak interactions.

- **T Symmetry**: The T operation involves the time inversion: $t \to -t$. This means, for example, that for velocity $\vec{v} = d\vec{x}/dt \to -\vec{v}$, while the force, defined as $\vec{F} = d\vec{P}/dt \to \vec{F}$, remains unchanged.
  The time reversal, however, also requires the exchange between initial and final state of the system. So the invariance of a particle system with respect to T is related to whether, taking the final state of a process and reversing the velocities of all particles, one can obtain the initial state with all velocities reversed. However this kind of experiment turns out to be not realizable, as it is impossible to exactly reproduce the final state of an interaction, expecially when several particles are produced. So, in order to test T-symmetry one has to rely on some quantities which can be measured with final state particles and are constrained by requiring T-symmetry. The mathematical transformation implying time inversion is usually referred to as $\hat{T}$: not in all cases a $\hat{T}$-violation means a T-violation, as will be discussed later on.

Regarding the above discrete symmetries, under very general assumptions, the so called CPT theorem can be proved; it states that the combination of C, P and T symmetries is a good symmetry of a theory if:

- The theory is Lorentz-invariant;
- The theory is local;
- The Hamiltonian of the theory is Hermitian;
- There is a state of minimum energy.

One straightforward consequence is that, for a theory where CPT symmetry holds, a T-symmetry violation implies a CP violation as well, and viceversa.

Until the half of the 20th century, the validity of P symmetry was assumed by physicists, as it was considered to be a symmetry of space itself; in 1956, however, the problem was addressed by a theoretical paper by C.N. Yang and T.D. Lee [8]. This theoretical analysis was triggered by the famous $\theta - \tau$ puzzle: in those years, in fact, two particles having compatible masses and lifetimes but decaying to two states with opposite parity were observed and named respectively θ and τ:

$$\theta^+ \to \pi^+\pi^0$$

$$\tau^+ \to \pi^+\pi^+\pi^-$$

For the θ^+ the possible values for L^P, where L is the total orbital angular momentum and P the parity, can be shown to be necessarily in the sequence 0^-,2^-,4^-... and so on, while for the τ^+ the possible values are 0^+,1^-,2^+... These could be decay modes of the same particle in two states with different parity, but this required parity to be violated in weak interactions. Yang and Lee proposed a series of experiments to verify parity conservation. The first experiment detecting P-violation in weak decays was carried out in the same year by C.S. Wu et al. [9], who showed that in the β-decay of polarized Co nuclei:

$$^{60}Co \rightarrow ^{60} Ni^* + e + \nu \qquad ^{60}Ni^* \rightarrow ^{60} Ni + \gamma(1.173 \text{ MeV}) + \gamma(1.332 \text{ MeV})$$

the positron emission was not isotropic. A key-point of the experiment, whose schematic view is shown in fig. 1.1, was the polarization of Cobalt nuclei by a magnetic field using the Rose-Gorter method, which implies cooling the Cobalt sample. The amount of polarization was monitored through the anysotropy of photons coming from the de-excitation of the Ni nucleus. A sizable asymmetry in the positron distribution was observed, and it was also seen that this asymmetry disappeared as the Co nuclei depolarized when temperature increased.

Within few days other experiments confirmed the violation of P and C symmetry in weak interactions. The outcome of these experiments was in agreement with the so-called V-A form of the weak currents, where the P and C violation were given by the simultaneous presence of a vector (V) and an axial (A) current:

$$J^{\alpha}(x) = J^{\alpha}_{V}(x) - J^{\alpha}_{A}(x) \tag{1.1}$$

where:

$$J^{\alpha}_{V}(x) = \sum_{l} \bar{\psi}_l(x)\gamma^{\alpha}\psi_{\nu_l}(x) \qquad J^{\alpha}_{A}(x) = \sum_{l} \bar{\psi}_l(x)\gamma^{\alpha}\gamma_5\psi_{\nu_l}(x) \tag{1.2}$$

and l is the lepton index (=e, μ, τ). Under parity transformation $J^{\alpha}_{V}(x)$ changes sign, $J^{\alpha}_{A}(x)$ does not. This equal mixture of vector and axial terms is such that the weak current (1.1) maximally violates the two symmetries C and P. The most important consequence is for neutrinos: assuming they have zero mass, the quantity $(1-\gamma^5)/2$ can be shown to be a helicity projection operator. This implies that only negative helicity ("left handed") neutrinos and positive helicity ("right handed") antineutrinos take part in weak interactions, while right-handed neutrinos and left-handed antineutrinos cannot interact at all.

Once the experiments demonstrated that P and C symmetries were violated, physicists hoped that at least CP symmetry, i.e. the transformation of all particles into their respective antiparticles coupled with a parity transformation, could be preserved. This idea stood until 1964, when the experiment realized by Christenson, Cronin, Fitch and Turlay [1] showed that the long-lived neutral kaon could decay to final states with different CP values.

The experiment, carried out at Brookhaven National Laboratories and sketched in fig. 1.2, was performed by impinging a 30 GeV proton beam on a Beryllium target, selecting the neutral particles coming out of the interaction and detecting

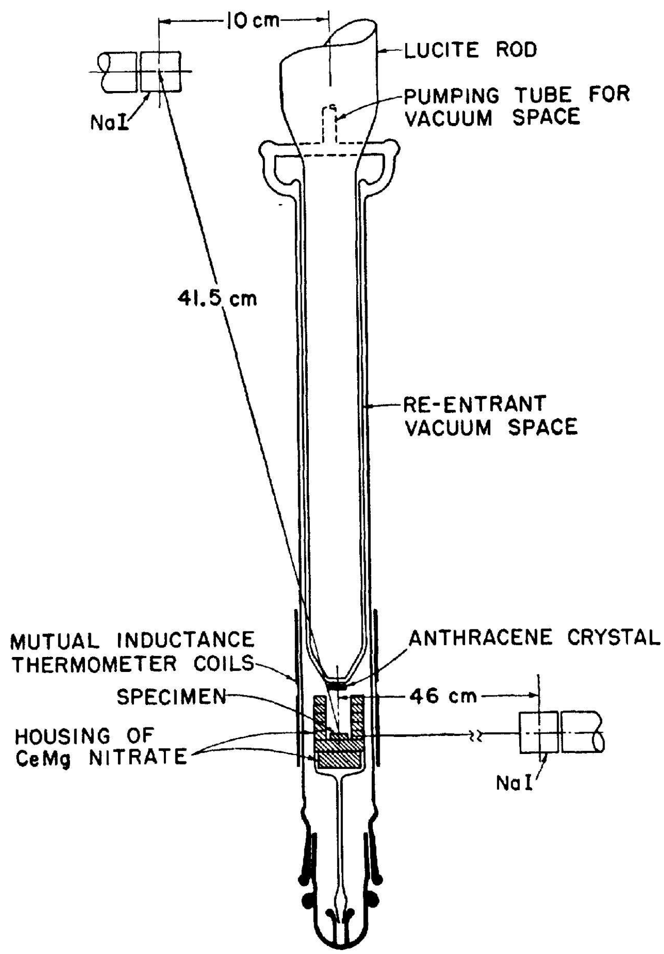

Figure 1.1: Sketch of Wu's experiment on P-symmetry violation.

their decay products. In case the mass eigenstates coincide with the CP eigenstates, the CP=1 eigenstate can only decay to the $\pi^+\pi^-$ mode, while the CP=-1 eigenstate can only decay to the $\pi^+\pi^-\pi^0$ mode; because of phase space considerations, the former decay has a much smaller decay length than the latter, and as a consequence after few cm's one should see only $\pi^+\pi^-\pi^0$ final states. However, the result of the experiment was the observation of the two-body decay $K^0 \to \pi^+\pi^-$; this means that the physical states must be written as a combination of different CP eigenstates, i.e. CP is not a conserved quantum number for weak interactions. This implies CP violation in weak decays, the consequences of which will be exposed in the next section, where theoretical issues of CP violation will be addressed.

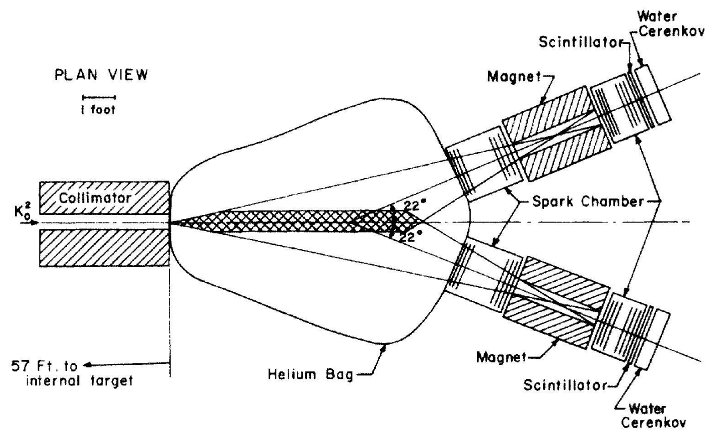

Figure 1.2: Plain view of the detector used by Christenson et al.

1.2 CP violation in the SM

In this section the origin of CP violation within the SM framework will be investigated; the different ways in which CP violation can manifest itself in a particle system will be then described.

1.2.1 CP violation and the CKM matrix

The Standard Model of strong and electroweak interactions is a non-abelian gauge theory based on the $SU(3)_C \times SU(2)_L \times U(1)_Y$ symmetry group. The $SU(3)_C$ subgroup is the symmetry of strong interactions; on the other hand, the $SU(2)_L \times U(1)_Y$ is the subgroup of electro-weak interactions. The invariance request on the fields with respect to the transformations given by these groups leads to the introduction of boson gauge fields mediating the interactions: gluons for strong interactions, $W^{\pm}$ and Z^0 for weak interactions, γ for electromagnetism. For an introduction to the electroweak Lagrangian and gauge mechanism see for example [10].

The mass part of the Lagrangian for quark and lepton masses can be written as:

$$\mathcal{L}^{eff}_{mass} = \bar{U} M_U U + \bar{D} M_D D + \bar{L} M_L L \tag{1.3}$$

where:

$$U = \begin{pmatrix} u & c & t \end{pmatrix} \qquad D = \begin{pmatrix} d & s & b \end{pmatrix} \qquad L = \begin{pmatrix} e & \mu & \tau \end{pmatrix} \tag{1.4}$$

and $M_U = diag\{m_u, m_c, m_t\}$, $M_D = diag\{m_d, m_s, m_b\}$, $M_L = diag\{m_l, m_\mu, m_\tau\}$ are the mass matrices and neutrinos are assumed to be massless.

The fermion fields appearing in the interaction part of the electroweak Lagrangian are not in general mass eigenstates, i.e. they do not coincide with those written in eq. 1.4; introducing the unitary matrices V_U, V_D and V_L the weak-interacting states can be written as:

$$\begin{pmatrix} u^1 & u^2 & u^3 \end{pmatrix} = V_U U \qquad \begin{pmatrix} d^1 & d^2 & d^3 \end{pmatrix} = V_D D \qquad \begin{pmatrix} l^1 & l^2 & l^3 \end{pmatrix} = V_L L$$

i.e. they are rotated with respect to the mass states. In this way in the interaction part of the electroweak Lagrangian a matrix of the form $\mathrm{V}_U^\dagger \mathrm{V}_D$ will appear (see [11]), which is commonly called the Cabibbo-Kobayashi-Maskawa matrix:

$$V_U^\dagger V_D = V_{CKM} = \begin{pmatrix} V_{ud} & V_{us} & V_{ub} \\ V_{cd} & V_{cs} & V_{cb} \\ V_{td} & V_{ts} & V_{tb} \end{pmatrix}$$

A necessary condition in order to have CP violation is the presence of weak amplitudes with different weak phases. This is the same as requiring in the electroweak Lagrangian complex coupling constants which:

- cannot be canceled by a redefinition of field phases;
- leave $\mathcal{L}_{ew}$ Hermitian.

It can be shown that the only possible coupling constants of $\mathcal{L}_{ew}$ satisfying these conditions are the matrix elements of ${V_U}^\dagger V_D$.

The first form of the CKM matrix dates back to almost 50 years ago. In the early 60's N. Cabibbo, in order to explain the experimental fact that, at quark level, flavour-changing decays had a much smaller amplitude than decays with no flavour changing, introduced a rotation between the flavour eigenstates (i.e. the mass states produced in strong interactions) and the weak interaction eigenstates of the quarks [12]. At that time only 3 quarks (i.e. u, d and s) where known, so the rotation involved d and s quarks in the coupling to u quark. After the hypothesis of a fourth quark, introduced by the GIM mechanism [13], the rotation between flavour and weak eigenstates could be written in terms of a 2×2 matrix:

$$M_C = \begin{pmatrix} \sin\theta_C & \cos\theta_C \\ \cos\theta_C & -\sin\theta_C \end{pmatrix} \qquad S_{mass} = M_C S_{flavour} \tag{1.5}$$

In 1973 Kobayashi and Maskawa [14] proposed the extension of the model in the case of three quark families, thus theorizing the present shape of the CKM matrix. Notably this was done before the experimental discovery of the c quark, in 1974 [15][16].

In the general case of N_f quark families, the CKM matrix is a $N_f \times N_f$ unitary matrix. The number of phases n_P and real parameters n_R needed to define such a matrix are:

$$n_P = \frac{N_f(N_f+1)}{2} \qquad n_R = \frac{N_f(N_f-1)}{2}$$

However, since $2N_f - 1$ phases of the $2N_f$ quarks are arbitrary, the non trivial phases in a N_f-dimensional CKM matrix are:

$$n_P{}^{real} = n_P - 2N_f + 1 = \frac{(N_f-1)(N_f-2)}{2}$$

In the case of 2 families, the CKM matrix is defined by one real parameter (the Cabibbo angle) and no phases. With the presence of 3 quark families, the definition of the CKM matrix requires 3 real parameters and 1 phase: it is thanks to the presence of this phase that CP (and T, as a consequence of CPT theorem) violation can take place in the SM. It is important to stress that the presence of 3 quark families and the mixing between strong and weak eigenstates of the quarks are both necessary, but not sufficient conditions for the presence of CP violation.

One of the most common parametrizations of the CKM matrix is the so-called Wolfenstein expansion [17]: it allows to write the matrix in terms of the four parameters A, ρ, η and λ (the Cabibbo angle), which is used as the expansion parameter. Neglecting $O(\lambda^5)$ terms it can be written as:

$$V_{CKM} = \begin{pmatrix} 1-\frac{\lambda^2}{2} & \lambda & A\lambda^3(\rho - i\eta(1-\frac{\lambda^2}{2})) \\ -\lambda & 1-\frac{\lambda^2}{2} - i\eta A^2\lambda^4 & A\lambda^2(1+i\eta\lambda^2) \\ A\lambda^3(1-\rho-i\eta) & -A\lambda^2 & 1 \end{pmatrix} \tag{1.6}$$

While the parameters A ($0.818^{+0.007}_{-0.017}$) and λ (0.2272 ± 0.0010) are relatively well known, ρ ($0.221^{+0.064}_{-0.028}$) and η ($0.340^{+0.017}_{-0.045}$) [18] are much more uncertain: the aim of CP-violation experiments is to overconstraint this two parameters to perform a test of the SM and look for possible new physics.

The presence of CP violation is usually shown using the so-called unitarity triangles. These are the triangles obtained in the complex plane by representing the unitarity conditions of the CKM matrix, i.e. the six off-diagonal relations given by $V^\dagger_{CKM}V_{CKM}$=1:

$$V_{ud}V^*_{us} + V_{cd}V^*_{cs} + V_{td}V^*_{ts} = 0 \qquad V_{us}V^*_{ub} + V_{cs}V^*_{cb} + V_{ts}V^*_{tb} = 0$$

$$V_{ud}V^*_{ub} + V_{cd}V^*_{cb} + V_{td}V^*_{tb} = 0 \qquad V_{ud}V^*_{cd} + V_{us}V^*_{cs} + V_{ub}V^*_{cb} = 0$$

$$V_{cd}V^*_{td} + V_{cs}V^*_{ts} + V_{cb}V^*_{tb} = 0 \qquad V_{ud}V^*_{td} + V_{us}V^*_{ts} + V_{ub}V^*_{tb} = 0$$

CP violation is realized only if the common area of these triangles is different from zero. With the Wolfenstein parametrization, sides and angles of the triangle

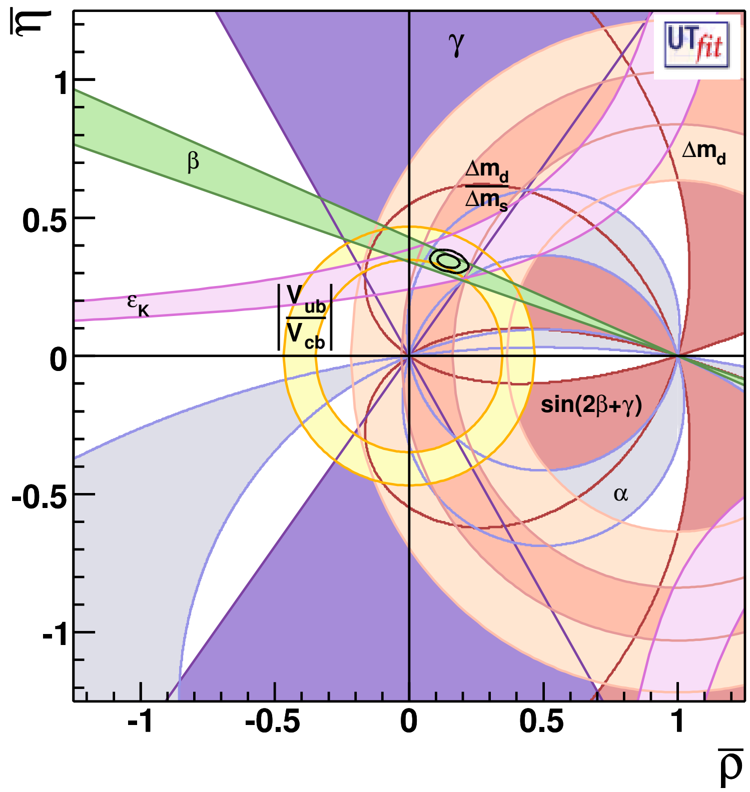

Figure 1.3: Fit of a unitarity triangle's vertices using constraints from different experiments.

can also be computed in terms of the parameters mentioned above. In particular the area can be expressed as:

$$J \sim \lambda(1 - \frac{\lambda^2}{2})A^2\lambda^5\eta \tag{1.7}$$

which directly connects CP violation to the presence of an irreducible phase (η) in the CKM matrix. An example of vertex fitting of a unitary triangle through experimental measurements is shown in fig. 1.3.

The latest results for the elements of the CKM matrix, according to the PDG [18] are:

$$V_{CKM} = \begin{pmatrix} 0.9736 \text{ to } 0.97407 & 0.2262 \text{ to } 0.2282 & 0.00387 \text{ to } 0.00405 \\ 0.2261 \text{ to } 0.2281 & 0.97272 \text{ to } 0.9732 & 0.04141 \text{ to } 0.04231 \\ 0.0075 \text{ to } 0.00846 & 0.04083 \text{ to } 0.04173 & 0.999096 \text{ to } 0.999134 \end{pmatrix} \tag{1.8}$$

1.2.2 Types of CP violation

According to the last section, CP violation can occur in a given process only if at least two amplitudes with different weak phases exist. Indeed under the application of the CP operator (i.e. considering the amplitude for the antiparticle) weak phases ϕ_j, (i.e. phases showing opposite signs in the transition amplitude for a process and in the transition amplitude for the CP-conjugate process) change their sign, while strong phases (i.e. phases showing same signs in the transition amplitude for a process and in the transition amplitude for the CP-conjugate process) are left unaffected. The total amplitudes A_f, $\bar{A}_{\bar{f}}$ can be written as:

$$< f|T|i >= A_f = \sum_j A_j e^{i\phi_j} e^{i\delta_j} \overset{CP}{\rightarrow} \sum_j A_j e^{-i\phi_j} e^{i\delta_j} = \bar{A}_{\bar{f}} =< \bar{f}|T|\bar{i} > \tag{1.9}$$

where T represents the transition matrix, i and f the initial and final state and the sum is over all the possible transition amplitudes between i and f.

The ways in which CP violation can take place inside the SM will be briefly reviewed [11]:

- **CP violation in mixing**: It happens when the eigenstates of the weak interaction are not the same as the CP eigenstates. This is the case, for example, of the neutral kaon system, where CP violation was first discovered (see section 1.1). It can be detected by looking at the decay of two weak eigenstates P_1 and P_2, which can be expressed in terms of the same CP eigenstates, and that decay in the same final state *f*. An asymmetry parameter can be computed:

$$a = \frac{\Gamma(P \rightarrow f) - \Gamma(\bar{P} \rightarrow f)}{\Gamma(P \rightarrow f) + \Gamma(\bar{P} \rightarrow f)}$$

  If a is different from 1 an *indirect CP violation* is detected.

- **CP violation in the decay (Direct CP violation)**: It takes place when there is a difference in the partial decay amplitude between a particle and its antiparticle. An asymmetry parameter can be defined as:

$$a = \frac{\Gamma(P \rightarrow f) - \Gamma(\bar{P} \rightarrow \bar{f})}{\Gamma(P \rightarrow f) + \Gamma(\bar{P} \rightarrow \bar{f})} = \frac{1 - |\bar{A}_{\bar{f}}/A_f|^2}{1 + |\bar{A}_{\bar{f}}/A_f|^2} \tag{1.10}$$

  where the ratio of the two amplitudes is given by:

$$|\frac{\bar{A}_{\bar{f}}}{A_f}| = |\frac{\sum_j A_j e^{-i(\phi_j - \delta_j)}}{\sum_j A_j e^{i(\phi_j + \delta_j)}}| \tag{1.11}$$

It can be shown starting from eq. 1.11 that, for this type of CP violation, both the weak and strong phases of the amplitudes involved must be different. Direct CP violation can happen also in charged mesons, where mixing is forbidden because of electric charge conservation.

- **CP violation in the interference**: This type of CP violation, which was the first to be measured in the neutral B system, can occur if two weak eigenstates decay to a common CP eigenstate. Calling $\lambda_f = q\cdot\bar{A}_{\bar{f}}/p\cdot A_f$ (where q and p are the coefficients expressing weak eigenstates as a function of strong eigenstates, i.e. of P and $\bar{P}$ mesons), its signature is given by $Im\lambda_f \neq 0$; this is different from the direct CP violation, which happens if $|\lambda_f| \neq 1$. One way to detect this effect is to compute the time dependent parameter $A_{CP}(t)$ defined as:

$$A_{CP}(t) = \frac{\Gamma(P(t) \to f_{CP}(t)) - \Gamma(\bar{P}(t) \to f_{CP}(t))}{\Gamma(P(t) \to f_{CP}(t)) + \Gamma(\bar{P}(t) \to f_{CP}(t))} = a^{dir}\cos\Delta mt + a^{int}\sin\Delta mt \tag{1.12}$$

A non-zero value for $a^{int} = \frac{2Im\lambda_f}{1+|\lambda_f|^2}$ implies the presence of CP violation in the interference.

1.3 NA48/2 physics

Following NA31 and NA48, which analyzed the neutral kaon decays and measured direct CP violation in this sector, the NA48/2 experiment addressed the study of charged kaon properties with unprecedented precision and statistical power. The main goal of the new experiment was the study of direct CP violation's effect in the decays $K^\pm \to \pi^\pm\pi^+\pi^-$ and $K^\pm \to \pi^\pm\pi^0\pi^0$ by looking at the Dalitz plot distribution in the positive and negative modes, fitting them with a parametrization of the matrix element and looking for possible differences between the two charge modes. This difference is expressed in terms of the charge asymmetry parameters A_g^c and A_g^n, which are in turn proportional to the difference of the Dalitz plot slopes $\mathrm{g}_{c,n}^+$ and $\mathrm{g}_{c,n}^-$ between positive and negative mode:

$$A_g^{c,n} = \frac{g_{c,n}^+ - g_{c,n}^-}{g_{c,n}^+ + g_{c,n}^-} \simeq \frac{\Delta g_{c,n}}{2g_{c,n}} \tag{1.13}$$

The final result, published in 2007 [19], improves the previous limit by a factor 10 and excludes the presence of CP violation in these channels at 10^{-4} level, with an error dominated by statistics:

$$A_g^c = (-1.5 \pm 2.2)\cdot 10^{-4} \qquad (K^\pm \to \pi^\pm\pi^+\pi^-) \tag{1.14}$$

$$A_g^n = (1.8 \pm 1.8)\cdot 10^{-4} \qquad (K^\pm \to \pi^\pm\pi^0\pi^0) \tag{1.15}$$

The SM prediction for CP violating effects for $A_g^{c,n}$ in $K^\pm \to \pi^\pm\pi^+\pi^-$ and $K^\pm \to \pi^\pm\pi^0\pi^0$ is in the range 10^{-5}-10^{-6} [20] [21].

Besides the test of direct CP violation in 3π decays, the data collected by NA48/2 allow the measurement of branching ratios (BR) up to 10^{-9}, and the possibility to measure correlated quantities, as form factors and CP-violating parameters. Some examples besides the physics case presented in this thesis are:

- form factors of Ke4 decay ($K^\pm \to \pi^+\pi^-e^\pm\nu$), which allow the measurement of the pion $a_0 - a_2$ scattering lengths [22];
- The effect of $\pi^+\pi^-$ strong interaction in $K^\pm \to \pi^\pm\pi^0\pi^0$ decay channel, providing an alternative way to measure pion scattering lengths [23];
- Ke3 ($K \to e^\pm\nu\pi^0$) decay, allowing the measurement of the V_{us} element of the CKM matrix [24];
- Kpi2γ ($K \to \pi^\pm\pi^0\gamma$) decay, where the BR can be measured and the direct emission contribution to the amplitude can be estimated [25];
- Ke2 ($K \to e^\pm\nu$) decay, where the BR measurement can give hints on the presence of new physics [26],[27].

1.4 The $K^\pm \to e^\pm\nu\pi^0\gamma$ decay

The present work addresses the analysis of the channel $K^\pm \to e^\pm\nu\pi^0\gamma$ (Ke3γ). The physical quantities which can be measured in this decay will be exposed. Finally the potential improvement on these measurements using NA48/2 data set will be discussed in relation to the values reported in the 2006 edition of the PDG.

1.4.1 Kinematics of the $K^\pm \to e^\pm\nu\pi^0\gamma$ decay

The decay is characterized by 4 particles in the final state; this implies 5 degrees of freedom, i.e. 5 independent kinematical variables are needed to describe the whole process. A possible choice of these variables is:

E_e	CM charged lepton energy;
E_{π^0}	CM Pion energy;
E_γ	CM Photon energy;
$W = \sqrt{(p_e + p_\nu)^2}$	Absolute value of the sum of lepton and neutrino 4-momenta;
$X = \frac{p_e \cdot p_\gamma}{M^2{}_K}$	Scalar product of electron and photon 4-momenta.

As mentioned in the next section, the inner bremsstrahlung (IB) part of the amplitude is divergent in the limit $E_\gamma \to 0$. Moreover the angle between photon and lepton shows a “quasi-singularity”, i.e. a singularity in the limit $m_e \to 0$. This means that the BR measurement must be performed with suitable cuts on these two variables and compared with theoretical predictions which are dependent on these cuts. Bearing this in mind, the mentioned kinematical variables are quite useful because the values of E_γ and X can be directly related to the angle between electron and photon.

The total decay amplitude, integrating the squared module of the matrix element over the whole phase space and summing over all possible polarizations of the electron and photon, is:

$$\Gamma(K^\pm \to \pi^0 e^\pm \nu\gamma) = \frac{1}{2M_K(2\pi)^8}\int\sum_{spin}|T|^2 d_{PhSp}(E_{e^\pm}, E_{\pi^0}, E_\gamma, W, X) \tag{1.16}$$

Since the NA48/2 experimental apparatus does not allow to measure the total kaon flux, the computed BR will be normalized to a reference channel, which is usually chosen in such a way that at least part of systematic uncertainties cancel in the ratio. For Ke3γ the most straightforward choice is the decay channel $K^\pm \to e^\pm\nu\pi^0$ (Ke3). The quantity to be measured is then:

$$R({E_\gamma}^{cut}, {\theta_{e\gamma}}^{cut}) = \frac{\Gamma(Ke3\gamma, E_\gamma > {E_\gamma}^{cut}, \theta_{e\gamma} > {\theta_{e\gamma}}^{cut})}{\Gamma(Ke3)} \tag{1.17}$$

The Ke3 amplitude includes radiative soft photons, whose presence, as discussed in Chapt. 5, has been accounted for in the analysis.

In the following chapters it will be discussed how experimental quantities (acceptances, trigger efficiencies, background) must be considered while computing R.

1.4.2 Ke3γ decay amplitude

For the decay analyzed:

$$K^\pm \to \pi^0(p')e^\pm(p_e)\nu_e(p_\nu)\gamma(q) \tag{1.18}$$

The matrix element has the form [28]:

$$T = \frac{G_f}{\sqrt{2}} e V_{us}^* \epsilon^\mu(q)^* \times [(V_{\mu\nu} - A_{\mu\nu})\bar{u}(p_\nu)\gamma^\nu(1-\gamma^5)v(p_e) +$$
$$+\frac{F_\nu}{2p_e q}\bar{u}(p_\nu)\gamma^\nu(1-\gamma^5)(m_e - \not{p}_e - \not{q})\gamma_\mu v(p_e)] = \epsilon^\mu(q)^* M_\mu \tag{1.19}$$

where G$_f$ is the Fermi constant, e the electron charge, V$_{us}$ the proper CKM matrix element, ϵ^μ the photon polarization vector, $\bar{u}$ and v the the neutrino and electron spinors, γ^ν the Dirac matrices and F$_\nu$ the Ke3 matrix element, whose presence will be discussed in a while.

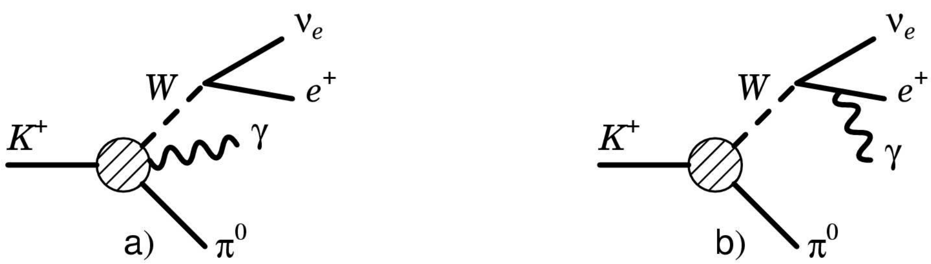

Figure 1.4: Feynman diagrams corresponding to different kinds of photon emission in the Ke3γ decay.

The matrix element is made of two parts, the first representing the K photon emission and all the intermediate hadronic states of the decay, while the second represents the photon emission by the charged lepton. A sketch of the Feynman diagrams is shown in fig. 1.4.

The first term is expressed through the hadronic tensors $V_{\mu\nu}$ and $A_{\mu\nu}$, defined as:

$$I_{\mu\nu} = i \int d^4x e^{iqx} < \pi^0(p') \mid T[V_\mu{}^{em}(x) I_\nu{}^{had}(0)] \mid K^+(p) > \qquad I = V, A \tag{1.20}$$

where:

$$V_\nu{}^{had} = \bar{s}\gamma_\nu u \qquad A_\nu{}^{had} = \bar{s}\gamma_\nu\gamma^5 u \tag{1.21}$$

$$V_\mu^{em} = (2\bar{u}\gamma_\mu u - \bar{d}\gamma_\mu d - \bar{s}\gamma_\mu s)/3 \tag{1.22}$$

The tensors $V_{\mu\nu}$ e $A_{\mu\nu}$ satisfy Ward identities:

$$q^\mu V_{\mu\nu} = F_\nu \qquad q^\mu A_{\mu\nu} = 0 \tag{1.23}$$

which follow from gauge invariance of the total amplitude:

$$q^\mu M_\mu = 0 \tag{1.24}$$

In the second term of equation (1.19) the matrix element of the decay $K^\pm \rightarrow e^\pm \nu \pi^0$ (Ke3) appears:

$$F_\nu = < \pi^0(p') \mid V_\nu{}^{had}(0) \mid K^+(p) > \tag{1.25}$$

The decay amplitude can be rewritten isolating the inner bremsstrahlung (IB) and the direct emission (DE) contributions. The IB terms, which represent the part of the amplitude non-vanishing (and in particular divergent) for small photon momenta, are given, according to Low's theorem [29], in terms of the Ke3 form factors f_+, f_1, defined by:

$$F_\nu(t) = \frac{1}{\sqrt{2}}[2p'_\nu f_+(t) + (p-p')_\nu f_1(t)] \qquad t = (p-p')^2 \tag{1.26}$$

This distinction implies a corresponding splitting in the hadronic tensors $A_{\mu\nu}$, $V_{\mu\nu}$. The axial part of this term is exclusively made of direct emission parts, and can be expressed in terms of four scalar functions A_i, i=1,...4:

$$A_{\mu\nu} = \frac{i}{\sqrt{2}}[\epsilon_{\mu\nu\rho\sigma}(A_1 p'^\rho q^\sigma + A_2 q^\rho W^\sigma) + \epsilon_{\mu\lambda\rho\sigma} p'^\lambda q^\rho W^\sigma (\frac{A_3}{{M_K}^2 - W^2} W_\nu + A_4 p'_\nu)] \tag{1.27}$$

The vector correlator $V_{\mu\nu}$ must be rewritten as:

$$V_{\mu\nu} = {V_{\mu\nu}}^{IB} + {V_{\mu\nu}}^{DE} \tag{1.28}$$

where the IB part is chosen in such a way that:

$$q^\mu {V_{\mu\nu}}^{IB} = F_\nu(t) \qquad q^\mu {V_{\mu\nu}}^{DE} = 0 \tag{1.29}$$

and can be written, according to the Low theorem, in terms of the Ke3 form factors f_+ and f_1.

The DE part of the Ke3γ matrix element can be defined as:

$$T^{DE} = \frac{G_f}{\sqrt{2}} e V^*_{us} \epsilon^\mu(q)^* (V^{DE}_{\mu\nu} - A_{\mu\nu}) \times \bar{u}(p_\nu)\gamma^\nu(1-\gamma^5)v(p_e) \tag{1.30}$$

where $V_{\mu\nu}$ can be expressed in terms of four scalar functions V_i, i=1,...4:

$$\begin{aligned} {V_{\mu\nu}}^{DE} = \frac{1}{\sqrt{2}}&[V_1(p'_\mu q_\nu - p'q g_{\mu\nu}) + V_2(W_\mu q_\nu - qW g_{\mu\nu}) + \\ &+ V_3(qWp'_\mu W_\nu - p'qW_\mu W_\nu) + V_4(qWp'_\mu p'_\nu - p'qW_\mu p'_\nu)] \end{aligned} \tag{1.31}$$

where W=p-p'-q.

The IB part is $T^{IB} = T - T^{DE}$.

1.4.3 Chiral perturbation theory

A thorough calculation of the Ke3γ matrix element makes use of the Chiral Perturbation Theory (ChPT). ChPT is an effective field theory whose Lagrangian is consistent with the chiral symmetry, as well as parity and charge symmetries; it allows to study the low-energy dynamics of QCD.

At low energy QCD becomes non-perturbative, so that it is impossible to extract information from partition functions. On the other hand, in the low-energy regime the degrees of freedom are no longer quarks and gluons, but hadrons, as the result of confinement. In other words, the energy is such that it does not probe the internal degrees of freedom (quarks and gluons) of hadrons. Neglecting light quark masses, the QCD Lagrangian can be written as:

$$\mathcal{L}_{QCD} = \sum_{q=u,d,s} \bar{q}\gamma^{\mu}(i\partial_{\mu} - g_s \frac{\lambda_a}{2} G^a_{\mu})q - \frac{1}{4} G^a_{\mu\nu} G^{a\mu\nu} + \text{heavy quark terms} \tag{1.32}$$

apart from $SU(3)_C$ invariance, this lagrangian has a global invariance under $SU(N_{lq})_L \times SU(N_{lq})_R \times U(1)_V \times U(1)_A$, where $N_{lq} = 3$ is the number of massless quarks. The $U(1)_V$ vector symmetry is exactly conserved even with non-vanishing quark masses and implies baryonic number conservation. The $U(1)_A$ axial symmetry, on the other hand, is explicitly broken at quantum level by the abelian anomaly [30] and thus does not correspond to any conserved quantity.

The group $G = SU(3)_L \times SU(3)_R$ (chiral symmetry) refers to the transformations:

$$\psi_{L,R} \xrightarrow{G} g_{L,R}\psi_{L,R} \qquad \text{where:} \qquad \psi = (u, d, s) \qquad g_{L,R} \in G \tag{1.33}$$

This symmetry is spontaneously broken: the subgroup which remains unbroken after the breaking of G is $H = SU(3)_V = SU(3)_{L+R}$. The eight Goldstone bosons corresponding to the eight generators of the broken symmetry can be interpreted, according to ChPT and in the limit $m_u = m_d = m_s = 0$ (chiral limit), as the meson octet of the famous "eightfold way theory" by Gell-Mann and Ne'eman [31], see fig. 1.5.

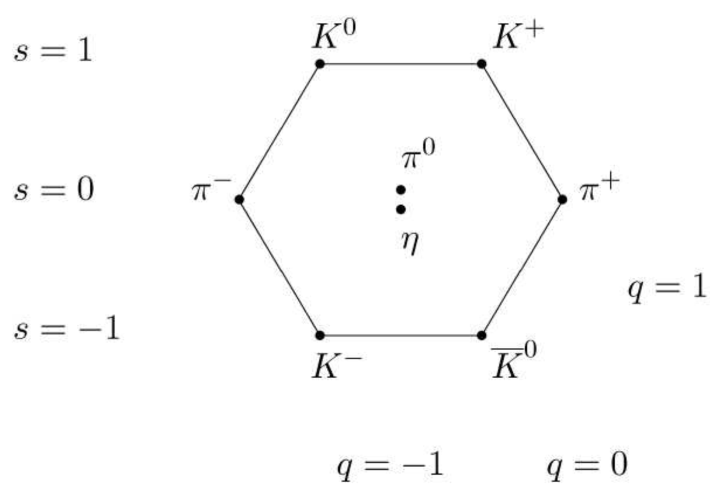

Figure 1.5: Meson octet from chiral symmetry breaking.

If real mesons were real Goldstone bosons, they should be massless; the fact that u, d and s quarks have a mass introduces in the theory terms which explicitly (not spontaneously) break G and H. Nevertheless, since $m_{u,d,s} << \Lambda_\chi$, where Λ_χ is the typical hadronic scale ($\simeq$ 1 GeV, i.e. the proton mass), these mass terms are small and can be treated as perturbations.

In an effective theory one has to write in the Lagrangian all the terms compatible with the symmetries of the theory; in general there is an infinite number of terms meeting this requirement. So, in order to make predictions, a counting scheme must be adopted which allows to keep some terms and to negelct others. The most common choice in ChPT is the p-expansion, i.e. the expansion in terms of powers of the meson's momentum.

One of the problems connected with this procedure is that the Lagrangian obtained in this way is non-renormalizable; however it can be shown [32] that the theory is renormalizable at a given order in the chiral expansion.

1.4.4 T-odd correlation and search for new physics

T-odd variable definition

The decays of charged kaons can be used as an excellent system to study direct CP violation. Since these effects are predicted to be negligible within the SM, in particular in semileptonic decays, the investigation of these channels also provides a probe for CP-violating mechanisms beyond the SM, i.e. a test of the presence of new physics.

CP violating (CP-odd) observables can be either $\hat{T}$-odd, and then are CP$\hat{T}$-even, or $\hat{T}$-even, and then are CP$\hat{T}$-odd (the relation between T and $\hat{T}$ was exposed in par. 1.1). In the first case the common way to measure the violation is to build a T-odd observable A, i.e. a variable which changes sign under T inversion, and look for its expectation value. It is important to stress that an expectation value for A (or $\bar{A}$, i.e. the observable relative to the CP-conjugate process) which is different from 0 only implies a $\hat{T}$-violation, and not necessarily a T (and hence CP)-violation: this is because of the presence of some effects, dealt with in the next section, which oddly contribute to A without violating CP. The T-violation in a single channel can then be measured only by carefully subtracting these effects, which may not be a trivial task. What genuinely violates CP is the sum between the expectation value of this variable for a process and that for the CP-conjugate process, i.e. $< A > + < \bar{A} >$.

Observables belonging to the second case typically are partial-width asymmetries.

An example of a T-odd variable allowing T-violation tests is the measurement of the transverse polarization of the muon in the decays $K^\pm \to \mu^\pm \nu_\mu \pi^0$ ($K^\pm \to \mu^\pm \nu_\mu \gamma$), which is odd under time reversal [33].

In experiments where the lepton polarization is not accessible, a T-odd correlation can still be obtained as a triple scalar product ξ of three independent 3-momenta in decays with at least 4 particles in the final state, like $K^{\pm} \to \pi^{+}\pi^{-}e^{\pm}\nu_e$ or the channel under investigation in this thesis, $K^{\pm} \to e^{\pm}\nu\pi^0\gamma$, for which a T-odd variable ξ is defined as:

$$\xi = \frac{\vec{p_\gamma} \cdot (\vec{p_\pi} \times \vec{p_e})}{{M_K}^3} \tag{1.34}$$

A violation of T-invariance in this channel would manifest with ξ-odd contributions to the differential width $d\Gamma/d\xi$. This means that if the variable:

$$A_\xi = \frac{N_+ - N_-}{N_+ + N_-} \tag{1.35}$$

is computed, where N_+ and N_- are respectively the number of events where ξ takes a positive or negative value, $A_\xi \neq 0$ would mean the existence of (at least) a $\hat{T}$ violating effect. If this parameter is computed for both positive and negative decays (from now A_ξ values computed for positive and negative events will be called A_ξ^+ and A_ξ^- respectively) and their sum is non-zero, this means, according to what was said before, a genuine CP-violating effect. The data collected by the NA48/2 experiment in 2003/2004 allow this measurement, which has never been performed so far.

Non CP-violating contributions to A_ξ

Apart from CP-violating effects outside the SM, at least two other sources of non-zero A_ξ within the SM can be identified. While they appear through different processes (i.e. electromagnetic and strong interactions, respectively), their common result is to introduce imaginary parts in the decay amplitude.

- **Radiative corrections:** if the matrix element is computed at first loop order in the electromagnetic constant α, loop diagrams like the one shown in fig.1.6 arise. These are loop diagrams with intermediate photons, which contribute with an imaginary part to the total amplitude. Once the matrix element (containing now these electromagnetic higher-order corrections) is computed, it can be shown [34] that these imaginary parts lead to a non-zero A_ξ. The asymmetries computed respectively for the electron and muon channels are:

$$A_\xi(K^+ \to e^+\nu\pi^0\gamma) = -0.59 \times 10^{-4} \tag{1.36}$$

$$A_\xi(K^+ \to \mu^+\nu\pi^0\gamma) = 1.14 \times 10^{-4} \tag{1.37}$$

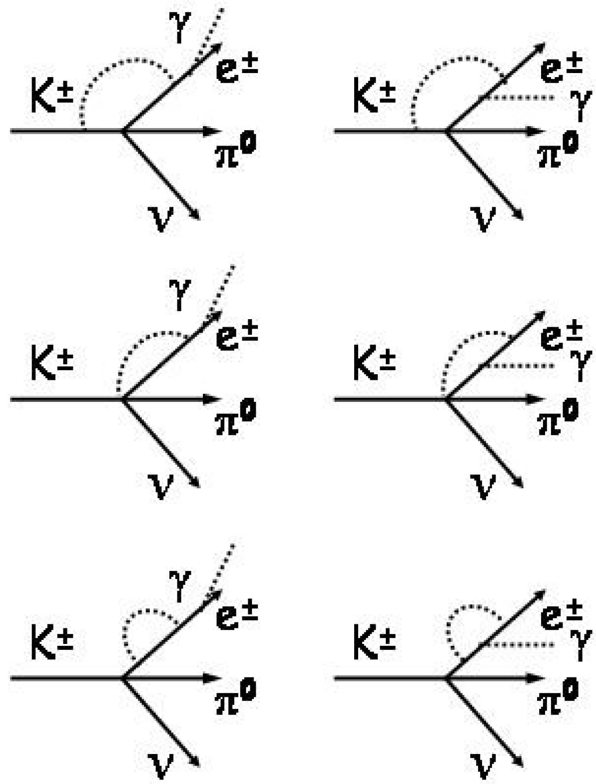

Figure 1.6: Final state interaction diagrams contributing to a non-zero value for A_ξ.

- **Imaginary parts in ChPT computation:** The computation of the DE part of the decay requires the use of ChPT. In particular ChPT was used to compute the structure functions V_i and A_i , introduced in the computation of the matrix element in (1.31). The technique is based on an expansion in terms of p^2 of the Lagrangian.

  The computation of the structure functions up to $\mathcal{O}(p^4)$ [35] yields all real quantities. For example for the A_i's one gets:

$$A_1 = -4A_2 = A_3 = -\frac{1}{2\pi^2 F^2}, \qquad A_4 = 0 \tag{1.38}$$

  where F is the neutral pion decay constant (= 130±5 MeV) . The reality of the structure functions implies that the squared matrix element does not contain terms proportional to ξ, hence no odd contributions to A_ξ are present at this order.

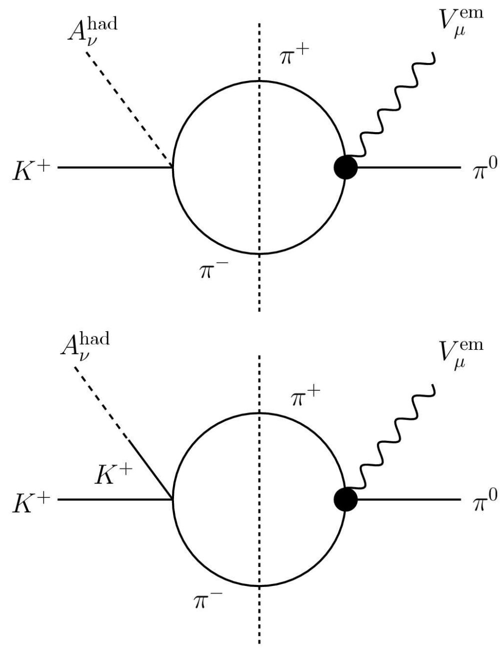

Figure 1.7: Diagrams contributing to $Im(A_i)$.

If the computation is performed up to $\mathcal{O}(p^6)$ order, the structure functions get an imaginary part [36]. For the A_i's the imaginary contribution comes from the one-loop diagrams in fig. 1.7, so that:

$$Im(A_1) = Im(A_3) = -\frac{s}{384\pi^3 F^4}(1 - \frac{4M_\pi^2}{s})^{\frac{3}{2}} \tag{1.39}$$

$$Im(A_2) = Im(A_4) = 0 \tag{1.40}$$

where $s = (p' + q)^2$. For what concerns the V_i's, the vector correlator $V_{\mu\nu}$ at this order can only receive contributions from two-loop (i.e. three pion) diagrams. In fig. 1.8a the general form of this diagram is shown, while in 1.8b and 1.8c there are, respectively, all the possible combinations for the coupling of the weak current and of the photon. The contribution to the imaginary parts is:

$$Im(V_i) = C_i \cdot \frac{1}{32768\pi^2\sqrt{3}F^4} \cdot \frac{s}{M_K^2 + 3M_\pi^2 - W^2}(1 - \frac{9M_\pi^2}{s})^4 \tag{1.41}$$

with:

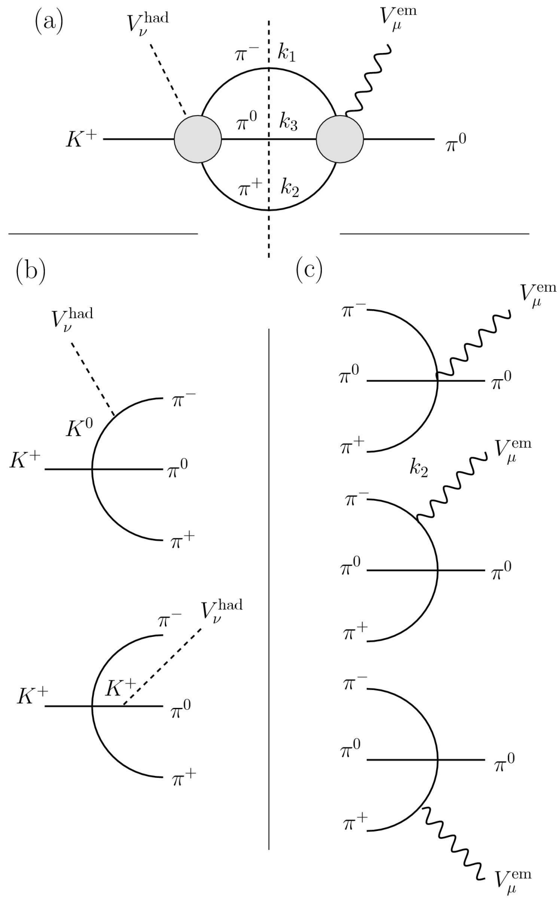

Figure 1.8: General form of the diagrams contributing to $\text{Im}(V_i)$ at $\mathcal{O}(p^6)$.In b) and c) all the possible combinations to form the diagram in a) are shown.

$$C_1 = \frac{1}{2}(s + t - M_K^2), \qquad C_2 = \frac{1}{2}(s + M_\pi^2), \tag{1.42}$$

$$C_3 = 0, \qquad C_4 = 1. \tag{1.43}$$

At level $\mathcal{O}(p^8)$ two-pion contributions to the V_i imaginary part arise: these contributions are sketched in fig. 1.9. Even though this contributions are at $\mathcal{O}(p^8)$ level, larger phase space and different threshold behaviour make them more sizeable with respect to those at $\mathcal{O}(p^6)$ level. They can be written as:

$$Im(V_i) = C_i \cdot \frac{s}{1536\pi^5 F^6}(1 - \frac{4M_\pi^2}{s})^{\frac{3}{2}} \tag{1.44}$$

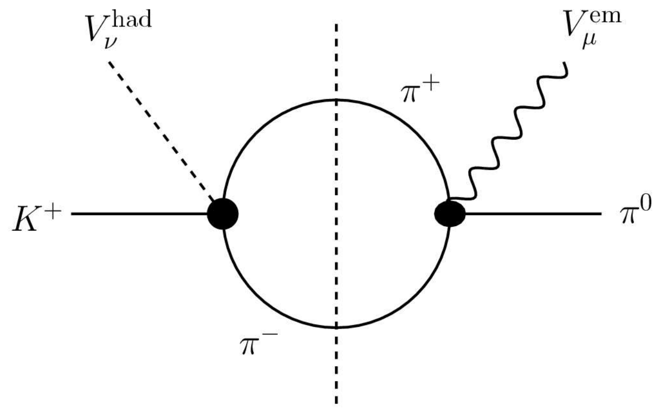

Figure 1.9: Diagram contributing to $\mathrm{Im}(V_i)$ at $\mathcal{O}(p^8)$ level.

The contributions to A_ξ coming from the diagrams described are shown in table 1.1 for Ke3γ and Kμ3γ; the single contributions coming from the terms $\mathrm{Im}(A_i)$ and $\mathrm{Im}(V_i)$ are also shown. By comparing them with 1.37 it is clear that the effect of ChPT-induced imaginary terms in the asymmetry is negligible compared to those coming from radiative corrections by about two orders of magnitude.

The absence of asymmetric effects on A_ξ within the SM up to 10^{-4} allows for a clean test of beyond-SM models predicting values of A_ξ different from 0 and higher than 10^{-4}. It is important to stress that the same test can be performed in the neutral channel ($K^0 \to \pi^\pm e^\mp \nu\gamma$): in this case, however, the final-state interaction contribution is much higher due to the presence of two charged particles.

If possible beyond-SM effects were of the same order or bigger than the asymmetric contributions exposed, their presence can be settled in the single channel. Otherwise the sum between A_ξ^+ and A_ξ^- can be considered: the latter yields a result which is independent from the theoretical knowledge of the asymmetric contributions, and only depends on the statistics available.

Beyond-SM values for A_ξ

In this section beyond-SM models predicting values different from 0 for A_ξ will be shortly reviewed. More information can be found in [37].

The model independent matrix element for the decay under analysis can be written as follows:

$$T = \frac{G_f}{\sqrt{2}} e V_{us}^* \epsilon^\mu(q)^* \times [((1+g_v)V_{\mu\nu} - (1-g_a)A_{\mu\nu})\bar{u}(p_\nu)\gamma^\nu(1-\gamma^5)v(p_e)+$$

A_i, V_i	$Ke3\gamma$	$K\mu3\gamma$
	A_ξ contributions ($Im(A_i)$)	
A_1	$1.4\cdot10^{-6}$	$4.5\cdot10^{-7}$
A_2	0	0
A_3	-	$-0.04\cdot10^{-7}$
A_4	0	0
A_ξ contributions ($Im(V_i)$, 2π at $\mathcal{O}(p^8)$)		
V_1	$-1.2\cdot10^{-7}$	$-3.1\cdot10^{-8}$
V_2	$-0.9\cdot10^{-7}$	$-4.2\cdot10^{-8}$
V_3	0	0
V_4	$-2.2\cdot10^{-7}$	$-0.2\cdot10^{-8}$
A_ξ contributions ($Im(V_i)$, 3π at $\mathcal{O}(p^6)$)		
V_1	$-0.8\cdot10^{-14}$	-
V_2	$-3.0\cdot10^{-14}$	-
V_3	-	-
V_4	$-6.6\cdot10^{-14}$	-
Total	$0.9\cdot10^{-6}$	$3.7\cdot10^{-7}$

Table 1.1: Contributions to A_ξ from non-vanishing imaginary parts of A_i and V_i in SM.

$$+(1+g_v)\frac{F_\nu}{2p_e q}\bar{u}(p_\nu)\gamma^\nu(1-\gamma^5)(m_e - \not{p}_e - \not{q})\gamma_\mu v(p_e)+ \tag{1.45}$$

$$+(g_s F_s^\mu + g_p F_p^\mu)\bar{u}(p_\nu)(1-\gamma^5)v(p_e) + \frac{g_s f}{2pq}\bar{u}(p_\nu)(m_e - \not{p}_e - \not{q})\gamma_\mu v(p_e)] \tag{1.46}$$

where g_s, g_p, g_v, g_a are the scalar, pseudoscalar, vector and pseudovector constants and:

$$F_s^\mu + \frac{p^\mu}{pq}f = i\int d^4x e^{iqx} < \pi^0(p') \mid T[V_\mu{}^{em}(x)\bar{s}u(0)] \mid K^+(p) > \tag{1.47}$$

$$F_p^\mu = i\int d^4x e^{iqx} < \pi^0(p') \mid T[V_\mu{}^{em}(x)\bar{s}\gamma_5 u(0)] \mid K^+(p) > \tag{1.48}$$

$$f =< \pi^0(p') \mid (\bar{s}u)(0) \mid K^+(p) > \tag{1.49}$$

This matrix element reduces to the SM one written in 1.19 for $g_s = g_p = g_v = g_a = 0$. In particular the coupling of the electroweak current with scalar hadronic currents is not present in 1.19.

The A_ξ computation using this matrix element yields:

$$A_\xi = -(2.9\times10^{-6}Im(g_s) + 3.7\times10^{-5}Im(g_p) + 3.0\times10^{-3}Im(g_v+g_a)) \tag{1.50}$$

which points out that a value different from 0 for A_ξ depends on the imaginary parts of the g constants being non-zero.

- **$\mathbf{SU(2)}_L \times \mathbf{SU(2)}_R \times \mathbf{U(1)}$ models:** in these models each generation of fermions is formed in $SU(2)_L$ and $SU(2)_R$ doublets. The Lagrangian of the model can be required to be invariant under transformations between left and right fields: this leads $SU(2)_L$ and $SU(2)_R$ fermion-boson couplings to be equal. In this case CP-violation appears due to left and right sectors of the model; the effect of CP-violation is more sizable than in the SM, since the analogue of the CKM matrix for the right sector contains $N(N+1)/2$ phases, where N is the number of fermion generations. The non-vanishing constants determining $|A_\xi| \neq 0$ are $\mathrm{Im}(g_v)$ and $\mathrm{Im}(g_a)$, i.e. the vector and pseudo-vector ones.

  The computed upper bounds for A_ξ are:

$$|A_\xi| < 2.6 \times 10^{-4} \qquad K^+ \to e^+\nu_e\pi^0\gamma \tag{1.51}$$

$$|A_\xi| < 0.8 \times 10^{-4} \qquad K^+ \to \mu^+\nu_\mu\pi^0\gamma \tag{1.52}$$

- **Models with scalar interaction:** In this models the non-zero asymmetry appears only due to the non-vanishing values of $\mathrm{Im}(g_s)$ and $\mathrm{Im}(g_p)$. Among these models there are some leptoquarks and multihiggs extensions.

  In these models the contribution to $|A_\xi|$ in Ke3γ decay is strongly suppressed with respect to Kμ3γ, because of the different fermion masses. For the latter, an upper limit has been derived:

$$|A_\xi| < 6.0 \times 10^{-6} \qquad K^+ \to \mu^+\nu_\mu\pi^0\gamma \tag{1.53}$$

The A_ξ asymmetry predicted by these models is out of reach using NA48/2 statistics; however the upper limit which will be computed in the present thesis will be a benchmark for other or future BSM theories.

1.5 Experimental measurements of R and A_ξ.

For what concerns the $R=\Gamma(\mathrm{Ke3}\gamma)/\Gamma(\mathrm{Ke3})$ measurement, the PDG 2007 reports the following value:

$$R = (0.54 \pm 0.04) \cdot 10^{-2} \tag{1.54}$$

This is the result of two measurements, namely the last two in table 1.2. Other results, not used for the computation of the quoted value, are also reported in the table. The IR applied cuts ($E^*_\gamma > 10$ MeV, $0.6 \leq \cos\theta^*_{e\gamma} \leq 0.9$) are however different

Author	Year	R($\times10^{-2}$)	E^*_γ cut	$\cos\theta^*_{e\gamma}$ cut	Events
Romano [39]	1971	(0.53 ± 0.22)	> 30 MeV	$\geq 0.6, \leq 0.9$	13
Romano [39]	1971	(0.76 ± 0.28)	> 10 MeV	$\geq 0.6, \leq 0.9$	13
Ljung [40]	1973	(0.48 ± 0.20)	> 30 MeV	≤ 0.9	16
Bolotov [41]	1986	(0.56 ± 0.04)	> 10 MeV	$\geq 0.6, \leq 0.9$	192
Barmin [42]	1991	(0.46 ± 0.08)	> 10 MeV	$\geq 0.6, \leq 0.9$	82

Table 1.2: $\Gamma(\mathrm{Ke3}\gamma)/\Gamma(\mathrm{Ke3})$ measurements through years.

from those used in this analysis, the reasons being that the latest theoretical as well as experimental results are based on these cuts.

The most recent result, published but not yet included on PDG, is from the ISTRA collaboration [38], which measured:

$$R = (0.64 \pm 0.02_{(stat)} \pm 0.03_{(syst)}) \cdot 10^{-2} \tag{1.55}$$

using the same IR cuts used in this analysis.

For what concerns A_ξ, the only measurement so far was performed by ISTRA on a sample of 1456 negative sign events, since the experiment only collected K^- decays:

$$A_\xi^- = -0.015 \pm 0.021 \tag{1.56}$$

and is not yet included in the PDG. It will be shown in the next chapters that the statistics available at NA48/2 in the 2003 and 2004 runs allows to select a much bigger Ke3γ event sample.

Chapter 2

The NA48/2 experimental setup

In this section the NA48/2 experimental apparatus will be described. The NA48/2 experiment is placed in the ECN3 hall in the North Area (hence NA) of the SPS, in the CERN site of Prevessin. The main detectors are those of the old NA48 experiment, with the only addition of KABES, a TPC detector used to measure momentum and position of incoming kaons, and of the Beam Position Monitor (also known as Pisa Monitor), a scintillator detector employed to monitor the beam position with a high resolution.

The description of the beam line and of the kaon selection will be addressed first, then all detectors will be described, with a particular care for those playing a fundamental role in the present analysis. Trigger setup and related issues will be dealt with at the end of the chapter and will be further discussed later in the following chapters.

A paper summarizing the experimental layout and technical solutions of the NA48 experiment (concerned with neutral kaon decays) has been recently published by the collaboration [43]: the reader can refer to this paper for all the detectors which were also used in the NA48/2 experiment.

2.1 Beam production and kaon selection

2.1.1 The SPS accelerator

The primary protons used to produce K beams in the NA48/2 experiment come from the Super Proton Sincrotron (SPS) accelerator; the 400 GeV proton nominal energy is reached through different stages of acceleration. The protons are created by a plasmatron source [44] and then accelerated up to 50 MeV by the Linac-2. A system of 4 vertically stacked small synchrotrons, called PS Booster (PSB), increases the proton energy up to 1.69 GeV and gives them a bunched shape. After this, the $3 \cdot 10^{13}$ protons per pulse arrive to the Proton Synchrotron (PS) accelerator, where their energy reaches 14 GeV. A 200 MHz radio frequency system allows to control the longitudinal emittance and the bunch properties.

The PS fills the SPS with 14 GeV, 5 ns spaced and 2 ns wide proton bunches. The protons are extracted from the SPS every 16.8 s through a non linear betatron resonance, which also allows to control the flux of the ejected particles.

It has to be mentioned that the SPS was used in the past as injector for the Large Electron Positron (LEP) and for the SppS (where Z_0 and $W^{\pm}$ were discovered); in the future it will also be used as the injector for the Large Hadron Collider (LHC). An overview of the CERN accelerator complex is shown in fig. 2.1

2.1.2 Kaon production and selection

The proton beam coming from the SPS, after being transported along a 800 m long beam line, impinges on a 400 mm long, 2 mm diameter beryllium target in the ECN3 hall of CERN Prevessin site. The $\sim 7 \cdot 10^{11}$ proton pulse has a flat top of 4.8 s, a period of 16.8 s and an energy of 400 GeV; protons hit the beryllium target with a 0 degree angle and produce through strong interaction several types of particles (protons, neutrons, muons, pions, kaons, electrons, photons).

A first collimator, placed 24 m from the target, defines the acceptance angle to be ± 0.36 mrad in both vertical and horizontal planes. Upstream of this collimator, neutral particles are dumped, while charged ones are selected in momentum by an achromat system of 4 dipole magnets with zero net deflection. The collimators placed in the middle of the achromat select for both signs a momentum band centered on 60 GeV/c and with a r.m.s. of 3.8%.

Once both K^+ and K^- beams are put back on the 0 degree line, they cross 4 quadrupoles, with the aim of focusing the beams with a convergence angle of ~ 0.04 mrad. This solution was preferred to the parallel beams in order to minimise any effect due to the width of the two beams: the two superimposed beams have a r.m.s. of about 5 mm and coincide within ~ 2 mm at the LKr, while in the first case the beam spot of each parallel beam would have been about 2 cm wide.

After this, a second achromat is placed to reduce the muon contribution and to house the first detector, KABES, aiming at measuring the position and momentum of incoming particles. Before the beginning of the decay region a cleaning and a final collimator are placed, as shown in figure 2.2.

In table 2.1 the fluxes of different particles entering the decay region are shown. It must be noticed that, although the kaon fraction is small compared to other particles, the latter ones either do not decay, remaining thus in the beam pipe, or their products (e.g. $\pi^{\pm} \to \mu^{\pm}\nu$) are mostly confined inside the beam pipe.

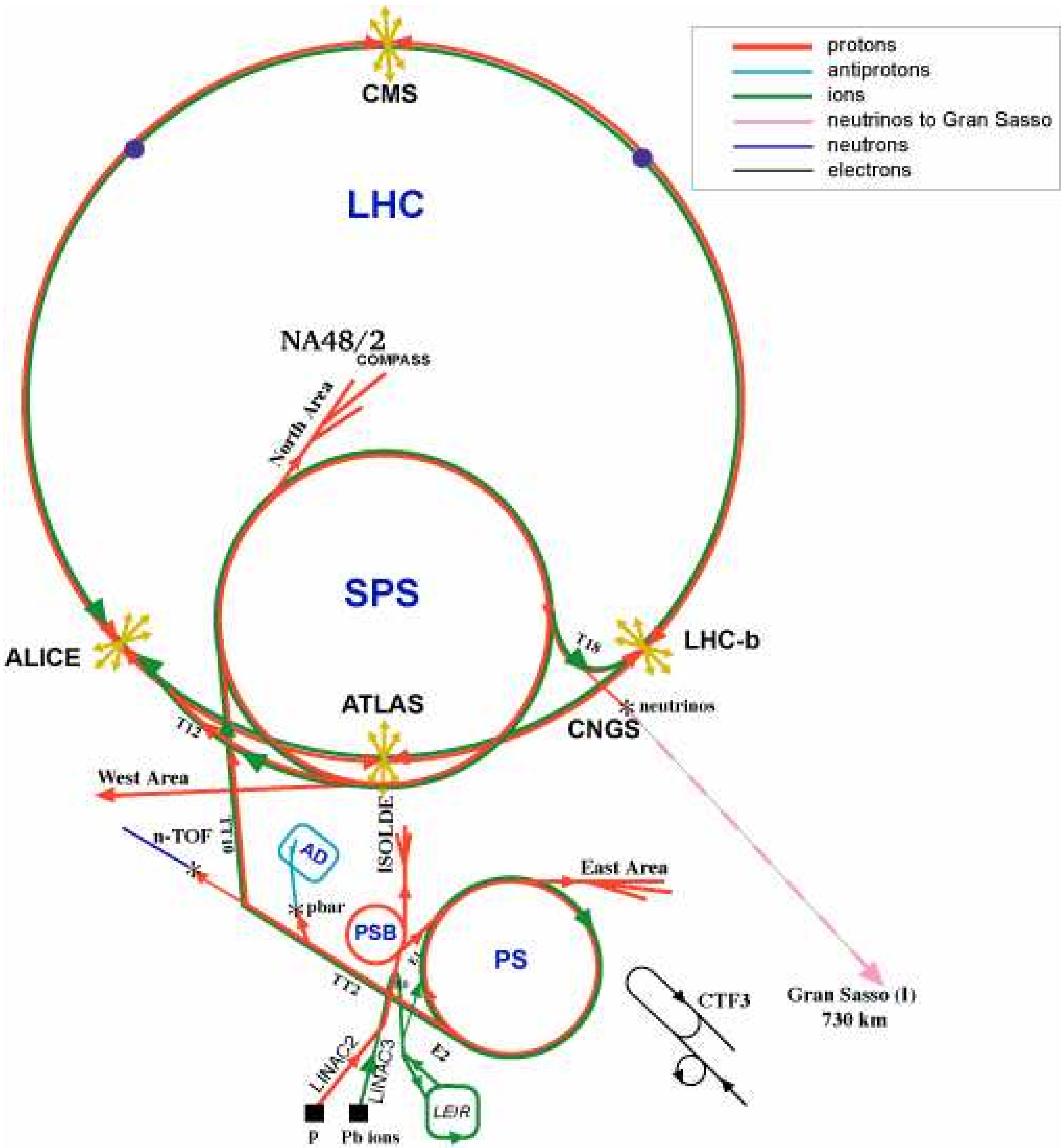

Figure 2.1: CERN accelerator system overview. NA48/2 is located north of the SPS, in the French area of Prevessin.

2.2 Detectors

In this section the detectors of the NA48/2 apparatus will be described, following their order with respect to the beam direction and stressing their role in particle detection. A schematics of the NA48/2 detectors is shown in fig. 2.3.

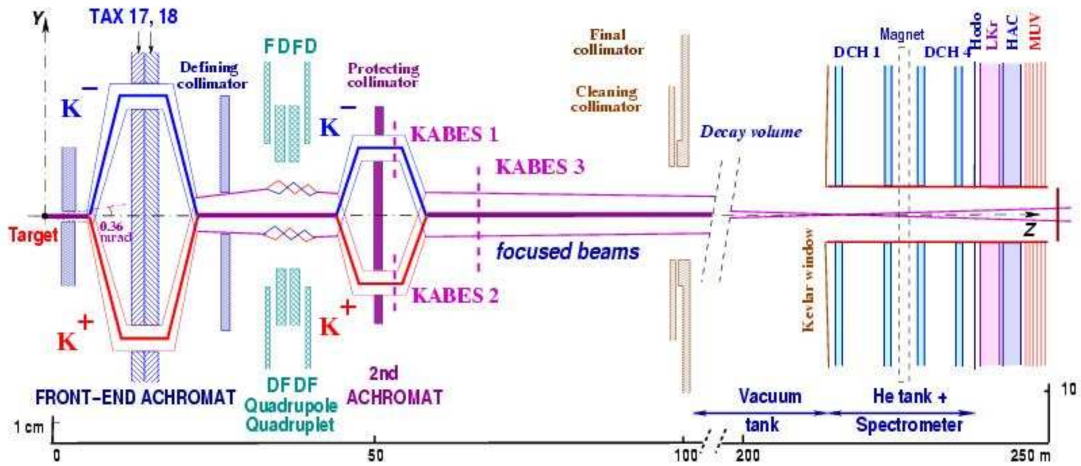

Figure 2.2: Section of the NA48/2 beamline.

particle	$+(\cdot 10^6/pulse)$	$-(\cdot 10^6/pulse)$
K	2.2	1.3
π	23	17
p	6.1	0.6
e	6.0	6.0
$Other$	~ 1	~ 1

Table 2.1: Fluxes of the different kind of particles constituting the beam at the beginning of the decay region.

2.2.1 KABES

KABES (KAon BEam Spectrometer) [45] is the first detector housed, as mentioned, at the beginning of the decay region. KABES is a TPC detector based on MICROMEGAS [46] with an amplification gap of 50 μm, whose primary goal is to measure the energy and direction of incoming kaons before they decay. A schematics of the detection process is shown in fig. 2.4.

The KABES detector is made of three double stations, each of them recording the position (both vertical and horizontal) and transit time of the kaons. Two stations are placed in the middle of the two arms of the second achromat, where the beam has been split by a magnetic field into positive and negative components; the third one is placed downstream the achromat, where the two beams are again collinear. The momentum of the incoming kaon is proportional to the coordinate difference between the station 1 or 2 and the station 3. The total amount of radiation length due to KABES is $1.29 \cdot 10^{-3}$, so that the effect of multiple scattering on the beam

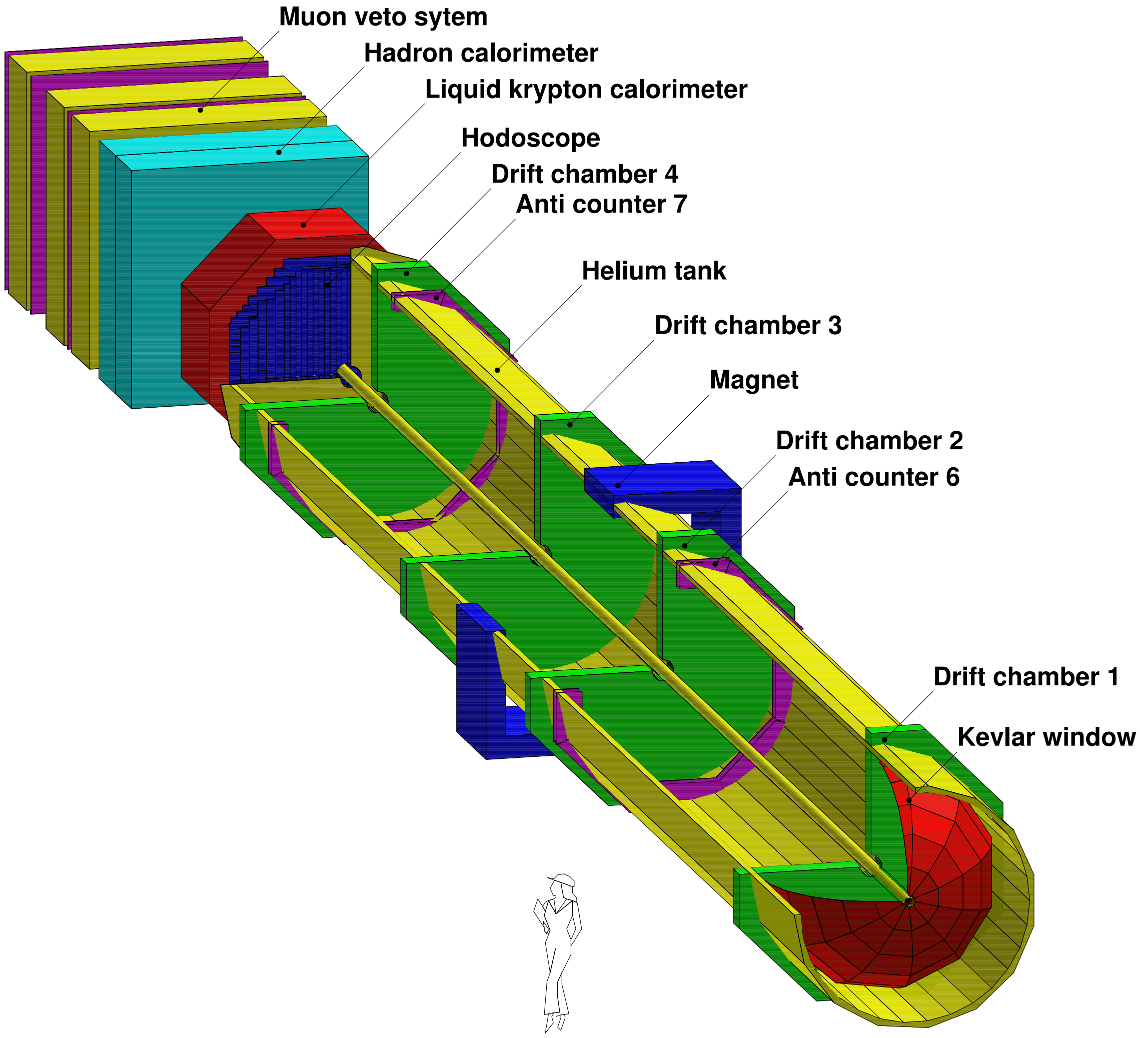

Figure 2.3: Layout of NA48/2 central detectors.

is minimized.

The readout of the strips is performed using HPTDC (High Performance TDC), developed at CERN. The system is able to stand a rate of 8 MHz per strip and a total rate of 40 MHz for a single station.

The momentum resolution of KABES has been evaluated using the spectrometer to reconstruct the decay $K^{\pm} \to \pi^{\pm}\pi^{+}\pi^{-}$ and studying the convolution of KABES resolution with the spectrometer's one; in this way a value of 1.1% has been measured. KABES performances in terms of space and time resolution are summarized in table 2.2.

KABES information is useful in decays for which a high resolution on kinematical variables is fundamental to distinguish the signal from the background: this can

Horizontal position	100 μm
Vertical position	130 μm
Time	$\simeq$ 0.65 ns

Table 2.2: Kabes resolution.

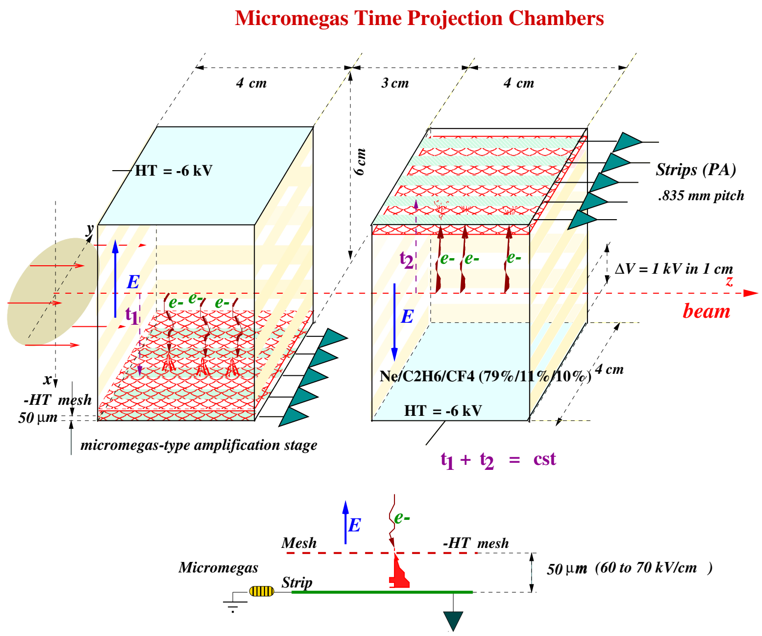

Figure 2.4: Principle of MICROMEGAS TPC functioning .

happen, for example, with rare decays, where the presence of a neutrino in the final state does not allow the reconstruction of the whole event. This is the case of the channel under analysis in this thesis: however the use of KABES implies some drawbacks due to the kaon mistagging, which can be of the order of few percent [47]. For this reason in the present analysis the nominal 60 GeV/c value was used for the kaon momentum, assumed to be directed along the Z axis and KABES info was not used.

2.2.2 Decay region and AKL anticounters

The NA48/2 decay region, shown in fig. 2.5, is contained in a cylindrical tube (called blue tube) which is $\sim$ 113 m long and 1.92 m in diameter, the latter increasing

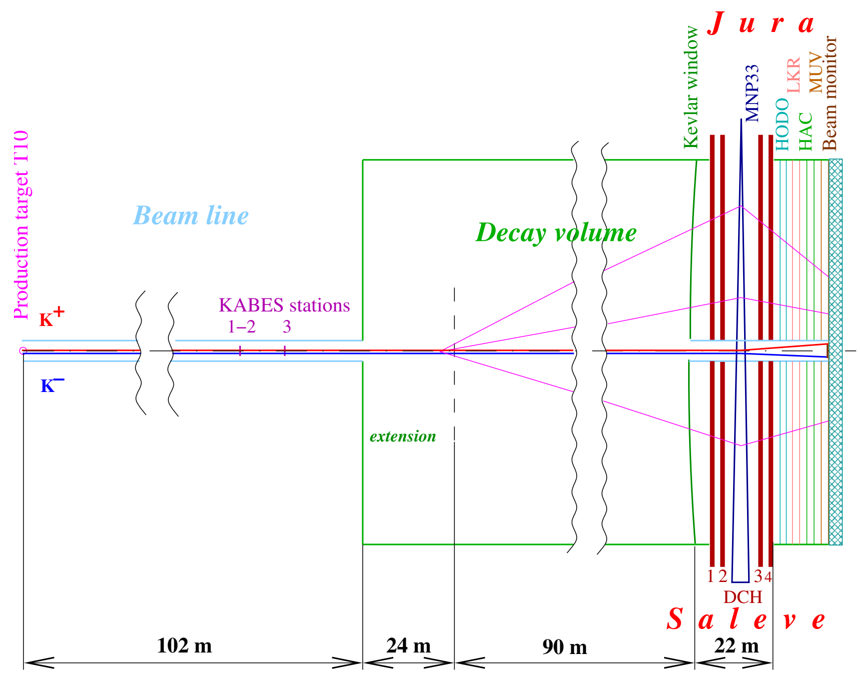

Figure 2.5: The NA48/2 decay region.

up to 2.4 m in the last 48 m. The decay region is evacuated (up to 10^{-4} mbar) in order to avoid interactions of particles from kaon decays before they reach the detectors.

The downstream part of the tube is closed by a thin Kevlar window, which separates the vacuum of the decay region from the Helium gas filling the magnetic spectrometer's volume. The window has an hemispherical shape with 1.3 m curvature radius; its thickness is 0.9 mm, corresponding to $3 \cdot 10^{-3}$ radiation lengths. The beam continues in an evacuated Aluminum pipe 1.2 mm thick and of 152 mm internal diameter.

A small magnetic field, mostly due to the Earth field, is present in the blue tube and has been carefully measured and mapped in winter 2003 by the use of Hall probes. The results of this measurement were included in the MC simulations used in the analyses. In fig. 2.6 the X and Y components of the measured magnetic field are shown.

Along the blue tube and in the spectrometer a counter detector system of 7 rings of iron and scintillator is placed, as shown in fig. 2.7. Its main purpose was to detect photons coming from $K_L \to 3\pi^0$ decay in the NA48 experiment, but they were also used as vetos in some NA48/2 analyses. Each pocket is made of two layers of scintillator, with a steel plate in front acting as a converter. Each layer is made of 12 plastic scintillator plates 10 mm thick, viewed by 12 photomultipliers (PMs)

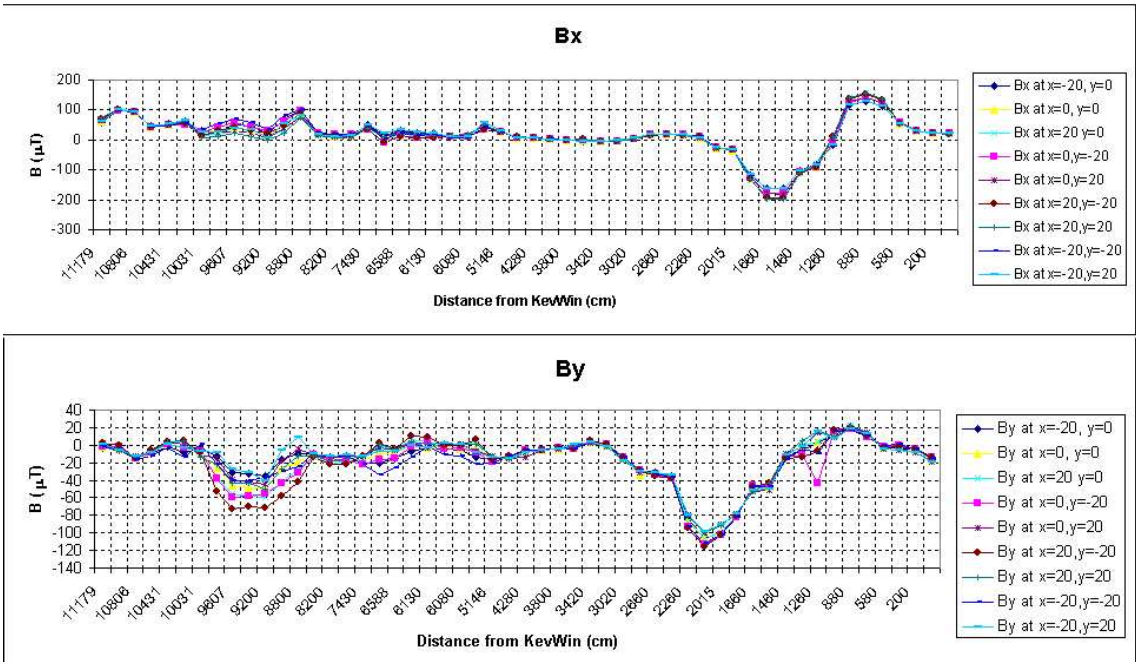

Figure 2.6: The X and Y component of the so-called "Blue Field", the residual magnetic field along the blue tube decay region.

for sockets 1 to 4 and by 8 PMs for pockets 5 to 7. The last 2 pockets are placed inside the spectrometer.

2.2.3 The magnetic spectrometer

The Magnetic Spectrometer is made of 4 drift chambers (DCH), with a dipole magnet placed between DCH2 and DCH3 (fig. 2.8). The magnet provides a transverse momentum kick of 120 MeV/c in the horizontal plane, thus allowing the track momentum measurement by measuring the track directions before and after the deviation.

In order to reduce systematic effects related to possible detector's asymmetries, the magnet's polarity was frequently inverted. In 2003 this was done on a daily basis, while in 2004 the reversing took place every $30 \cdot 10^6$ collected triggers (~ 3 hours). The accuracy of the field inversion is monitored by using Hall probes and by reconstructing offline the kaon mass in $K^\pm \to \pi^\pm\pi^+\pi^-$ decay. The spectrometer volume is kept at atmospheric pressure and filled with Helium to reduce Coulomb scattering.

Each chamber, octagonal in shape with an external radius of 120 cm, is made of 8 planes of sense wires (fig. 2.10) grouped in 4 views of 2 planes each, staggered

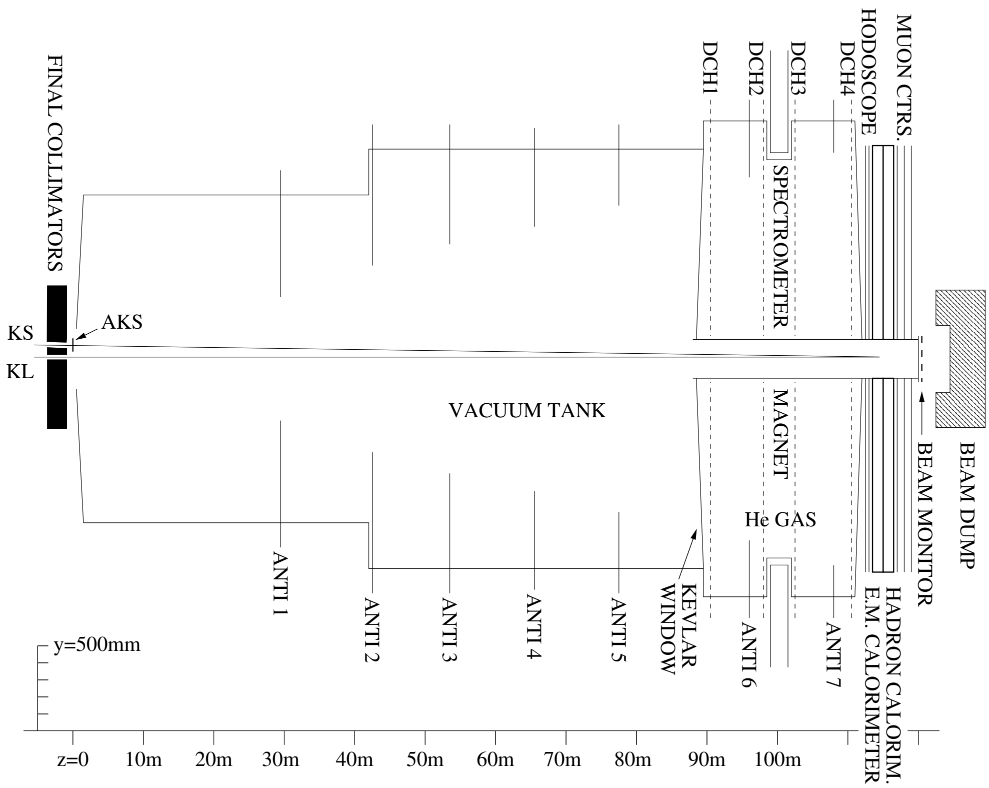

Figure 2.7: Positions of the AKL ring counters.

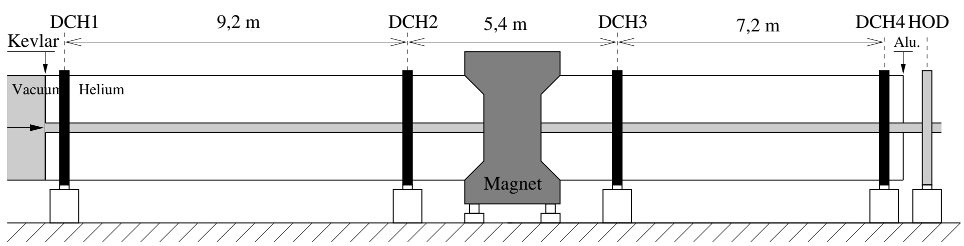

Figure 2.8: Position of drift chambers and magnet with respect to NA48/2 beam line.

by half wire pitch. The wires are aligned in X(horizontal), Y(vertical), U and V directions, where U and V are the directions obtained by rotating the X and Y axes by 45°; the total number of wires is 256 for each plane. The chambers are filled with a mixture of Argon (50%) and Ethane (50%), yielding a maximum drift time of 100 ns (corresponding to half the 10 mm wire pitch) and a global resolution better than 100 μm on the space point position; the time resolution is 700 ps, thanks to the use of HPTDCs. The momentum resolution for tracks reconstructed by the spectrometer can be parametrized as:

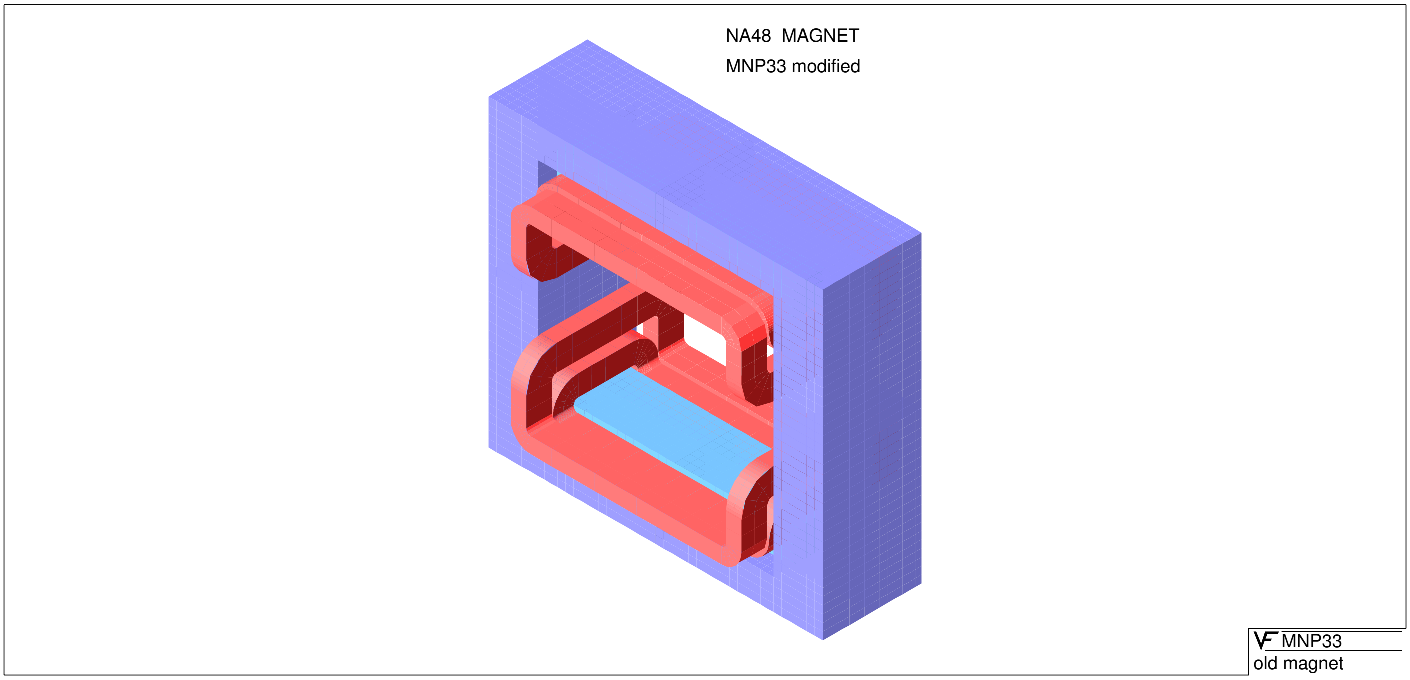

Figure 2.9: The spectrometer magnet MNP33. The central aperture measures 2.45 $\times$ 2.20 m^2.

$$\frac{\sigma(P)}{P} = 1.0\% \oplus 0.044 \cdot P(GeV/c)\%$$

where the first term is related to multiple scattering and the second one to the space point resolution. The resolution on the $K^{\pm}$ mass in the decay $K^{\pm} \to \pi^{\pm}\pi^{+}\pi^{-}$ reconstructed using only the spectrometer's data is 1.7 MeV/c^2. A schematization of the electric field generated by the DCH wires and of the signal induced on single wires by a charged particle are shown in fig. 2.11 and 2.12 respectively.

Because of the importance of the drift chamber in the charged asymmetry measurement, special care was taken in order to avoid any kind of left-right asymmetry: in particular symmetric wires with respect to the DCH plane center were read by the same electronic module, and special muon runs were taken during the data-taking in order to monitor the DCH alignment.

2.2.4 The charged hodoscope

The charged hodoscope is placed between the last DCH and the calorimeter; its purpose is to yield a time measurement of charged tracks for both the offline and the online analysis and to provide a fast trigger condition based on the number of

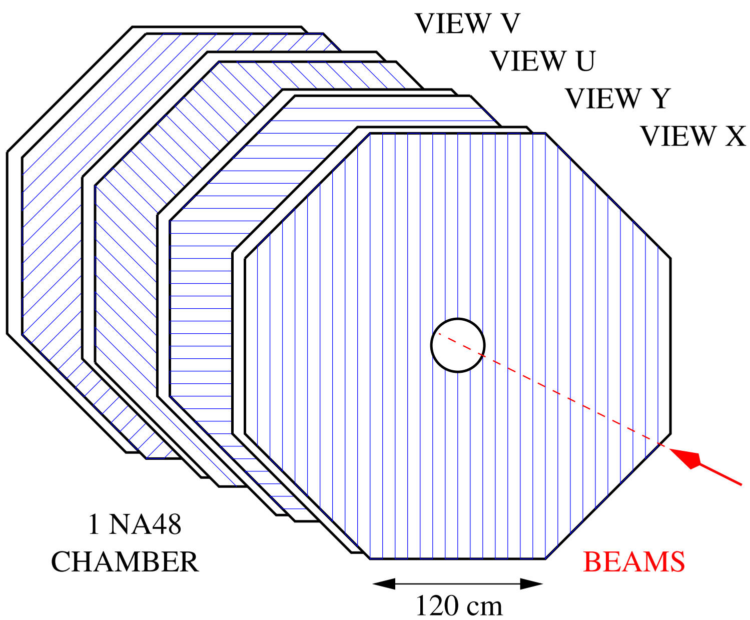

Figure 2.10: The 4 views of one NA48 drift chamber.

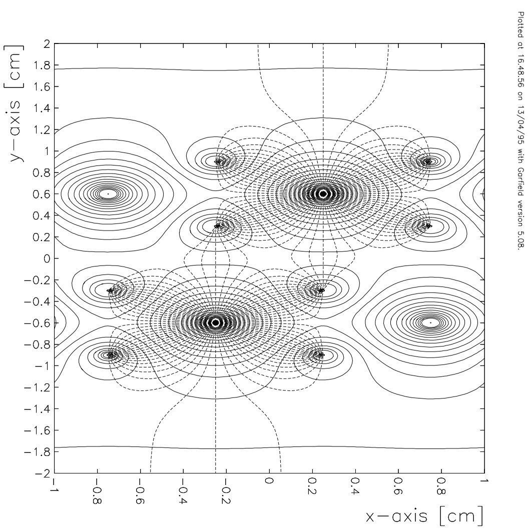

Figure 2.11: Electric field inside a DCH plane.

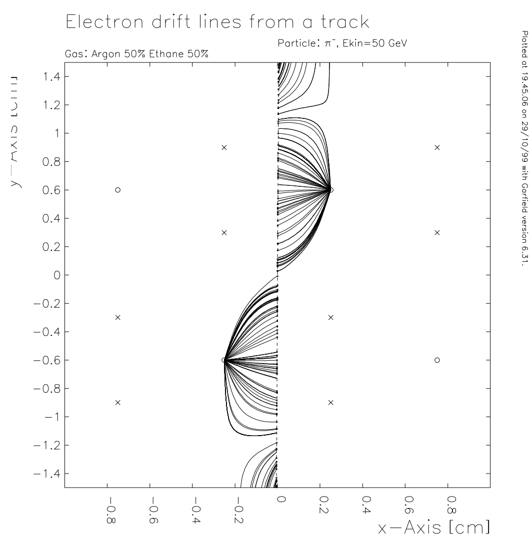

Figure 2.12: Signal induced by a 50 GeV pion through a drift chamber.

incoming tracks.

The charged hodoscope is composed of two planes of plastic scintillator strips, respectively oriented in the horizontal and vertical direction. There are 64 strips in each plane, with different widths and lengths according to the octagonal geometry of the detector: the length is in the range 60-121 cm, while the width varies from

6.5 to 9.9 cm. The layout of the hodoscope is shown in fig. 2.13, the central hole is 27 cm in diameter. The horizontal plane is 80 cm from the calorimeter, while the vertical one is 80 cm upstream of the former: the different timing related to this distance can be used to tag false coincidences due to the *back splash* coming from the calorimeter's surface, i.e. particles undergoing a reflection on the LKr surface and crossing the hodoscope.

The trigger logic conditions are built by combining the coincidences of signals by the 4×4 quadrants of the two planes: for example a track will generate a Q1 signal if two geometrically compatible quadrants, one for each plane, detect the passage of one particle. The Q2 condition, aiming at triggering events with more than 1 track, is given by the time coincidence of at least two Q1 signals.

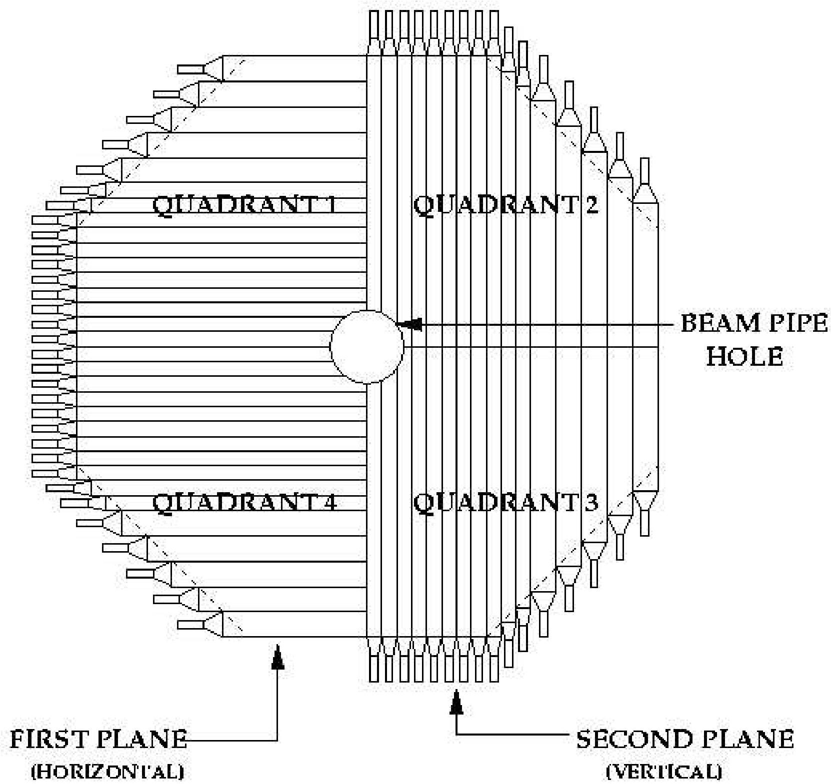

Figure 2.13: The two planes of the charged hodoscope.

The signals from the photomultipliers of each strip are also sent to a 10 bit 40 MHz FADC/TDC, where the signal pulse height and time are measured. The read-out is performed by special VME modules called PMB (Pipelined Memory Board). In this way a time resolution of ~ 150 ps can be achieved.

2.2.5 The electromagnetic calorimeter (LKr)

For the detection and energy measurement of electromagnetically interacting particles, NA48/2 uses a quasi homogeneous liquid Krypton ionization chamber. This choice is due to the good linearity in the detector's response, the absence of aging problems and the short radiation length (less than 5 cm), which allowed the realization of a compact calorimeter in the longitudinal direction without using passive material as radiator, as in sampling calorimeters.

Characteristics

The calorimeter is approximately octagonal in shape in the transverse plane; the length of the active part in the longitudinal direction is 127 cm, corresponding to 27 radiation lengths. The active part is divided into 13248 cells defined by Cu-Be-Co longitudinal ribbons 18 mm wide, 127 cm long and 40 μm thick, transversally spaced by $\simeq$ 1 cm: in this way a single cell has a section of $\simeq 2\times2$ cm (see fig. 2.17).

The cells are not exactly parallel to the beam direction: a projective geometry, pointing at $\sim$ 90 m in front of the calorimeter, was chosen according to the acceptance of the $K_{L,S} \to \pi^0\pi^0$ decay in NA48, in order to perform the best measurement of the angle between the photons and the beam direction. The stability of ribbons is obtained by 5 plates along the longitudinal direction, spaced by $\simeq$ 21 cm.

The function of the plates is twofold: to define the distance between the ribbons (which are pulled with a 2N tension) and to give them a peculiar "zig-zag" shape, used to minimize inefficiency for showers developing close to them (the so called *accordeon geometry*). In the middle of each cell a collecting anode ribbon is placed, to which a tension of about 3 KV is applied.

Krypton thermal stability is crucial in order to assure a constant response of the calorimeter in space and time. Krypton temperature is kept constant at 121.0$\pm$0.1 K through a complex cryogenic regulation system. The calorimeter is enclosed in a 4 mm thick external aluminum vessel and an internal vacuum insulated 29 mm thick steel container, housing the $\simeq$ 9 m^3 of Krypton. The temperature dependence of electron drift speed is $\Delta v_d/v_d \cdot \Delta T \simeq 0.87\%$ K^{-1}. The cryostat introduces $\simeq$ 0.65 radiation lengths of passive material, corresponding on average to 50 MeV of undetected energy for the incoming photons.

The most important characteristics of the liquid Krypton can be found in table 2.3.

Readout

The readout of the LKr works in a current-sensitive mode using the initial induced current, proportional to the ionization generated in the Krypton by the electromagnetic shower and therefore to the energy of the initial photon or electron. The front-end electronics, directly mounted on the detector back-plate in order to

Liquid Krypton properties		
Atomic number	Z	36
Mass number	A	84
Density (at 120 K)	$\rho(g/cm^3)$	2.41
Radiation length	X_0 (cm)	4.7
Molière's radius	$R_M(cm)$	4.7
Energy to produce the pair e^-+ion	W(eV/pair)	20.5
Hadronic interaction length	$\lambda_l(cm)$	60
Boiling temperature (at 10^5 pascal)	$T_b(K)$	119.8
Fusion temperature (at 10^5 pascal)	T_m	116.0
Drift velocity @ 1 KV/cm	$v_d^e(mm/\mu s)$	2.7
Drift velocity @ 5 KV/cm	$v_d^e(mm/\mu s)$	3.7
Critical energy	$E_c(MeV)$	21.51

Table 2.3: Main physical properties of liquid Krypton.

minimize the noise and the rise time of the signal, consist of the preamplifiers and the electronic calibration system for single channels.

Coaxial cables take the output of the preamplifiers to feedthroughs, equipped with suitable transceivers; hence the signals reach the readout modules, the CPD (Calorimeter Pipelined Digitizer). The sampling of the signal is performed every 25 ns (40 MHz) by a 10 bit FADC with an automatic gain switching on the whole dynamic range (3.5 MeV to 100 GeV) in order to avoid signal overflows; the gain value is recorded in two additional bits.

The digitized signals are bufferized and then sent to a Data Concentrator system, which applies *zero suppression* for cells below a certain treshold and runs a clusterization algorithm for cells above threshold. In this way the number of read cells is reduced to $\simeq$ 100 per shower.

A small fraction of the LKr cells ($\simeq$ 60) are marked as *dead cells*, the reason being the presence of problems in the electronic chain (faulty preamplifiers, excessive noise, no calibration, bad pedestals) which corrupt the signal. In fig. 2.14 the dead cell distribution on the LKr surface is shown.

Calorimeter performances

The linearity of the calorimeter response has been frequently checked by selecting electrons from $K_L \to \pi^{\pm}e^{\mp}\nu_e$ (K_Le3) decay and comparing the energy measured by the LKr with the momentum measured by the spectrometer (fig.2.16). The overall energy scale was obtained by adjusting energies of photons from $K_S \to \pi^0\pi^0$ such that the π^0 vertex distribution began at the accurately measured position of AKS counter (which vetoed K_S decays upstream of itself); the result was checked with

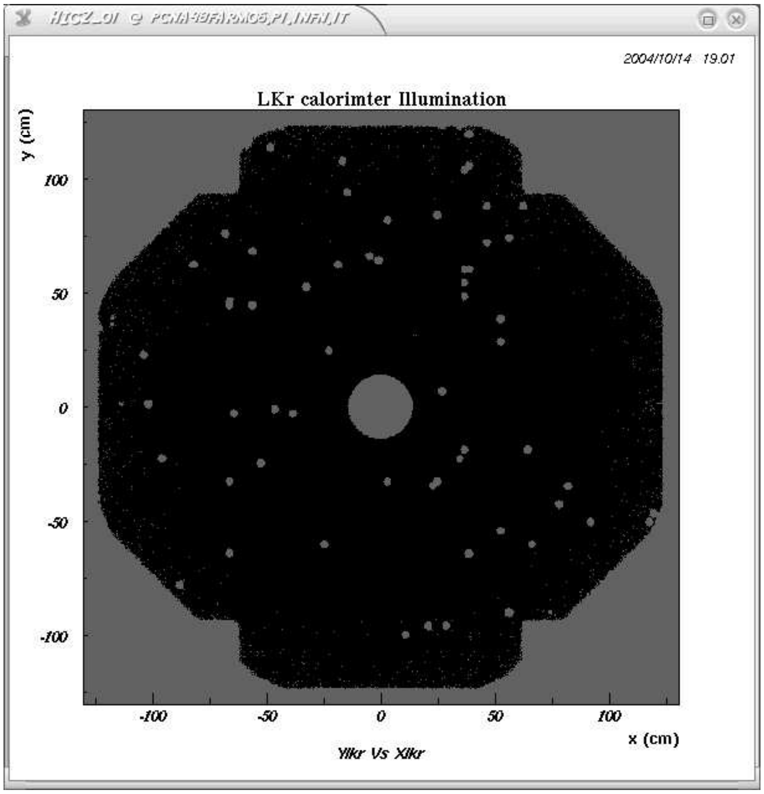

Figure 2.14: Dead cells in the LKr.

special η runs (where $\eta \to 2\gamma$ or $\eta \to 3\pi^0$ were produced in a thin target at a known longitudinal position at about halfway the fiducial decay region), these decays being used also to compute calibration constants.

The energy resolution was measured using dedicated electron runs with momentum spread of 0.1% and checked with K_{Le3}. The resolution can be parametrized as [48]:

$$\frac{\sigma_E}{E} = \frac{0.032}{\sqrt{E(GeV)}} \oplus \frac{0.09}{E(GeV)} \oplus 0.0042 \tag{2.1}$$

where the first term is due to fluctuation in photoelectrons' statistics, the second one to electronic noise and radioactivity and the last one to cell intercalibration (fig.2.15).

The space resolution of the LKr was measured with special electron runs (comparing their position in LKr and that measured by DCHs) to be:

$$\sigma_{x,y} = (\frac{4.2}{\sqrt{E(GeV)}} \oplus 0.6)\mathrm{mm} \tag{2.2}$$

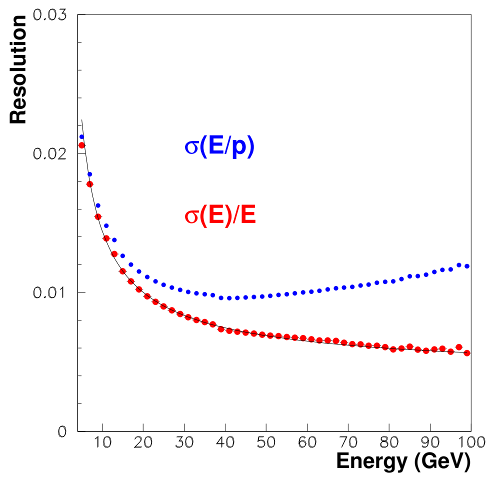

Figure 2.15: Resolution of the LKr energy measurement.

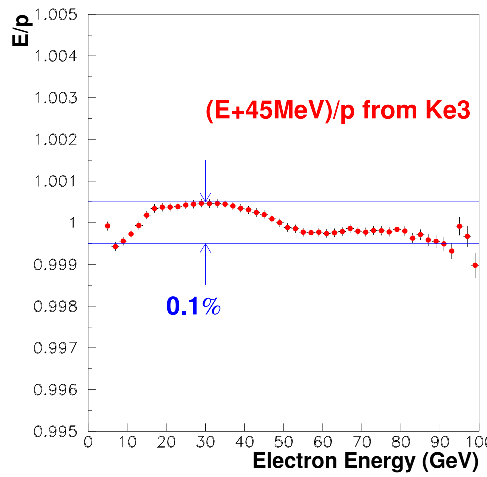

Figure 2.16: The linearity of the LKr is within $\pm$ 0.05% over the whole energy spectrum. The ratio E/p is defined in Chapt. 4.

The good energy and position resolution (respectively $\sim$ 1% and $\sim 1mm$ at 20 GeV) are important when reconstructing the π^0 decay vertex, which can be obtained, imposing the PDG value of the π^0 mass, by the formula:

$$V_{\pi^0} = \frac{\sqrt{[(x_1 - x_2)^2 + (y_1 - y_2)^2]E_1 E_2}}{M_{\pi^0}} \tag{2.3}$$

where V_{π^0} is the decay vertex distance from the longitudinal center of gravity of the shower development in the LKr, $x_{1,2}$, $y_{1,2}$ their transverse coordinates and $E_{1,2}$ the γ's reconstructed energy. The resolution on V_{π^0} is found to be better than 1 m at 70 m from the LKr. Thanks to the LKr's high granularity, two photons are resolved if their relative distance is at least $\sim$2 cm.

The time resolution for a single electromagnetic cluster is found to be $\sim$ 500 ps.

2.2.6 The neutral hodoscope

A neutral hodoscope (NHOD) is housed inside the electromagnetic calorimeter, on the second LKr spacer, at the depth (9.5 X_0) where a 25 GeV photon's shower reaches its maximum. The NHOD is made of 256 bundles of scintillating fibers immersed in the LKr (fig.2.17). The signal produced by an e.m. shower is read by 32 photomultipliers (8 for each quadrant) and provides an independent measurements of the shower time, as well as an independent source of minimum bias trigger, the so-called T0N. The time resolution is $\sim$ 250 ps.

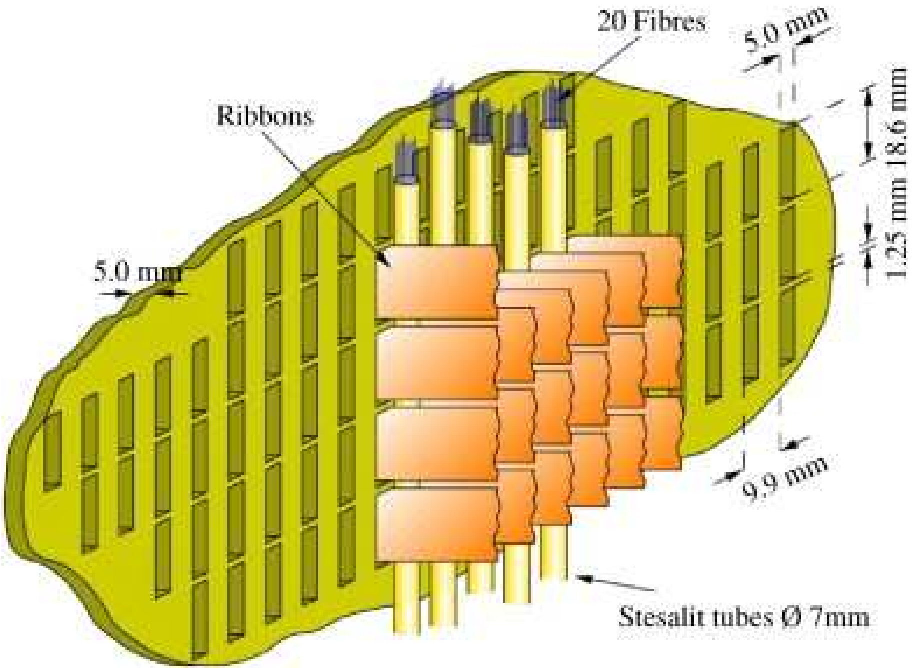

Figure 2.17: Position of the NHOD fibers with respect to the second LKr spacer.

2.2.7 The hadronic calorimeter

An iron-scintillator sampling calorimeter (HAC, see fig. 2.18) is used to measure hadron energies. The HAC is placed downstream the calorimeter and is made of two modules, whose total thickness is 6.7 λ_{int}. Each module is made of 24 iron plates alternated to scintillator planes; each plane is realized with 44 half-strips, for a total area of 2.7×2.7 m^2 of sensible area, as shown in fig.2.18. The energy resolution is:

$$\frac{\sigma(E)}{E} = \frac{65\%}{\sqrt{E(GeV)}}$$

2.2.8 The muon veto

The muon veto (MUV) is made of three plastic scintillator planes, each one covering a surface of 2.7×2.7 m^2; before each plane a 80 cm ($\sim 5\lambda_{int}$) thick iron wall is placed. Each plane is subdivided into plates: 11 plates, 1 cm thick, for the first two planes, 6 plates, 6 mm thick, for the third plane (fig.2.19). All plates are read at both sides by photomultipliers; the readout was performed with a 1GHz deadtime-less TDC system.

The time resolution of the MUV is ~ 700 ps [49]. The inefficiency was measured using $K_{L\mu3}$ to be $\sim 1\%$.

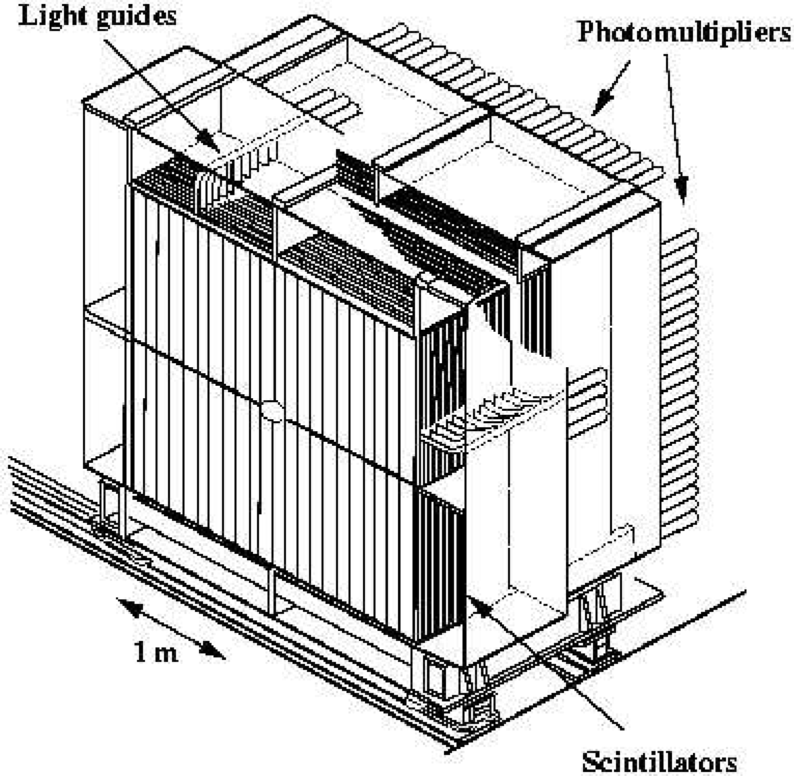

Figure 2.18: The HAC detector.

2.3 Trigger

The NA48 trigger system is designed to have no dead time with an event rate in the detectors at the level of 1 MHz. The system is pipelined and synchronized by a 40 MHz clock. The data coming from the detectors are stored every 25 ns on circular memories 204.8 μs deep.

Within the trigger system two branches can be distiguished:

- the “charged” trigger, which mainly uses CHOD and DCHs, is responsible for the acquisition of charged particles;
- the “neutral” trigger, which uses LKr, NHOD and HAC, is responsible for the acquisition of neutral particles.

Since both neutral and charged particles are present in several $K^{\pm}$ decays, both triggers (or part of them) are often involved in the acquisition of a single channel.

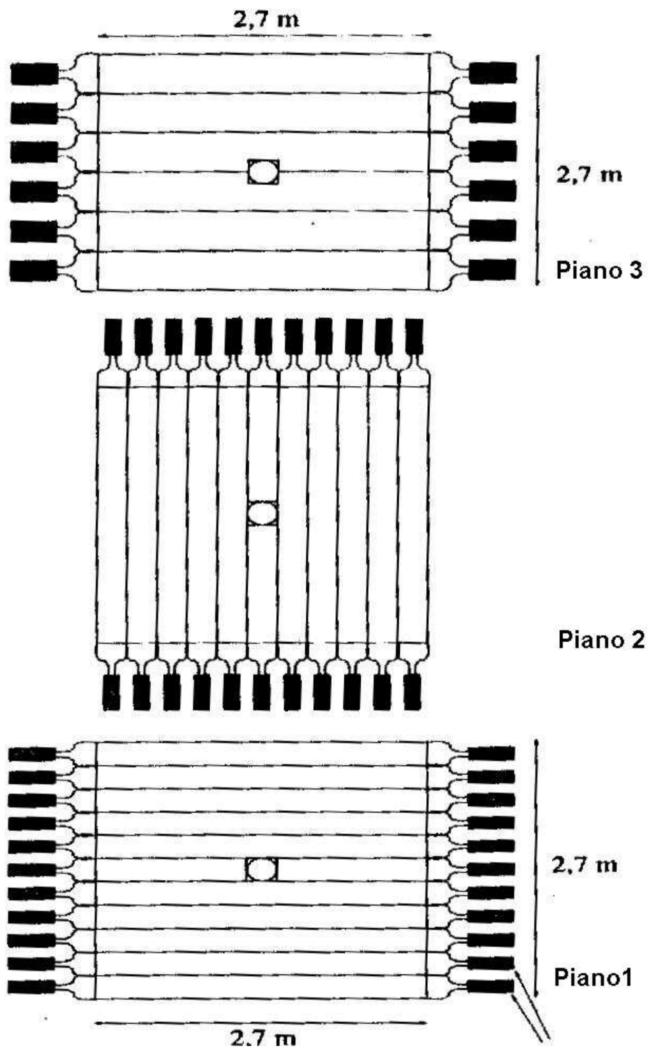

Figure 2.19: Scintillator planes in the Muon veto.

A third subsytem, the Trigger Supervisor (TS), collects the information from both triggers and takes the final decision on the acquisition of the event.

2.3.1 The charged trigger

The amount of data collected by the detectors must be reduced from $2 \cdot 10^6$ triggers/burst to $\sim 5 \cdot 10^4$ triggers/burst, which is the number of events that can be written on disk. The reduction takes place in two steps: the first is called Level 1 (L1) and is based on fast hardware signals coming from CHOD and DCHs, while the second one, called Level 2 (L2), is done via software, through a rough reconstruction of the event using DCH information.

L1 trigger

The first step of the charged trigger chain reduces the rate at the level of 150 KHz. Signals from several detectors are used to provide fast trigger conditions: this is the case, for example, of Q1 and Q2 signals, already mentioned in par. 2.2.4. Other detectors used for L1 signals are the AKL (in veto mode) and the chambers. All L1 signals are combined with the information from the LKr at the L1 TS level. Before being processed by the level 2 (L2), a 30-bit time-stamp is attached to the event; moreover a 3-bit code (*strobe*) is defined to act as an input to the L2 algorithm. The typical rates of L1 signals are shown in table 2.4.

Trigger	Rate/spill
Q1	$1.8 \cdot 10^6$
Q2	$2.9 \cdot 10^5$
Q2·!AKL	$2.5 \cdot 10^5$
T0N	$7.0 \cdot 10^4$
E_{LKr} >10 GeV	$2.4 \cdot 10^5$
1μ	$1.6 \cdot 10^6$

Table 2.4: Typical rates of Level 1 signals.

L2 trigger (Massbox)

The second level charged trigger, called Massbox (MBX), is a software trigger based on DCH data to perform a fast online reconstruction of space points and track segments. To do this, a processor farm is used, which takes a decision asynchronously with a maximum latency of 100 μs. The proper reduction factor can be obtained because it is possible to apply online relatively complex algorithms like vertex reconstructions or invariant mass calculations; the online resolution on kinematical quantities, even if worse with respect to the offline reconstruction, assures a high efficiency for all the defined triggers.

The MBX system is subdivided in 4 subsystems, as shown in fig. 2.20. These are:

- **Coordinate Builder (CB)**: the hit coordinates are built analyzing the information coming from the two planes in each view of the DCHs. The reference time is given by the Q1 signal.

- **Event Builder and Dispatcher (EDB)**: the EDB gathers the information provided by the CB and sends them to an available Event Worker for processing.

- **Event Worker (EW)**: it uses the 12 coordinates (4 for each of the 3 DCHs included) to compute the space points associated with the track, together with other physical quantities. A space point is reconstructed if at least one of the following conditions is satisfied within 1.5 mm tolerance:

$$u = \frac{x+y}{2}$$

$$v = \frac{y-x}{2}$$

$$y = \frac{u+v}{2}$$

- **Event Worker Farm Manager (EWFM)**: it sends the time stamp of the candidate events to the TS for the final decision and informs the EB about which EW can accept events to be processed. It also manages the X_{off} signals, which prevent the delivery of new L1 strobes by the L1TS if the EDB is busy.

In table 2.5 the principal L2 signal rates in 2003 are shown.

L2 Trigger	Rate
2 Vertices (MBX-2VTX)	22 KHz
1 Vertex and mass cut	13 KHz
Anti $\pi^+\pi^0$ cut (MBX-1TRKP)	14.5 KHz
Anti K_{l2} cut	0.8 KHz

Table 2.5: Typical rates of L2 signals in 2003.

2.3.2 The neutral trigger

The NA48 level 2 neutral trigger is a self-triggering deadtime-less pipelined trigger, synchronized with the 40 MHz clock of the experiment. Its main function in NA48/2 is to monitor the MBX trigger for the $K^\pm \to \pi^\pm\pi^0\pi^0$ decay and also to provide the total energy deposited in the LKr calorimeter for the L1 TS. These operations are performed through the calculation of some kinematical quantities made by custom VLSI electronics.

The LKr cells are grouped into *super cells*, made of 16 (2×8) single cells, both in the X and Y view. The energies of these cells are summed and their signal is digitized by a 10 bit 40 MHz FADC. The digital signals are finally summed into 64 strips on both X and Y projections by the Vienna Filter Module system, each strip being 2 cells (4 cm) wide. The SPY system fans out the signal thus obtained into the Pipeline Memory Board (PMB) and the Peak Sum System (PSS). The PMB information are used for online monitoring and offline checks of the calorimeter readout; the PSS allows the calculation of the energy distribution momenta (up to the 2nd), the number of peaks and their timings in the horizontal and vertical projections. The momenta are computed according to the formulae:

$$\begin{cases} m_{0,x} = \sum_{i=1}^{64} E_i^x \quad m_{0,y} = \sum_{i=1}^{64} E_i^y \\ m_{1,x} = \sum_{i=1}^{64} E_i^x (i-32) \quad m_{1,y} = \sum_{i=1}^{64} E_i^y (i-32) \\ m_{2,x} = \sum_{i=1}^{64} E_i^x (i-32)^2 \quad m_{2,y} = \sum_{i=1}^{64} E_i^y (i-32)^2 \end{cases} \tag{2.4}$$

These quantities are then used to calculate physical quantities for the event (total energy, COG radius, reconstructed vertex) by the Look-Up Table (LUT), which are then used in trigger cuts. Another quantity used in the triggers' definition, in particular to define the NTPeak condition, is the number of peaks in both X and Y views. A peak is defined as an energy maximum on the strips, according to the conditions:

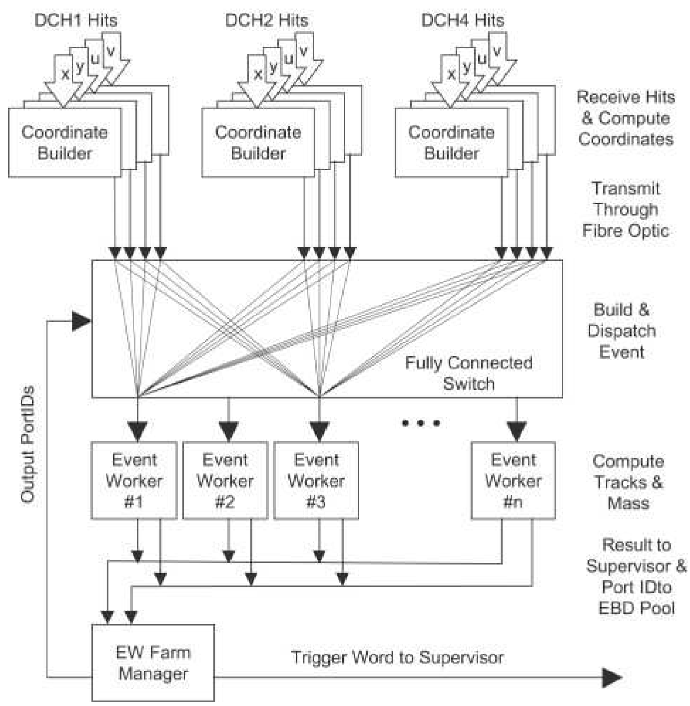

Figure 2.20: Scheme of the L2 charged trigger system (Massbox).

$$E_{i-1} < E_i \ , \ E_i > E_{i+1}$$

The peaks are counted in time windows of 3.125 ns to reduce the effect of accidental showers. The NTPeak condition is fulfilled if more than two peaks are detected either in X or Y view.

A diagram of the neutral trigger system is shown in fig. 2.21.

2.3.3 The trigger supervisor

The information from the various triggers is finally sent to the trigger supervisor, which takes the final decision on the event. It also adds a final trigger word and time-stamp to the event and sends to the Read-out Controllers the command to record the event. Besides the L2 triggers, in order to measure trigger efficiencies, several control triggers are acquired with different downscaling factors, in order to match the total bandwidth available: some of them are summarized in table 2.6.

2.4 Data acquisition

The NA48/2 data acquisition system, shown in fig. 2.22, is composed of 11 subdetector PCs, 8 event builders and 1 control PC, which are housed at Prevessin

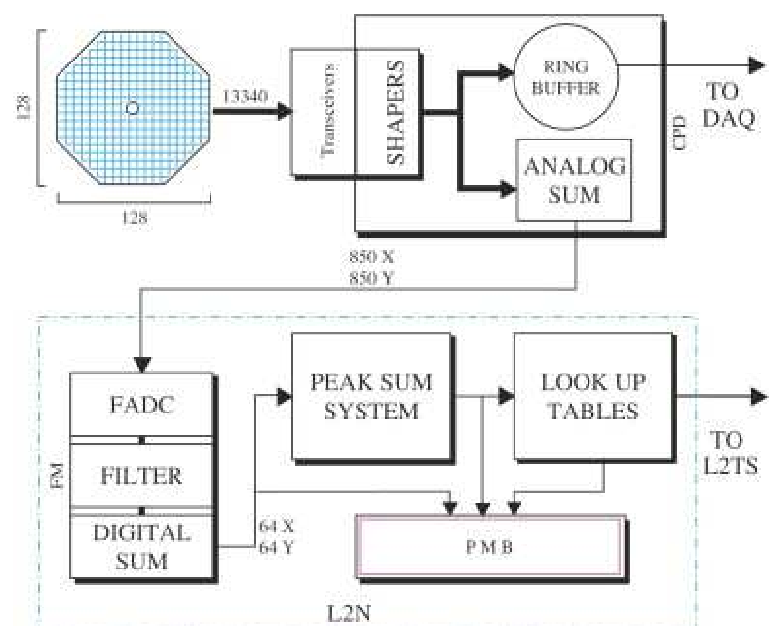

Figure 2.21: Diagram of the neutral trigger.

Control trigger	Rate	Downscaling
T0N	0.6 KHz	200
NT PEAK	1.3 KHz	50
NT NOPEAK	1.0 KHz	80

Table 2.6: Typical rates of some control triggers and related downscaling factors.

site. A fast 200 Mbit/s switch delivers data to all PC's, which are equipped with Linux OS. The subdetector PC's store the data sent by the sub-detectors during the SPS burst. These data are then partitioned in 8 blocks and sent to the event builder PC's in such a way that all data coming from a single event are processed by the same event builder. Here the data are rearranged into complete events and then sent through an optical fiber connection to CERN disk servers in Meyrin, were they are processed and stored on magnetic tapes. A lack of data from one of the sub-detectors during the burst causes a rejection of the whole burst.

2.5 Reprocessing

The data coming from each event builder and relative to a single burst are called *burstlets*. All the burstlets are copied onto private disks installed at the IT division

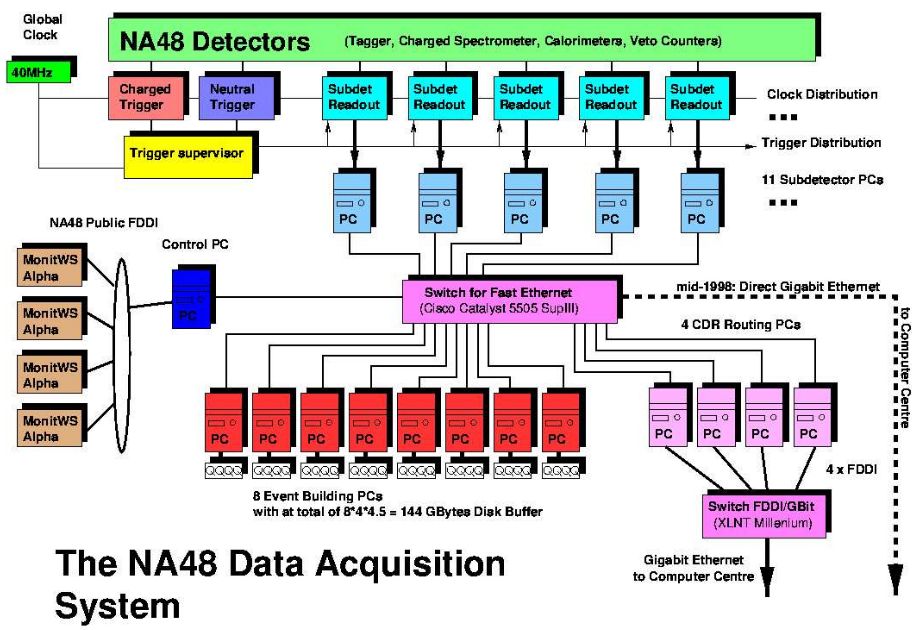

Figure 2.22: Schematic of the DAQ system.

at CERN. The data flow is $\sim 3TB$/day at full efficiency.

After some checks on the integrity of the data copied on the disks, the burstlets are processed and filtered by a software, the *L3*, which creates different output *streams*. The computer power needed is provided by the CERN batch system (lx-batch), to which jobs are submitted by a daemon running on CERN public PCs. After this the events are written on tape. There are two kinds of data written: *raw files*, which still contain unprocessed sub-detector information for selected events, and *Compact files*, which contain reconstructed information computed during the L3 processing

In 2003/2004 up to 5 different kind of streams were produced by the L3. A typical raw data file, containing data acquired during a whole burst, is $\sim$ 500 MB, while a Compact file is $\sim$ 120 MB.

2.6 Data taking

Data for NA48/2 analyses were collected during two different periods, in summer 2003 and 2004.

2.6.1 2003 data taking

In 2003 NA48/2 collected data for 80 days, from June 12th until September 8th. In addition, a week of proton beam at nominal conditions was used in May to setup the new beam line and test the detectors and trigger conditions. Another week, in which the beam's bunches were produced as envisaged for LHC (25 ns r.f. structure) were used for calibration and η runs, being useless for data taking. Three special runs with muons were taken to align DCH planes; for the same reason two low-intensity hadron beam runs were collected, during which the beam spot was deflected by ± 20 cm along the X, Y, U, V directions.

In order to minimize systematic effects, the spectrometers' magnet has been inverted every day, while the beam achromats were inverted on a weekly basis. A complete set of data including all possible magnet configurations, called a *super-sample*, is accumulated over a period of about two weeks.

Because of several problems with SPS (absence of beam, power cuts, cooling problems) the efficiency of the run was about 50%.

2.6.2 2004 data taking

The second phase of NA48/2 data taking lasted 90 days, from May 15th to August 18th 2004. The whole period was subdivided in two parts by a week of highly bunched protons for LHC tests; in the second part the readout was modified in order to decrease recorded data from $K^{\pm} \to \pi^{\pm}\pi^{+}\pi^{-}$ events and increase the bandwidth for other K decays and the trigger collection rate by 20% (6×10^5 trigger/burst).

In 2004 muon runs were frequently collected because of a slight shift in the chambers' transverse alignment observed in 2003 run; this precaution allowed to monitor the stability in DCH relative position at the level of 20 μm.

The last week of data taking was devoted to special runs, aiming at collecting data for semileptonic and leptonic kaon decay analyses, and tests for a possible future experiment, whose goal is that of collecting ~100 events of the rare $K^{+} \to \pi^{+}\nu\overline{\nu}$ decay. The project is currently in the R&D phase at CERN, under the name of P326/NA62.

Chapter 3

Analysis strategy

In this chapter the procedure to estimate the Ke3γ/Ke3 BR and A_ξ using the NA48/2 data will be described. The data samples on which the analysis was performed will be briefly reviewed in the last section.

3.1 Quantities to be measured

The quantities whose measurement represents the goal of the present work, the Ke3γ/Ke3 BR and the T-violation parameter A_ξ, were defined in Chapt. 2 from a theoretical point of view. Here the procedure adopted for their experimental estimation will be described, pointing out the experimental quantities (acceptances, BG estimation, trigger efficiency) required; their derivation will be described in the following chapters.

3.1.1 Ke3γ/Ke3 amplitude ratio

The measurement of an absolute BR in NA48/2 requires a precise knowledge of the absolute kaon flux, which in turn depends on the number of protons impinging on the beryllium target. Since this last quantity can be measured with very poor accuracy, the best experimental procedure is to compute a relative BR, normalizing the analyzed channel to a known one so that the flux dependence in the ratio is canceled. The flux of candidate events measured in the final data depends on the following quantities:

$$\Phi(channel) = \Phi(Kaon) \times P_{decay} \times BR^{ch} \times \epsilon^{ch}_{trig}/D^{ch} \times Acc^{ch} + \Phi(BG) \qquad (3.1)$$

where:

- Φ(Kaon) is the flux of kaons;

- P_{decay} is the probability that a kaon decays in the decay region;
- BR^{ch} is the BR of the channel considered;
- ϵ^{ch}_{trig} is the trigger efficiency for to that channel;
- D^{ch} is the (possible) downscaling factor for the trigger considered;
- Acc^{ch} is the acceptance (both geometric and relative to the event selection) of the channel considered;
- Φ(BG) is the total flux from background channels.

The choice of the normalization channel to be used must be done in such a way that:

- the number of events in the final state is much higher than for the channel under analysis, so that the statistical error related to the normalization channel is negligible;
- the final state of the normalization channel is as similar as possible to the analyzed channel; this allows the partial cancellation of systematic effects. For example, it is desirable that the two channels share the same trigger chain.

In the case of Ke3γ, the most natural choice is the normalization to the Ke3 decay, which has a very similar final state and a much higher BR ($\sim$ 5% with respect to $\sim 2{\cdot}10^{-4}$ of the Ke3γ).

For these reasons the measurement of R=BR(Ke3γ)/BR(Ke3) is considered: using the equation 3.1 to get the Ke3γ and Ke3 BR's as a function of the other variables, the expression becomes:

$$R = \frac{BR(K^{\pm} \to e^{\pm}\nu\pi^0\gamma)}{BR(K^{\pm} \to e^{\pm}\nu\pi^0)} = \frac{\Phi(Ke3\gamma) - \Phi(BG_{Ke3\gamma})}{\Phi(Ke3) - \Phi(BG_{Ke3})} \cdot \frac{\epsilon^{Ke3}_{trig} \times Acc^{Ke3}}{\epsilon^{Ke3\gamma}_{trig} \times Acc^{Ke3\gamma}} \tag{3.2}$$

where the downscaling factors $D^{Ke3\gamma}$ and D^{Ke3} cancel out because the trigger used for the two channels is the same (see Chapt. 7 for further details).

For the BR computation, events coming from negative and positive kaons can be used together.

3.1.2 A_ξ measurement

No normalization channel is needed for the measurement of A_ξ; in this case, however, positive and negative channels must be distinguished since, as discussed in Chapt. 1, the measurement is strictly sign-dependent. Every possible source of asymmetry for the ξ variable must be taken into account: one of these is the BG, which must be carefully computed and subtracted bin-by-bin. Every BG channel has a different shape in the ξ variable, as shown in fig. 3.1; this is due to the different kinematics of the decays.

The experimental quantity to be measured is then:

$$A_\xi = \frac{\sum_{bin+}(N_{ev}^{bin+} - N_{bg}^{bin+})\epsilon_{trig}^{+} - \sum_{bin-}(N_{ev}^{bin-} - N_{bg}^{bin-})\epsilon_{trig}^{-}}{\sum_{bin+}(N_{ev}^{bin+} - N_{bg}^{bin+})\epsilon_{trig}^{+} + \sum_{bin-}(N_{ev}^{bin-} - N_{bg}^{bin-})\epsilon_{trig}^{-}} \tag{3.3}$$

Where the + and - signs are referred to the sign of ξ (see Chapt. 1). For what concerns the trigger efficiency, which represents another potential source of asymmetry, it will be shown in Chapt. 7 that it plays no role in the A_ξ measurement.

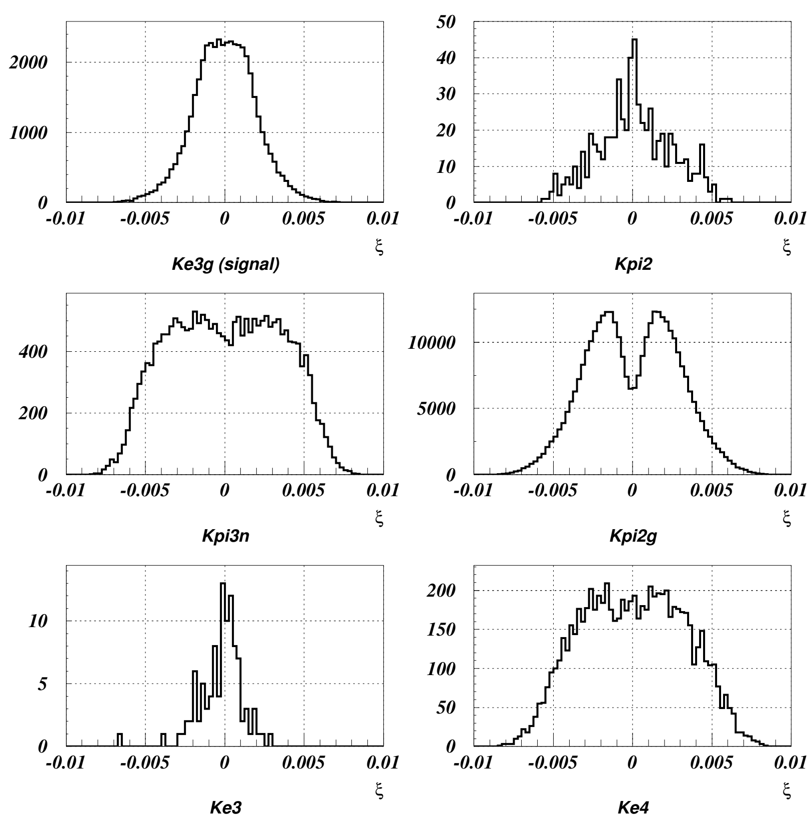

Figure 3.1: MC distributions in the ξ variable for signal and BG channels considered, after the selection and BG reduction cuts described in Chapt. 4 and 6.

3.2 Data Analyzed

The data analyzed to perform the estimation of the BR and of A_ξ were collected during the 2004 special run, consisting of 3 days of data-taking with minimum-bias trigger conditions from 12th to 14th August (see Chapt. 2). The reason why these data were used was the possibility that the L2 trigger, and especially the MBOX cut (see Chapt. 2 and 7), could bias the data collected in 2003 for the channels under analysis. The available statistics for this sample is lower with respect to the data collected during normal run, being just a few thousands (compared to some 10^5s) of events for Ke3γ, once the nominal cuts are applied.

As for the format of the data analyzed, it was chosen to perform the analysis on SUPERCOMPACT (SCMP) data. The SCMP format contains less information with respect to COMPACT data, but no selection is applied on them. Also the MC events analyzed, whose generation will be dealt with in Chapt. 5, were created in the SCMP format.

SCMP data, both real and MC, are then read using the same program; here loose cuts are applied and selected events are organized in Ntuples, where all the event information can in principle be written, which are more easily accessible and analyzable. Afterwards, the final selection is applied on Ntuples to get the final results. In this way one can avoid accessing the whole data sample (which, for the 2003 data only, is $\simeq$ 3 TB) for every variation in the analysis. The Ntuples produced were read and analyzed through PAW (Physics Analysis Workstation) [50].

Chapter 4

Selection of Ke3γ and Ke3 samples

The first step to compute the quantities described in Chapt. 3 is to select Ke3γ and Ke3 events in such a way that the residual BG is as low as possible. In this chapter the selection technique will be exposed, while in Chapt. 6 the cuts applied to reduce BG coming from different channels will be discussed, and the residual BG will be computed and subtracted from the selected events.

4.1 Track and energy reconstruction in NA48/2

At the SUPERCOMPACT level, the information collected by the detectors are already processed, and tracks and clusters (whose definition will be given in a while) are reconstructed and ready for the analysis. Here the procedure to obtain these two quantities is exposed.

4.1.1 Track reconstruction

The basic information from the DCHs is represented by a hit in a wire, i.e. by an electrical pulse over threshold and the related time information. A DCH cluster is defined if there is one hit in both planes of all the views (X, Y, U and V), the hits being associated through space coincidence. Front segments are then built for each view using hits from the same views in DCH1 and DCH2 (i.e. the chambers before the spectrometer magnetic field). Some of the front segments can be excluded if they do not point to the decay region. Using front segments, a front track is extrapolated to the decay region; the track can also be defined using 3 or 2 front segments, in case some of them were discarded. In order to be sure that the reconstructed front track comes from the decay region it must fulfill the condition to cross a 10 cm diameter cylinder whose axis coincides with the beam axis, as shown in fig. 4.1. Once a front track is computed, space points can be defined in DCH1 and DCH2 as their intersection with the front track, while the space point in DCH4 is computed using the computed cluster.

The second stage consists in introducing the time information: this leads to the rejection of those tracks whose space points are not consistent in time. A quality variable is also computed, which measures the fraction of hits close to the track average time.

Finally the hit positions in all DCH3 views of the track obtained in this way are computed, and the cluster from DCH3 (if any) can be added to the track if it is geometrically and timely consistent with these extrapolated hits. This also eliminates some ambiguities regarding DCH4 points compatible with two tracks (the so-called "ghost tracks").

4.1.2 LKr energy reconstruction

Once the electric pulses are collected by the LKr cells (see Chapt. 2) and converted into energies through calibration constants, the energy deposited in the LKr by a particle can be reconstructed once a way is defined to group the cells sharing the same energy deposit. This group of cells, i.e. a LKr cluster, is defined if the following requirements are met (at a given 25 ns clock cycle) [51]:

- one cell has a local maximum, i.e. it has more energy than any of its eight surrounding cells;
- the cell's energy is larger than 0.25 GeV;

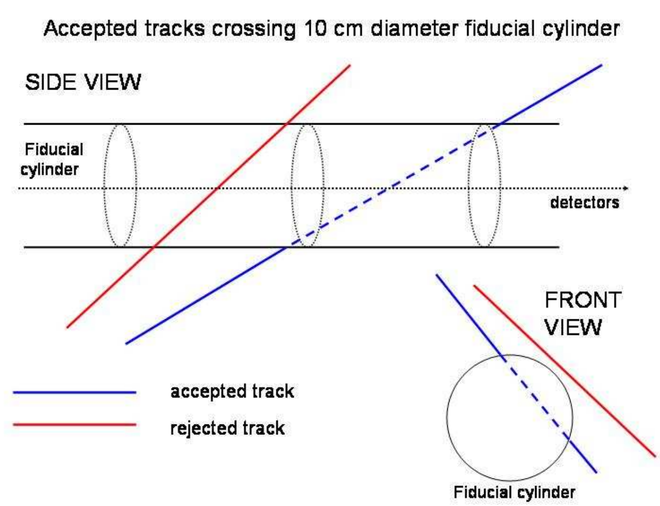

Figure 4.1: Reconstructed tracks must cross a 10 cm diameter cylinder whose axis coincides with the beam axis.

- the cell's energy satisfies the relation:

$$E > 0.18 + 1.8 \cdot E_{avg} \qquad \text{(E in GeV)} \tag{4.1}$$

where E_{avg} is the average energy (in GeV) of the eight surrounding cells.

Once a cluster is found, its position is estimated using the centre of gravity (COG) of the energy deposition in a 3×3 cell matrix. If a cell is within the cluster radius (11 cm from the COG) of more than one cluster at the same time, the energy of the cell is shared among the clusters according to the formula $E_i = E_{cell}(W_i/\sum_j W_j)$, where E_i is the energy fraction of the cell belonging to the cluster i and W_i is the expected energy deposited by the cluster i in the cell, computed using a first estimate of the cluster energy from the central cell, the cluster distance from the cell and the expected energy profile.

In the energy sharing, the time of the deposit is also considered, in case the cell receives contributions from two clusters at different times. After the sharing, new values for the energies and COGs of the clusters are computed. In case two clusters are closer than 11 cm the procedure is iterated, while if a very low energy cluster is close to a high energy one, its energy is assumed to come from the latter and the cluster is dropped from the list. If a dead cell is present in the cluster region, the energy collected in the good cells is used to estimate the energy deposited in the dead cell; the energy computed in this way is finally added to the cluster energy. Clusters whose center is closer than 2 cm to a dead cell are usually excluded from the list of used clusters in the analysis phase.

4.2 Ke3γ and Ke3 analysis

The selection of Ke3γ and Ke3 events requires the presence of a track measured by the spectrometer with a calorimetric cluster associated (the electron) and at least three other clusters (the two photons from the π^0 and the radiated γ) without any associated track; in case of Ke3 this number is two. The fact that two of these clusters come from the decay of the π^0 will introduce, as it will be shown in the following, further requirements on the event topology.

4.2.1 Track selection

Among the events reconstructed by the L3 trigger, those having one track compatible with an electron must be selected. Thanks to the space points reconstructed by the chambers it is possible to measure several quantities, e.g. the slope of the track before and after the magnet or the position of the particle while crossing the chambers.

Some fiducial cuts are applied: the particle position at the chambers is requested to be far from the beam pipe (to avoid BG coming from the beam halo) and from the edges of the chambers (to avoid edge effects). In addition the position of the charged vertex, defined as the point of minimum distance between the track and the beam axis, is required to be inside the decay volume (see fig. 4.3). A cut on minimum and maximum track momentum is also applied. The number of reconstructed tracks in the event is required to be equal to one.

An important tool to distinguish electrons with respect to other particles (typically muons or pions) is the ratio between the energy measured by the calorimeter and the momentum measured by the drift chambers, the so-called E/p. The association between a track and a cluster is made in the following way:

- the intersection of the track with the calorimeter surface is extrapolated;
- a LKr cluster is associated to the track if its position is within a distance of $\pm$ 5 cm from the track extrapolation,and if its time is compatible with the track time within 5ns;
- if more than one cluster fulfills the previous requirement, no cluster is associated to the track and the event is discarded.

Since the electrons' energy is almost totally absorbed by the calorimeter, the E/p ratio is close to 1, while this isn't true in general for other particles; as a consequence

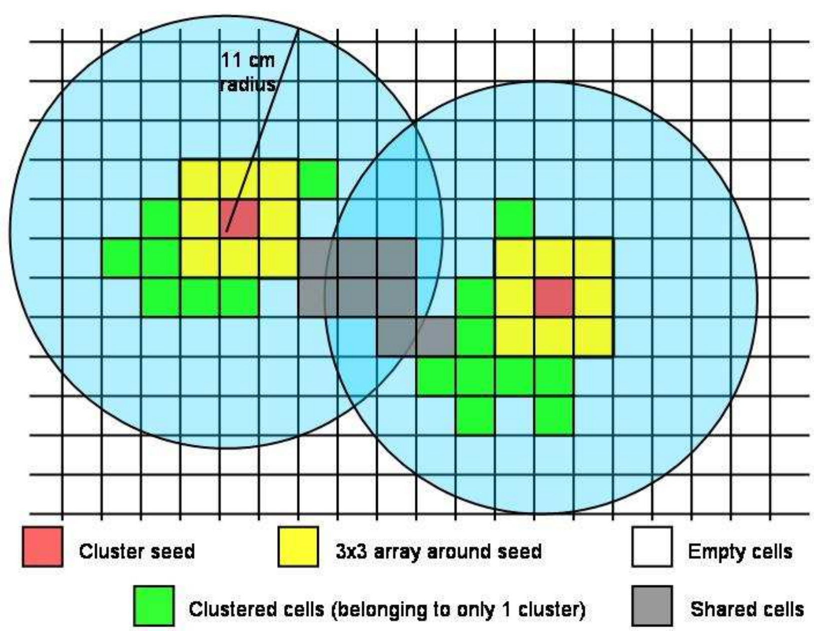

Figure 4.2: Schematics of a particle's energy reconstruction through clusterization.

a tight cut on this variable improves the rejection of particles which are not electrons. The E/p distribution of selected tracks (before the E/p cut) is shown in fig. 4.4. The effect of the E/p cut will be further investigated in the chapter dedicated to BG reduction.

In table 4.1 the nominal values adopted for the described cuts can be found. The charged vertex position along the Z axis is usually computed taking as a reference the AKS, where K_S were generated in NA48. This station is 12108.2 cm upstream of the LKr front surface.

Cut	Nominal value
P_{track}	5-35 GeV/c
DCH1 radius	12-120 cm
DCH4 radius	13-120 cm
Charged Vertex	-1000-7000 cm
track quality	> 0.6
E/p	0.95-1.05
$\|T_{cluster} - T_{trk}\|$	< 5 ns

Table 4.1: Nominal values of the cuts for track selection.

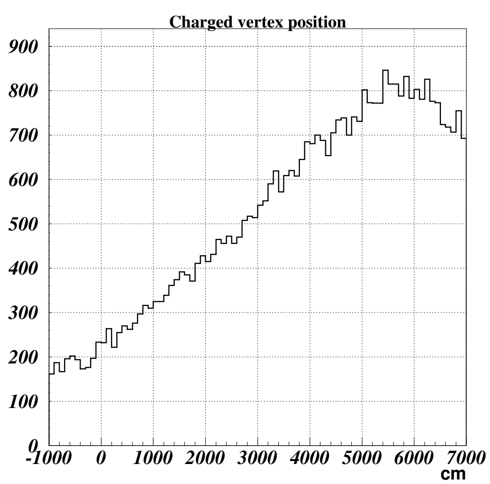

Figure 4.3: Charged vertex position.

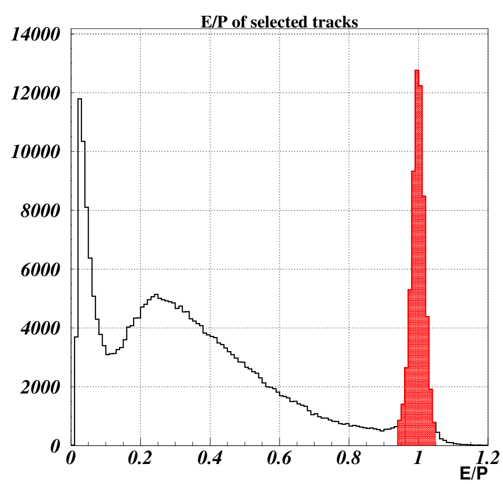

Figure 4.4: Distribution of E/p variable for selected tracks. The red area marks the events accepted by the E/p cut used in the present analysis.

4.2.2 Cluster selection

At least four clusters must be reconstructed to obtain a Ke3γ event; events with a number of "good" clusters less than four are rejected. A minimum distance of the cluster center from dead cells is imposed and a lower limit is required on its energy.

A cut on the point where neutral particles (either γ from π^0 decay or the radiative γ) cross DCH1 was also applied in order to avoid the effect of a flange housed in that position which is not well reproduced by MC. The cluster position on DCH1 was computed using the charged vertex. The distance of this point from the Z axis is requested to be > 14 cm.

A cut on the difference between the LKr cluster time and the time of the LKr cluster associated to the track is applied. The selected clusters are also required to have a minimum distance between each other.

In table 4.2 the nominal values used for these cuts are shown.

Cut	Nominal value
Cluster number	≥ 4
Cluster energy	> 3 GeV
$\lvert T^i_{clust} - T^{trk}_{clust}\rvert$	< 3 ns
Distance between clusters	> 10 cm
DCH1 cluster cut	> 13 cm

Table 4.2: Nominal cut values for LKr cluster selection.

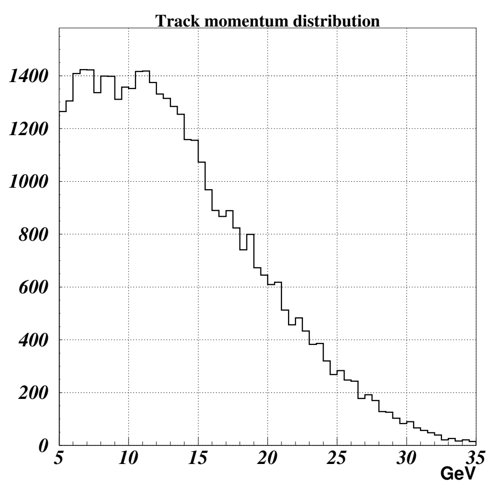

Figure 4.5: Momentum of selected tracks.

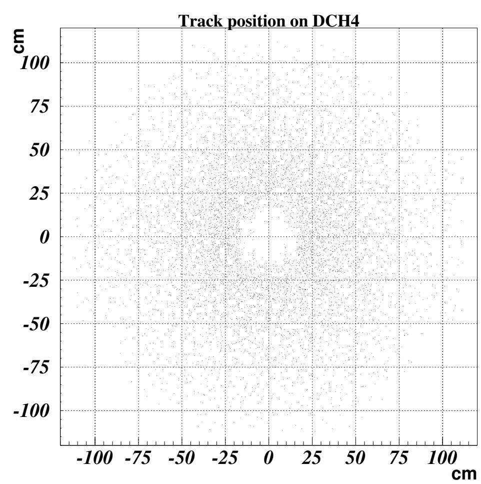

Figure 4.6: Hit position on DCH4 of selected tracks.

4.2.3 Pion and photon tagging

Once one track compatible with an electron and at least four good clusters are selected, one proceeds to identify clusters created by photons from π^0 decay, as well as the one created by the radiative photon.

The first step is to loop over all possible photon pairs and impose the π^0 PDG mass to evaluate the distance V_{π^0} of the π^0 decay vertex from the LKr calorimeter surface. The latter (V_{π^0}, also called "neutral vertex") is given by the expression 2.3.

A cut on the distance between the neutral and charged vertex (defined as the point of minimum approach between the selected charged track and the Z axis) is applied in order to select the best photon pair candidate. The pair for which this distance is the lowest is selected, provided its value is within $\pm$ 400 cm (see fig. 4.10). This cut can be understood by looking at the difference between the reconstructed neutral and charged vertex and the generated value of the vertex shown in fig. 4.9 for a sample of Ke3 events: the cut applied is $\sim 3\sqrt{RMS^2_{ntrl} + RMS^2_{chgd}}$, where RMS_{ntrl} and RMS_{chgd} are the root mean squares of the two distributions. If no pair fulfills this requirement the event is discarded; if there are more than one pair of clusters satisfying this condition, the event is also discarded, thus reducing the BG coming from events with two π^0s, like $K^\pm \to \pi^\pm\pi^0\pi^0$ or $K^\pm \to e^\pm\nu\pi^0\pi^0$.

Finally, in order to select the radiative photon, a loop is performed on the remaining clusters and the photon four-momentum is computed, assuming the neutral vertex as the decay vertex. The selected cluster is that which minimizes the missing squared mass of the event, i.e. the squared module of the difference between the kaon (assumed to be a particle of 60 GeV/c nominal momentum along the Z axis;

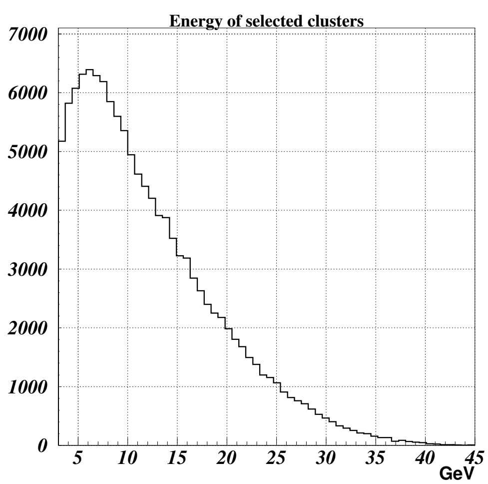

Figure 4.7: Energy distribution of selected clusters.

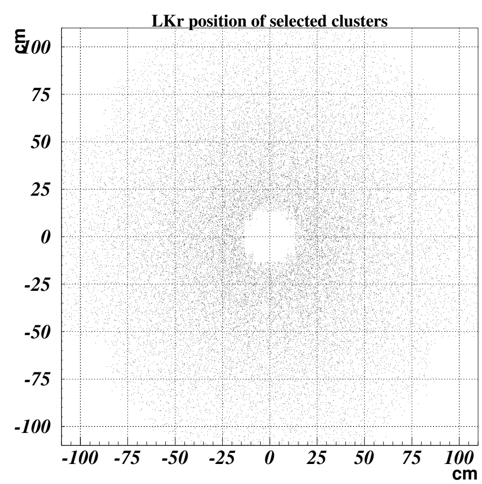

Figure 4.8: Position on LKr surface of selected clusters.

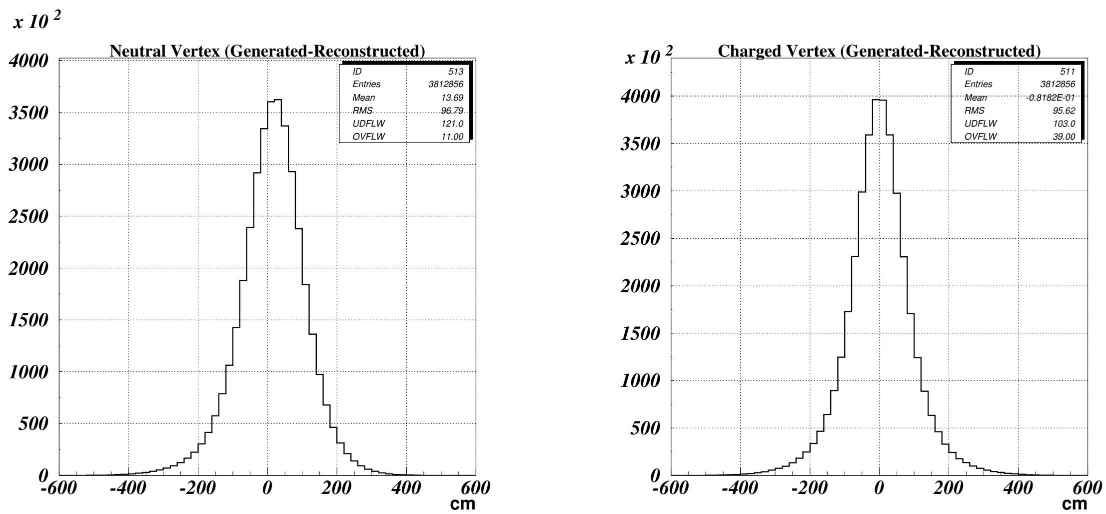

Figure 4.9: Neutral (left) and charged (right) vertex resolution, computed as the difference between reconstructed and generated MC quantities.

as stated in Chapt. 2, KABES was not used in this analysis due to the known mistagging problems) and the sum of the reconstructed particles' four-momenta:

$$M_\nu{}^2 = |\underline{K} - \underline{e} - \underline{\pi^0} - \underline{\gamma}|^2 \tag{4.2}$$

where the underlining stands for the 4-momentum of the particle. The distance between the cluster associated to the track and that associated to the radiative photon must be greater than 15 cm, in order to reduce the contamination coming from photons emitted by bremsstrahlung effect. Finally, the total energy E_{tot} of the reconstructed particles is requested to be lower than 66 GeV.

The selection of the Ke3 events is performed applying the same fiducial cuts used in the Ke3γ selection; this feature allows to better keep systematic effects under control. The only difference is that for Ke3 no additional photon must be selected and, as a consequence, the minimum number of clusters requested in this case is three. No cut is applied on the maximum number of clusters, both in Ke3γ and Ke3 analysis. The number of total clusters for selected Ke3γ and Ke3 events is shown in table 4.3; the events with additional clusters are mostly due to radiative events (i.e. with additional γ's in the final state) or to residual BG, which will be dealt with in Chapt. 6.

4.2.4 Infrared cuts

As pointed out in the first chapter, the computation of the Ke3γ/Ke3 BR can be performed once a cut is set on the infrared divergent variables, namely, in the rest frame of the kaon, the energy of the photon and the angle between the photon and

Number of clusters	% of events having N clusters	
N	Ke3γ	Ke3
3	-	96.84
4	95.92	3.09
5	3.96	0.057
6	0.078	0.0094
> 6	0.042	0.0054

Table 4.3: Percentage of events having N clusters for Ke3γ and Ke3.

the electron (which is a quasi-divergence, i.e. a divergence in the limit $m_{lepton} \to 0$). The nominal cuts which will be used in the present work are:

$$E^*_\gamma > 30 \text{ MeV} \qquad \theta^*_{e\gamma} > 20^\circ$$

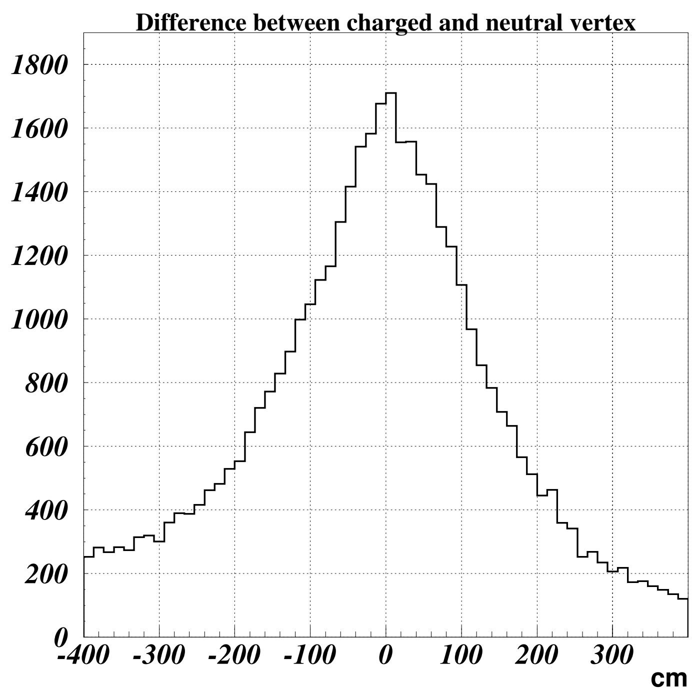

Figure 4.10: Distribution of the difference between charged and neutral vertex for the selected Ke3γ sample. The difference between right and left tail is due to the Ke3 BG contamination, which also slightly shifts the mean value from 0. The asymmetry is well reproduced by MC, as shown in fig. 4.11.

where E^*_γ and $\theta^*_{e\gamma}$ are the photon energy and photon-electron angle in the kaon rest frame.

Some attention must be payed when generating Ke3γ MC events regarding the IR cut imposed, because of resolution effects; this issue will be dealt with in the chapter on MC production and its comparison with data.

No explicit infrared cut is applied in the Ke3 selection; however emission of soft photons is simulated in the Ke3 MC, their presence affecting the kinematical properties of selected particles ($e^\pm$ and π^0) and the acceptance computation.

In table 4.4 the cuts applied in Ke3γ and Ke3 selections are summarized. As already mentioned, the two selections are very similar, this being a consequence of the fact that the two chosen final states are very much alike. Differences will arise, however, when the BG suppression cuts will be addressed in Chapt. 6, as the BR

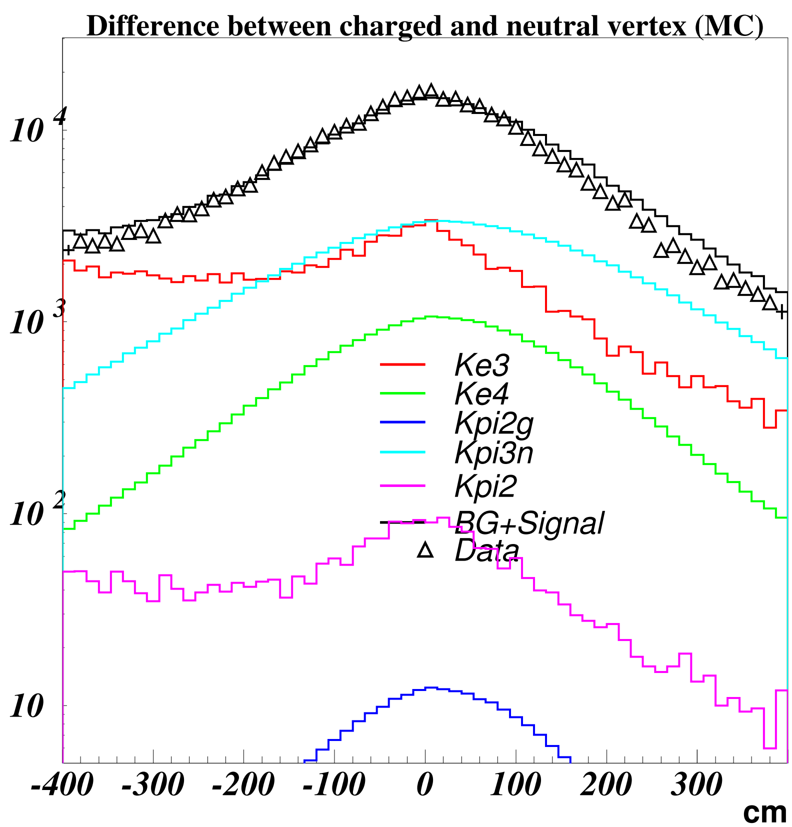

Figure 4.11: Difference between charged and neutral vertex for MC generated Ke3γ events and the relative BG. Cuts aiming at reducing the BG, discussed in Chapt. 6, are not applied here.

difference between the two decays (about two orders of magnitude) is such that BG sources from other decay modes play different roles.

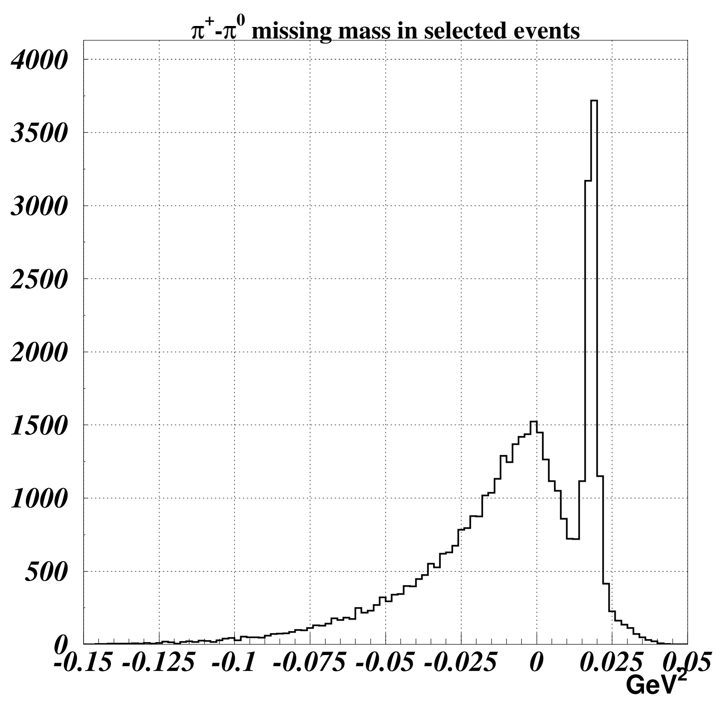

Figure 4.12: Electron-pion squared missing mass ($MM^2 = |K^\pm$ -$e^\pm - \pi^0|^2$) before BG reduction cuts. A peak is clearly visible at $MM^2 = m^2_{\pi^0}$, due to the $K^\pm \rightarrow \pi^\pm\pi^0\pi^0$ contamination.

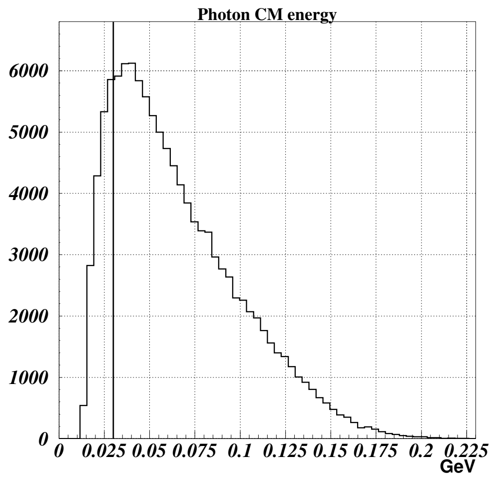

Figure 4.13: CM photon energy in selected Ke3γ events. The line corresponds to the IR cut.

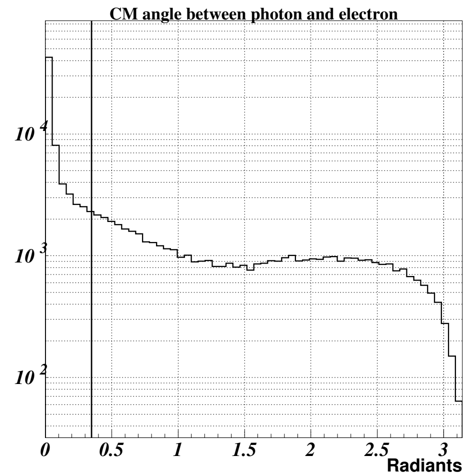

Figure 4.14: CM angle between electron and photon in selected Ke3γ events. The line corresponds to the IR cut.

Selection cuts	
Cut applied	Nominal value
Charged-neutral vertex distance	$\pm$ 400 cm
e-γ cluster distance on LKr	> 15 cm (Ke3γ only)
E_{tot}	< 66 GeV
E^*_{γ}	> 30 MeV (Ke3γ only)
$\theta^*_{e\gamma}$	> 20° (Ke3γ only)

Table 4.4: Cuts applied to select Ke3γ and Ke3 events.

Chapter 5

Monte Carlo simulation

A GEANT3-based Monte Carlo (MC) simulation has been used in this analysis to produce events for both the signal and the normalization channel, in order to compute the Ke3γ and Ke3 acceptances and compare the distributions obtained for data and MC events. The decay channels representing a BG for the analyzed decays were generated as well; the study of their kinematical properties allowed to improve the rejection power of the cuts applied in the analysis and to estimate the residual BG in the selected samples (see Chapt. 6).

5.1 CMC

The MC simulation used is the official one of the NA48/2 experiment, called CMC [52]. It includes a full GEANT-based simulation of the apparatus, from the kaon generation on the beryllium target up to the detector signals of the decay products. The simulation includes:

- a detailed description of the detector's geometry;
- effects of LKr dead cells and of DCH wire inefficiencies;
- interaction of radiation with matter, e.g. pair production and bremsstrahlung;
- possibility to generate a decay according to a matrix element (ME) implemented by the user. In absence of a ME the decay is generated according to phase space;
- secondary production of particles (e.g. $\pi^{\pm} \to \mu^{\pm}\nu$ decay);
- implementation of some known effects, like the presence of a residual magnetic field in the decay volume (see section 5.5).

The initial event is generated using a hit-and-miss technique according to a weight, which is given by the product of the ME and the phase space. The data (four momenta, decay vertices, possible secondary decays) of the final particles produced are then processed by GEANT, which simulates their passage through the experimental apparatus and the reconstruction of the measured quantities by the detectors. The data output is the same as for real data (COMPACT and SUPER-COMPACT files), so that the same analysis tools can be used. The MC generated quantities are available in the output and can be compared with the reconstructed ones.

Some aspects of the reconstruction are not well simulated by CMC. This is the case, for example, of time measurements (e.g. the time measured by the hodoscope as it is crossed by a charged particle), or the EM shower development of pions inside the calorimeter (due to the poor theoretical knowledge of hadronic particles' interaction with matter). In Chapt. 6, dedicated to BG reduction, a way to obtain this information directly from the data will be discussed.

5.2 Ke3γ and Ke3 generation

Since the Ke3γ decay was not among those already implemented in the CMC code, one of the first tasks of the analysis shown in this thesis was to provide a suitable ME to be put in the production routine. The code used in the theoretical work [28] was first adapted to work in the CMC environment, and then events were generated according to it.

One problem to overcome was the presence of infrared cuts in the ME computation. Since the event generation relies on a hit-and-miss technique using the ME value as a weight, if the ME is divergent in some kinematical variables the generation of MC events without infrared cuts would require an infinite time to reasonably fill the whole phase space. As a consequence, as shown in Chapt. 1, the theoretical computation of the relative branching fraction comes with well-defined infrared cuts. On the other hand the cuts on infrared variables in MC generation must be chosen taking into account experimental resolution effects, which cause a migration of events between adiacent bins. Taking E^*_γ as an example, part of the events with $E^*_\gamma < 30$ MeV will drift into the $E^*_\gamma > 30$ MeV area, and vice-versa. If however the MC generation is limited to the production of events with $E^*_\gamma > 30$ MeV, the events belonging to the $E^*_\gamma < 30$ bins that could migrate in the accepted area are not taken into account.

The solution is to produce a MC sample with infrared cuts which are more inclusive than the nominal cuts by the resolution width. The acceptance ACC(MC)=$\bar{N}/N$ used in the BR computation will then be the ratio of simulated events $\bar{N}$ falling within the infrared cuts and the number of generated events N whose infrared divergent variables are *strictly* above the infrared cut at MC generation.

For what concerns the MC generation of the normalization channel (Ke3), the ME used in the already published Ke3 analysis [24] was used, which also includes radiative corrections [53]. In the case of Ke3γ, the ME used shows some theoretical uncertainties mostly due to radiative and isospin-breaking corrections missing, which will be discussed in the last chapter.

The generation of events for Ke3γ and Ke3 was performed proportionally to the number of selected events in each run analyzed: this is because the MC is tuned in a run-by-run way in order to reproduce time-dependent effects, e.g. beam variations between runs, which are monitored during the data-taking and can translate into an acceptance variation. In fig. 5.1 the number of events selected are shown for Ke3γ and Ke3, relatively to the positive charge, for the 12 runs analyzed.

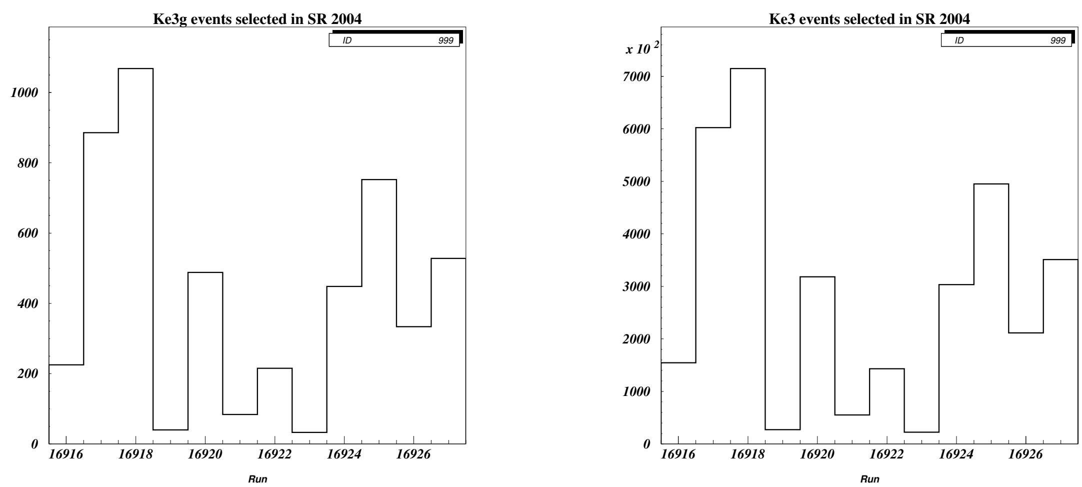

Figure 5.1: Events selected in the runs composing the special run 2004 (runs 16916-16927) for Ke3γ and Ke3 events.

5.3 Background generation

The possible sources of BG to the Ke3γ channel will be discussed in detail in the next chapter. In table 5.1 a summary of the considered channels is shown, pointing out the number of events generated for each BG channel.

One can note that the number of events generated for the Ke3 BG is much higher with respect to the other BGs. This is due to the fact that, even if the acceptance for this BG channel is low, once the residual BG events are rescaled for the ratio of the decay amplitudes, it becomes sizable; however a limited number of events means a high uncertainty on the residual BG, this being the reason why the number of generated Ke3 sample is bigger. In the next chapter Ke3 will be shown to be one of the most sizable BG to the Ke3γ.

Channel	Generated events ($\cdot 10^6$)	
	positive	negative
Ke3	72	36
Ke4	24	12
Kpi3n	24	12
Kpi2	24	12
Kpi2g	24	12

Table 5.1: BG MC events generated with CMC.

5.4 Ke3γ and Ke3 acceptance computation

The Ke3γ and Ke3 acceptances needed for the BR computation (see Chapt. 3) were computed as the ratio of the events passing the selections for the two channels and the total number of events generated. The number of generated Ke3γ events was such to make the statistical error associated to the acceptance negligible with respect to that associated to the selected events on data: the Ke3γ MC sample is larger by a factor ~ 10 relative to the number of Ke3γ selected in data. For the Ke3 sample the number of MC events after the selection is approximately equal to the events selected in data, hence their statistical uncertainty is of the same order; however the Ke3 has a much higher statistics with respect to Ke3γ and its contribution to the statistical uncertainty in the BR computation is negligible.

In tables 5.2 and 5.3 the number of generated events for signal and normalization channel and the computed acceptances for the two channels are respectively shown. As already stated, they were generated proportionally to the number of events selected in real data for each run.

Channel	Generated events ($\cdot 10^6$)	
	positive	negative
Ke3γ	2.1588	1.2546
Ke3	36.009	19.883

Table 5.2: Number of generated events for Ke3γ and Ke3 channels.

There is a small difference in acceptance between positive and negative events, which is more evident in the case of Ke3 data: the reason lies in the different shape of the positive and negative beams, which go through different paths in the NA48/2 experiment. During the 2004 SR the achromat polarity was left unchanged, while the DCH's magnetic field polarity has been swapped once. In fig. 5.2 the distance of the track's closest point (CDA) to the Z axis is averaged in bins of the azimuthal angle, for positive and negative events, relatively to the run 16918, i.e. the run with

Channel	Acceptance	
	positive	negative
Ke3γ	(1.6168$\pm$0.0095)%	(1.632$\pm$0.012)%
Ke3	(6.8679$\pm$0.0044)%	(6.7381$\pm$0.0058)%

Table 5.3: Acceptances for Ke3γ and Ke3 computed using MC events.

the highest statistics. One can note that the CDA distribution is almost flat for the negative beam, while the positive one is peaked at $\phi=\pi/2$, $3\pi/2$, this meaning the shape of the beam had an ellipsoidal rather than circular shape. The MC reproduces the effect in a good way, thanks to its tuning with the inclusive channel $K^{\pm} \to \pi^{\pm}\pi^{+}\pi^{-}$.

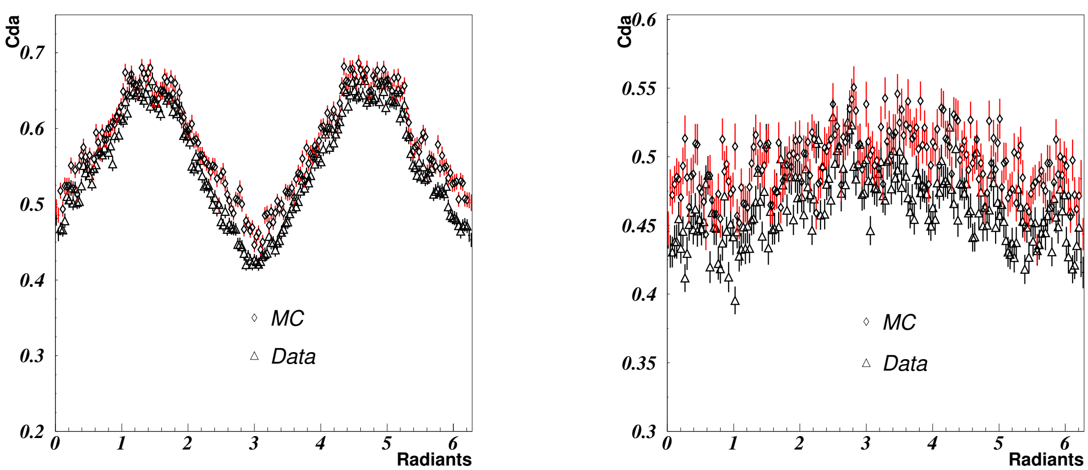

Figure 5.2: CDA projection in bins of the azimuthal angle for positive (left) and negative (right) events, in data and MC.

5.5 Corrections on data and MC samples

Several effects, whose result was to distort the detectors' measurements, had to be taken into account in the MC simulation.

In the following a brief explanation of these effects is given.

- **Field in the blue tube:** the presence of a small magnetic field (called blue tube field) in the decay region was already discussed in Chapt. 2: its effect is to slightly shift charged particles with respect to their initial direction. Using the 2003 blue field measurements, a correction was applied to the spectrometer data in order to correct (i.e. as if the blue field was not present) the track direction, and to obtain real values of positions and slopes on the DCHs.

- **Spectrometer corrections:** the so-called α and β corrections allow respectively to take into account possible misalignements of the drift chambers and differences between positive and negative magnetic field absolute values. The technique used was to reconstruct the kaon invariant mass using $K^{\pm} \to \pi^{\pm}\pi^{+}\pi^{-}$ decays: in the presence of a misalignment of one of the chambers the energy of the positive pions, for a given orientation of the spectrometer magnetic field is, for example, underestimated, while that of the negative pion is overestimated: as a consequence $\mathrm{M(K^+)}<\mathrm{M}_{PDG}$ and $\mathrm{M(K^-)}>\mathrm{M}_{PDG}$ and the sign of the inequalities flips when the spectrometer magnetic field is inverted.

  One can compute the kaon mass as a function of the run and to correct the measured momentum according to the formula:

$$P_{corr} = P_{meas} \cdot (1 + \eta \alpha P_{meas}) \tag{5.1}$$

  where $\eta = \pm 1$ according to the pion's charge and:

$$\alpha = -sign(B) \cdot \frac{< M(K^+) > - < M(K^-) >}{1.7476} \tag{5.2}$$

  where 1.7476 is an empirical number relating the positive and negative mass difference to the measured momentum difference.

  The fact that $M(K^+)$ and $M(K^-)$ are not centered at the kaon PDG mass is due to the fact that $|B^+|$ and $|B^-|$ could not be exactly the same. This is corrected by introducing the parameter β, defined as:

$$\beta = -\frac{< M(K^{\pm}) > - M(K)_{PDG}}{0.2 \cdot M(K)_{PDG}} \tag{5.3}$$

  and multiplying P_{corr} defined in 5.1 by a factor $(1+\beta)$.

- **Projectivity correction:** the geometry of the LKr cells is such that their axis is pointing at a distance D=110 m in front of the LKr surface. If a particle originates close to this point, the cell on which it impinges on the LKr is parallel to the particle's trajectory, and the amount of energy deposited in the neighbouring cells is only due to the shower's lateral development (parametrized by the LKr Moliere's radius). However, if the decay vertex is far from this point, the particle's trajectory can cross the neighbouring cells, as shown in fig. 5.3, and the amount of energy deposited per cell also depends on the shower's energy and hence on its depth: this causes a slight error when computing the transverse coordinates of the cluster center.

To account for this effect a correction is applied. The depth d_{cal} of the EM shower produced by a particle in the LKr depends logarithmically on the energy of the shower and is computed using a parametrization whose coefficients are estimated through MC simulation. It can be easily shown that the real position X_{real} (and analogously Y) of the shower impact point is obtained, starting from the uncorrected position X_{meas}, with the formula:

$$X_{real} = X_{meas}(1 + \frac{d_{cal}}{D} - \frac{d_{cal}}{V}) \tag{5.4}$$

where V is the reconstructed vertex position of the particle.

- **Non-linearity correction:** a LKr non-linearity in the cluster reconstruction was found using neutral Ke3 decays and studying the E/p behaviour of isolated electrons; the effect is mostly due to the zero-suppression applied on the LKr cells by the Data Concentrator (see Chapt. 2). It was found that the correction is negligible for cluster energies above 11 GeV, while under this threshold the correction can be parametrized in terms of the measured energy as follows:

$$\Delta E = E_{real} - E_{meas} = a_1 + a_2 E_{meas} + a_3 E^2_{meas} + a_4 E^3_{meas} \quad (\mathrm{E}_{meas} \text{ in GeV}) \tag{5.5}$$

$$a_1 = 0.039 \qquad a_2 = -0.0104 \qquad a_3 = 9.3 \times 10^{-4} \qquad a_4 = -2.84 \times 10^{-5} \tag{5.6}$$

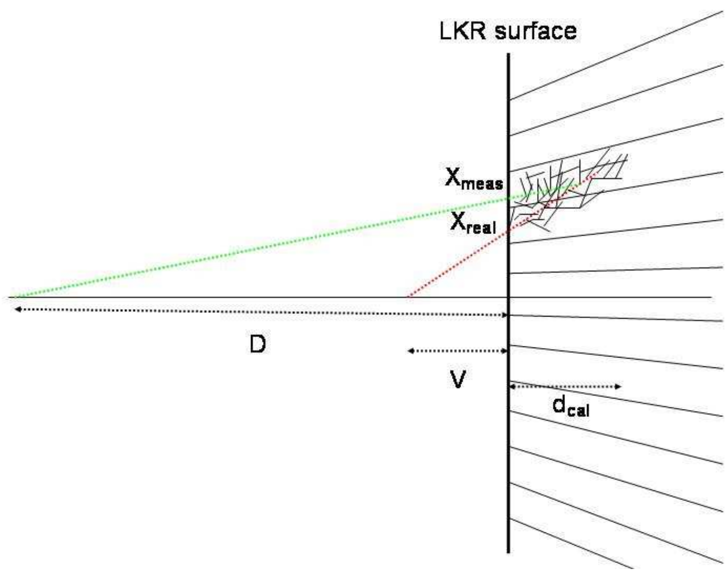

Figure 5.3: Projectivity effect induced by the pointing geometry of LKr cells.

Below 3 GeV the LKr behaviour becomes highly non-linear. The clusters selected for this analysis were required to be above this threshold.

5.6 Data and MC comparison

To check the validity of the MC sample produced, some data/MC comparisons were performed. Differences between data and MC could arise if one of the following things happens:

- The matrix element used does not reproduce well the decay over the whole phase space;
- The MC simulation doesn't reproduce all the detector's effects;
- The presence of unaccounted BG biases data distributions.

In the following plots the cuts used to reduce the BG, which will be discussed in Chapt. 6, are already applied.

5.6.1 Ke3γ Data/MC comparison

Data and MC event distributions for the signal channel are in good agreement. Some of the most significant variables are shown in the following plots.

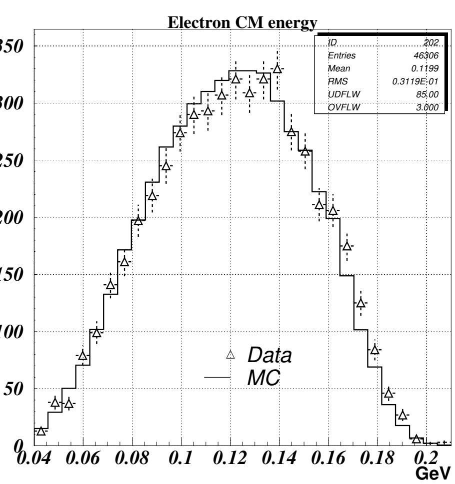

Figure 5.4: Electron CM energy distribution for Ke3γ events (data and MC).

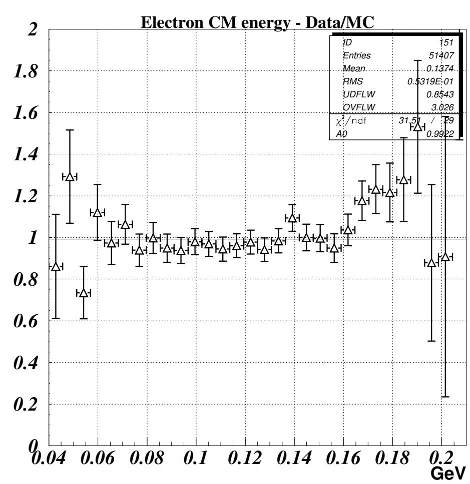

Figure 5.5: Electron CM energy data/MC ratio for Ke3γ events.

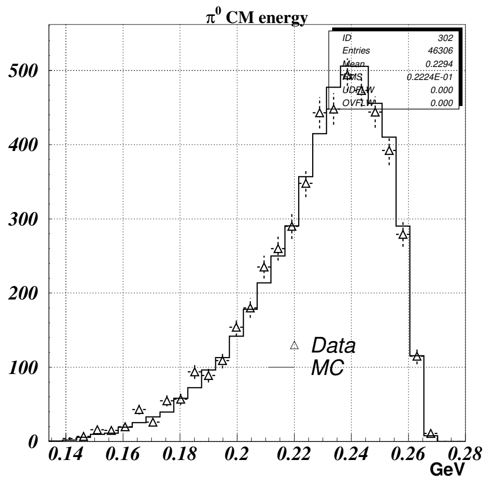

Figure 5.6: Pion CM energy distribution for Ke3γ events (data and MC).

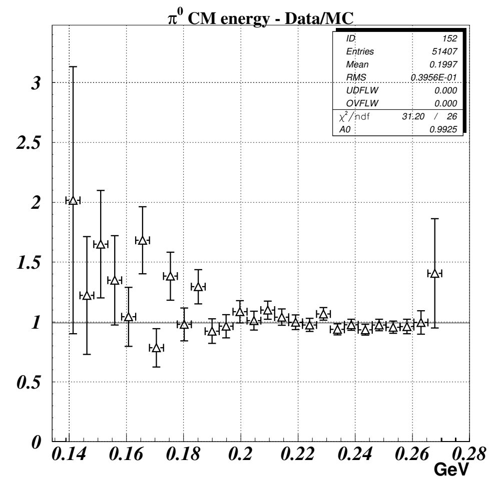

Figure 5.7: Pion CM energy data/MC ratio for Ke3γ events.

5.6.2 Ke3 Data/MC comparison

The data/MC ratio for the normalization channel is acceptable, even if differences of few percent arise in some distributions. In the following plots some distributions are shown.

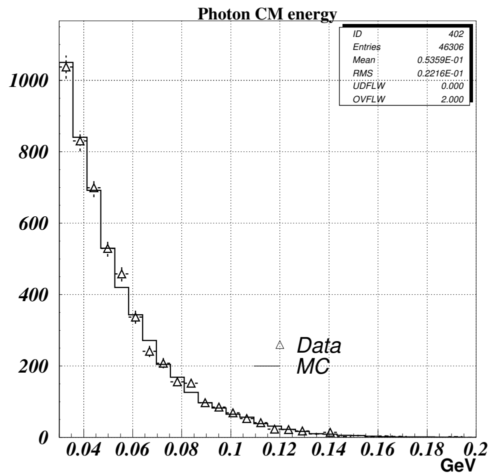

Figure 5.8: Photon CM energy distribution for Ke3γ events (data and MC).

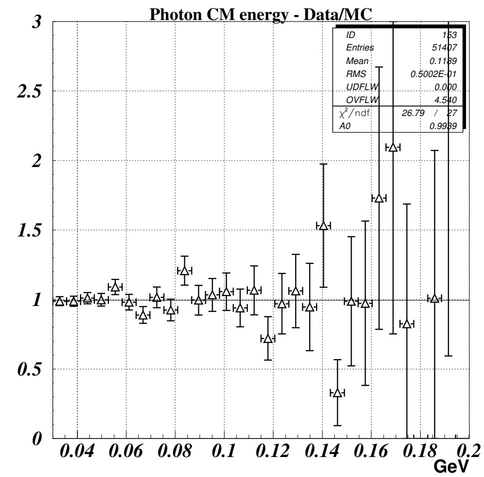

Figure 5.9: Photon CM energy data/MC ratio for Ke3γ events.

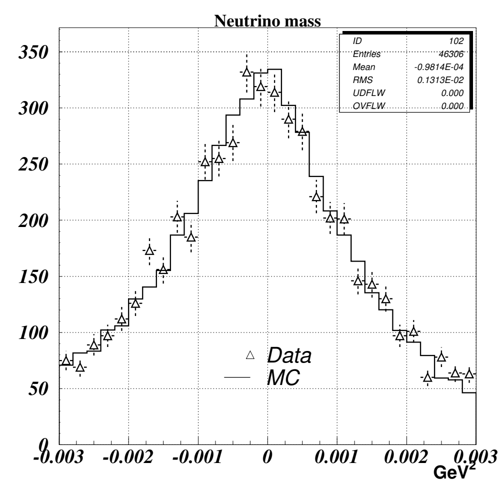

Figure 5.10: Missing squared mass distribution for Ke3γ events (data and MC).

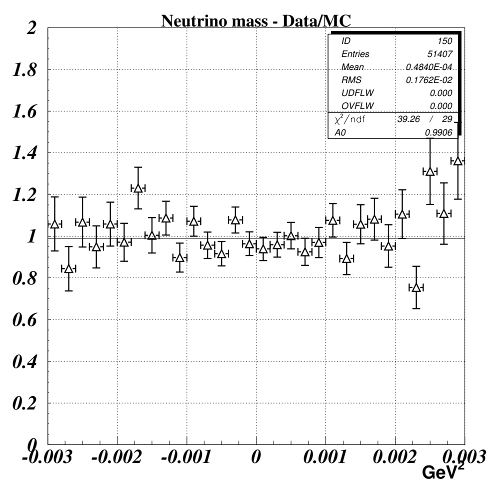

Figure 5.11: Missing squared mass data/MC ratio for Ke3γ events.

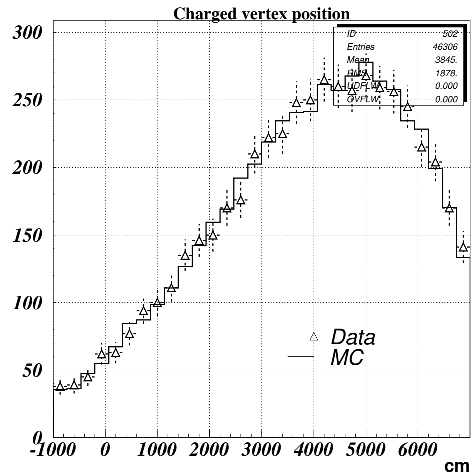

Figure 5.12: Charged vertex position for Ke3γ events (data and MC).

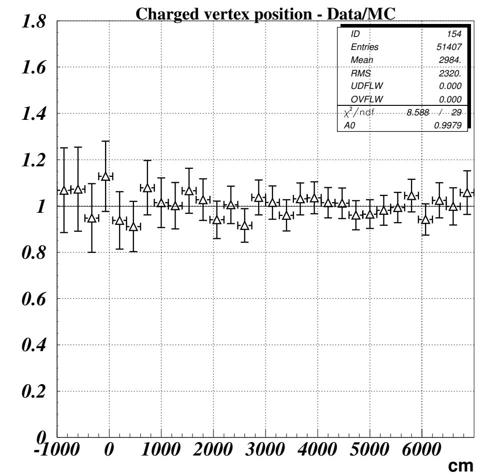

Figure 5.13: Charged vertex position data/MC ratio for Ke3γ events.

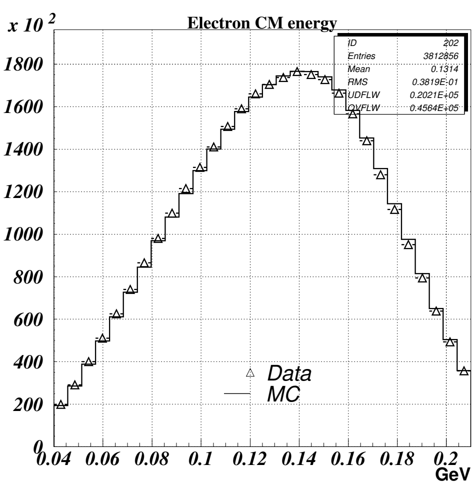

Figure 5.14: Electron CM energy distribution for Ke3 events (data and MC).

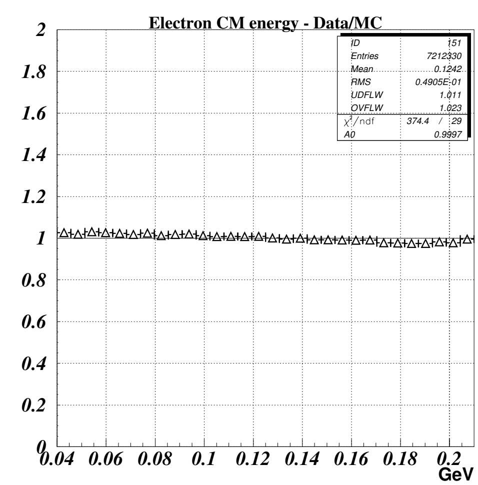

Figure 5.15: Electron CM energy data/MC ratio for Ke3 events.

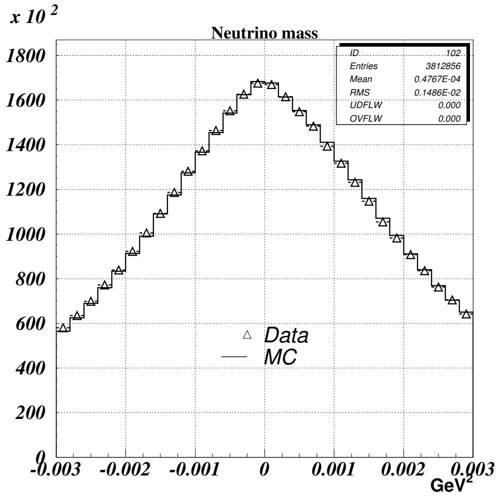

Figure 5.16: Missing squared mass distribution for Ke3 events (data and MC).

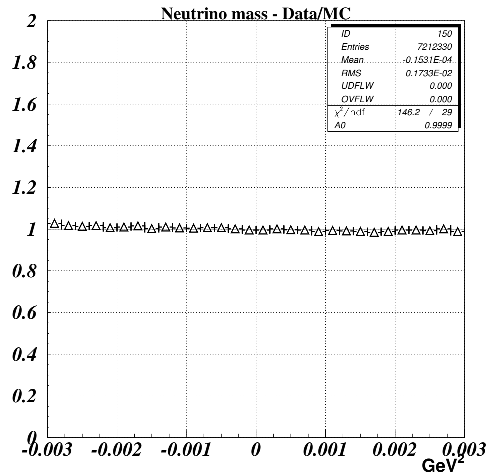

Figure 5.17: Missing squared mass data/MC ratio for Ke3 events.

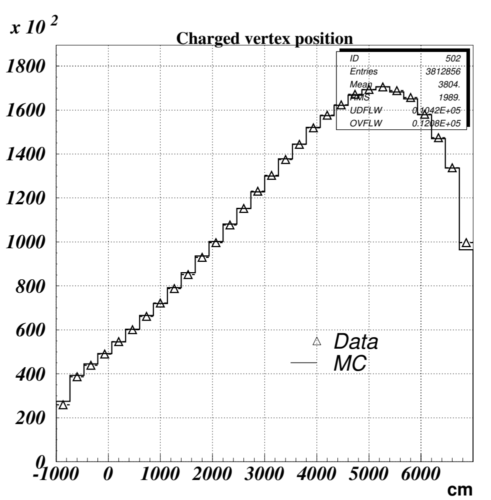

Figure 5.18: Charged vertex position for Ke3 events (data and MC).

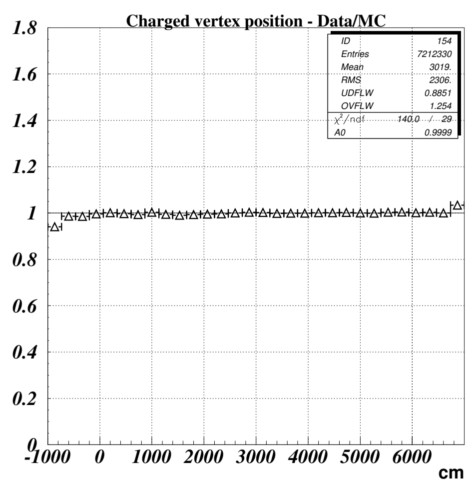

Figure 5.19: Charged vertex position data/MC ratio for Ke3 events.

Chapter 6

Background reduction

The BG reduction on data selected with the cuts described in Chapt. 4 represents a crucial part of the present analysis. The Ke3γ channel, the BR being of order 10^{-4}, can receive contributions by many different channels, some of which are up to two orders of magnitude larger. The presence of the neutrino implies that not all the particles produced can be detected; as a consequence one can cut on the missing mass of the event, rather than kaon mass, to tag the event.

The process of BG reduction is closely related to the analysis of MC generated data for the BG channels, with the goal of exploiting their different kinematical properties (with respect to the Ke3γ signal) to select a sample as clean as possible.

In this chapter the possible BGs for Ke3γ and Ke3 will be first discussed, pointing out the way in which they can reproduce the final state of the channels under analysis. Afterwards the cuts applied to reduce the BG will be listed, together with their effect on the signal. Finally the residual contamination will be subtracted.

6.1 Standard tools to reject BG

Some quantities can be used in order to distinguish the signal from BG, which can be related either to the event kinematics or to the way different particles interact with the detectors. These quantities are:

- **E/p ratio**: the ratio between the energy measured by the calorimeter and the momentum measured by the spectrometer for charged particles, already introduced in Chapt. 4. This should peak close to 1 for electrons, since all their energy is released in the 27 radiation lengths of the calorimeter, and be usually less than 1 for muons and pions.

- **Invariant mass**: in decays were no neutrino is produced and all the visible particles are within the acceptance, the invariant mass of the event can be computed:

$$M_{part} = \sqrt{|\sum_i \underline{p_i}|^2} \tag{6.1}$$

where $\underline{p_i}$ is the four-momentum of the i-th reconstructed particle. In case of kaon decays, this quantity should peak at the kaon mass, at ~ 0.493 GeV/c^2. This variable can be used, for example, in the decay $K^\pm \to \pi^\pm\pi^0$, with the charged pion mislabelled as electron. In this case a cut around the K mass eliminates most of the BG;

- **Missing mass**: another tool to distinguish different decays is the missing squared mass of a particle (or a group of particles), which is defined as:

$$MM^2_{part} = |\underline{K} - \sum_i \underline{p_i}|^2 \tag{6.2}$$

Here $\underline{K}$ represents the kaon four-momentum, which is assumed to be along the Z axis with the nominal momentum of 60 GeV/c, while the sum is over all the particles one wants to compute the missing mass of. For example, in the decay $K^\pm \to \pi^\pm\pi^0\pi^0$ the missing mass squared of the charged pion and a neutral pion peaks around the π^0 squared mass.

6.2 Background channels to the Ke3γ decay

Contributions to the Ke3γ background come from both leptonic and non-leptonic channels; these two BG categories can be treated separately.

6.2.1 Non leptonic channels

For these channels there is at least a charged pion track from the kaon decay, so the contribution of this decay can be strongly reduced using the E/p variable. Neverthless a relevant BG from high BR decay modes remains also after this cut, so that other ways to reduce BG must be devised.

$K^\pm \to \pi^\pm\pi^0$ (Kpi2) decay

The Kpi2 decay can contribute to the Ke3γ background if the pion is mislabelled as an electron and another cluster is detected, either accidentally or if part of the pion shower is reconstructed as an extra cluster. The reconstructed invariant mass of the charged track (once it is assigned the charged pion mass) and the π^0 should be distributed around the Kaon mass, as it is shown in fig. 6.1.

$K^{\pm} \to \pi^{\pm}\pi^0\pi^0$ (Kpi3n) decay

The Kpi3n decay can contribute to the Ke3γ signal if one photon from the two π^0's is lost, either because it is out of acceptance or its energy deposit in the LKr is not reconstructed as a cluster, while the remaining photon mimics the radiative γ. In this case the missing squared mass of the track (once it is given the π^+ mass) and of the π^0 peaks at the π^0 squared mass, as it is shown in fig. 6.2.

$K^{\pm} \to \pi^{\pm}\pi^0\gamma$ (Kpi2γ) decay

The Kpi2γ final state is very similar to the Ke3γ: as a consequence the acceptance for this channel is much higher with respect to other non leptonic channels (but it is equally highly suppressed by the E/p cut) and the BG to Ke3γ can in principle be sizable even if the Kpi2γ BR is roughly an order of magnitude lower.

6.2.2 Leptonic channels

In the leptonic channels the presence of the neutrino prevents the reconstruction of all the particles produced.

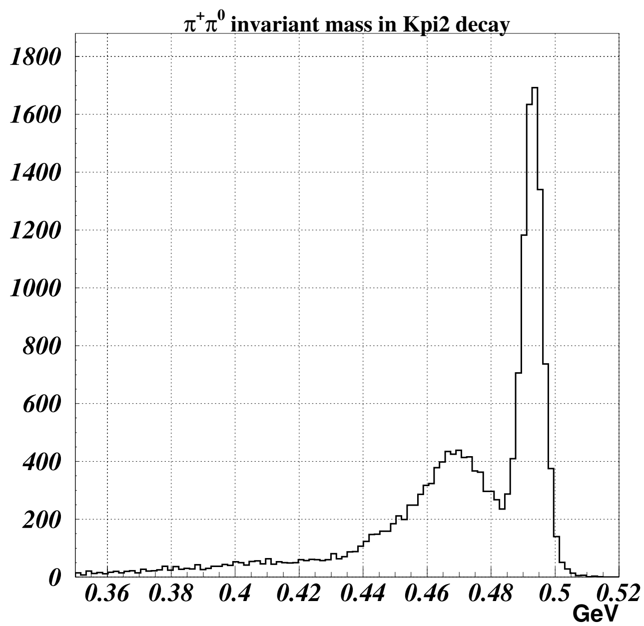

Figure 6.1: Invariant mass of the $K^{\pm} \to \pi^{\pm}\pi^0$ decay (MC), attributing the π^+ mass to the track, and considering the track and the π^0 selected through the Ke3γ analysis.

$K^{\pm} \rightarrow e^{\pm}\nu\pi^{0}$ (Ke3) decay

The Ke3 contribution to the Ke3γ signal can be caused by the presence of an accidental cluster simulating the radiative photon. However there's a more relevant contribution caused by the conversion of one of the photons from the π^0 decay after DCH1 and by the bremsstrahlung photons emitted by the charged lepton in the material crossed before the spectrometer magnet. The technique to tag and eliminate this BG will be discussed in the next section, when the cuts applied to reject the BG will be shown. A sketch of the ongoing processes is shown in fig. 6.3 and 6.4.

$K^{\pm} \rightarrow e^{\pm}\nu\pi^{0}\pi^{0}$ (Ke4) decay

This channel contributes to the BG when one of the photons from the decay of the π^0's is out of acceptance or goes undetected. Since the charged track is an electron, the E/p cut is not effective in reducing this BG; however the contamination of this channel is negligible as the BR of the decay is one order of magnitude smaller than the Ke3γ.

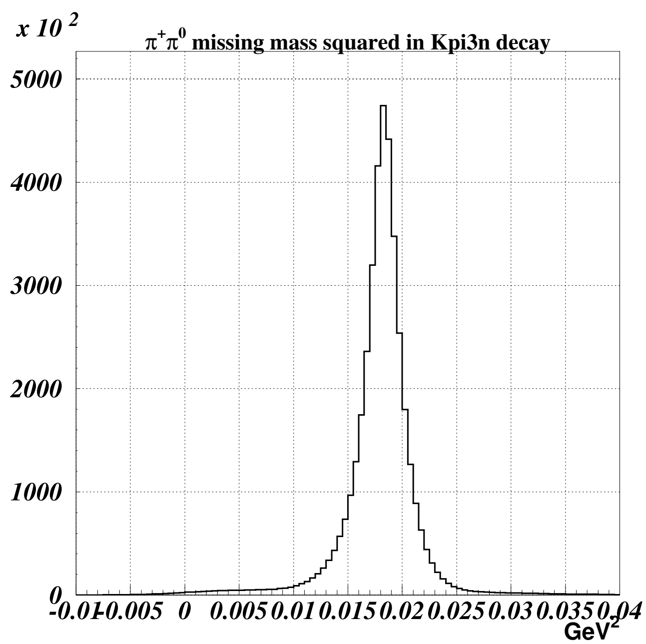

Figure 6.2: $\pi^+\pi^0$ missing mass squared in $K^{\pm} \rightarrow \pi^{\pm}\pi^{0}\pi^{0}$ decay (MC).

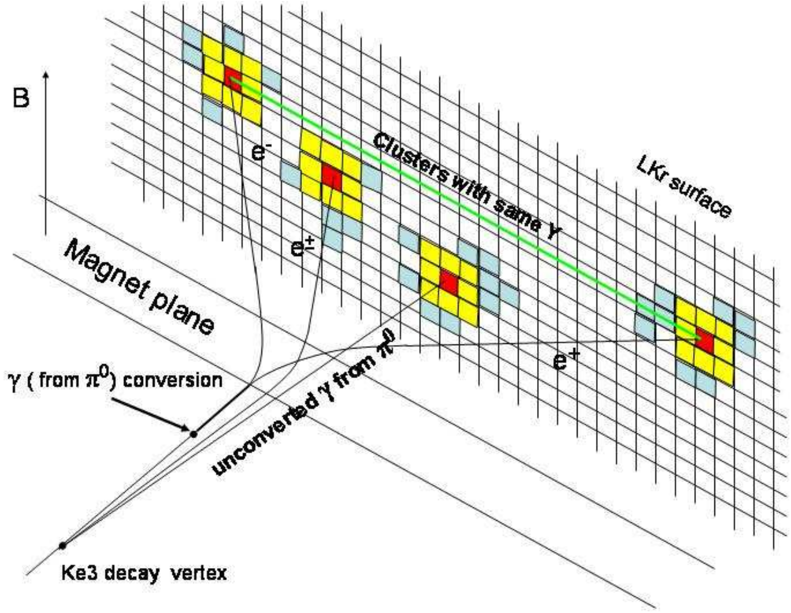

Figure 6.3: Sketch of the BG generated by Ke3 channel through a photon conversion after DCH1.

6.3 Ke3γ BG identification

In this section the identification of the contamination produced by the BG channels exposed in the previous section to the Ke3γ sample will be described. The use of MC simulated events is mandatory to optimize the cuts and improve their rejection power. The kinematical isolation of the signal will be performed using the tools described in the last section.

The use of the E/p cut is very powerful in rejecting non-leptonic channels, i.e. channels where the track having the same sign of the decaying kaon is a pion. The cut applied on data is, as seen in Chapt. 4, $0.95 < \mathrm{E/p} < 1.05$. However the effect of this cut on BG reduction cannot be estimated in a proper way in the MC simulation because of the uncertainties in reproducing hadronic showers inside the LKR calorimeter.

The problem has been overcome by selecting a clean sample of charged pions in the $K^{\pm} \rightarrow \pi^{\pm}\pi^{0}\pi^{0}$ decay and measuring the pion E/p spectrum directly on data. The result is shown in fig. 6.5. A study of the cut efficiency in momentum bins was also performed (fig. 6.6) thanks to the considerable statistics collected (~ 18 million events), giving as a result a slight dependence of the rejection factor with respect to the momentum,as shown in fig. 6.6. Anyway a constant rejection factor was used:

$$R_{E/p} = 1 - A_{E/p} \qquad A_{E/p} = (4.551 \pm 0.016) \cdot 10^{-3}$$

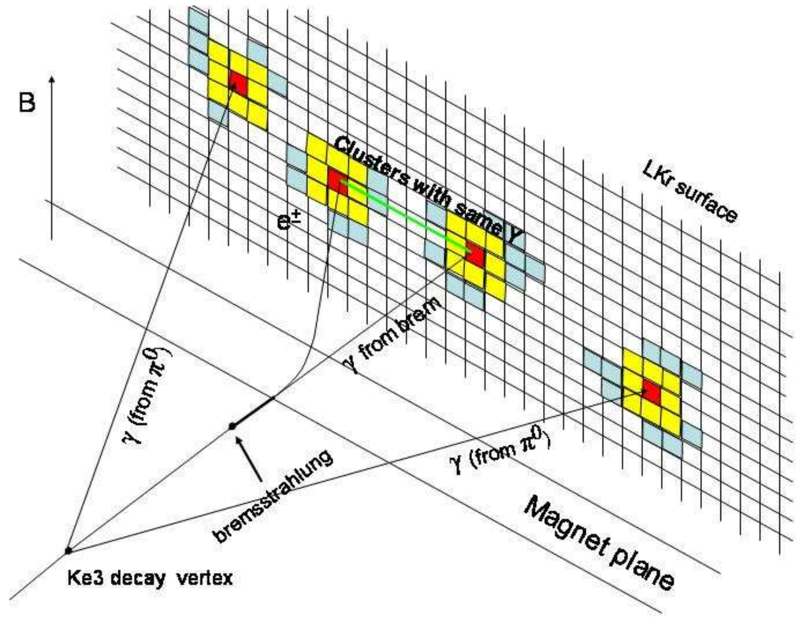

Figure 6.4: Sketch of the BG generated by Ke3 channel through an electron bremsstrahlung.

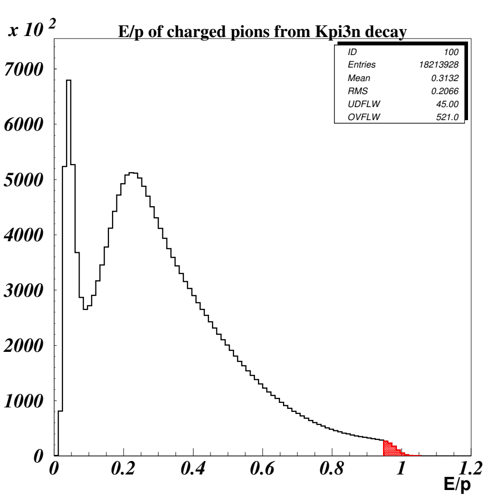

Figure 6.5: E/p ratio for charged pions selected in $K^{\pm} \rightarrow \pi^{\pm}\pi^{0}\pi^{0}$ decay. The E/p area accepted by the analysis cut is the red one.

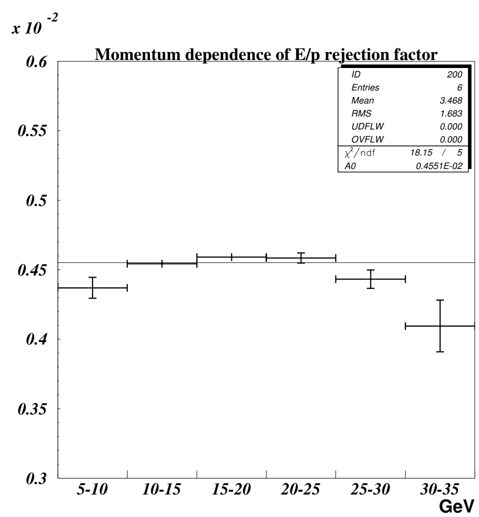

Figure 6.6: The fraction of accepted events $A_{E/p}$ for pions as a function of track momentum.

$A_{E/p}$ being the fraction of accepted events.

Other important rejection cuts are represented by the variables $MM^2_{e-\pi^0}$ and

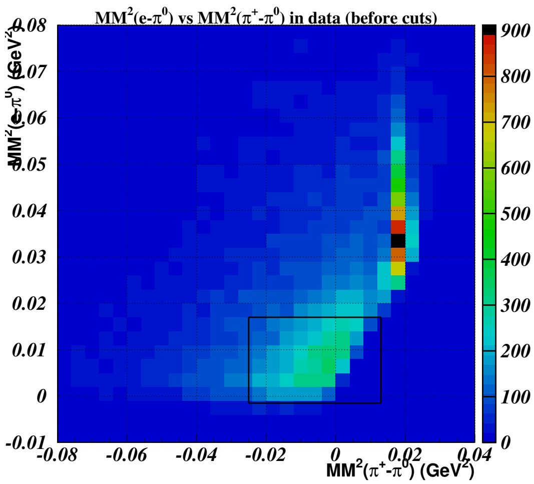

Figure 6.7: $M^2_{e-\pi^0}$ vs $M^2_{\pi^\pm-\pi^0}$ for Ke3γ data. The box defines the cuts applied.

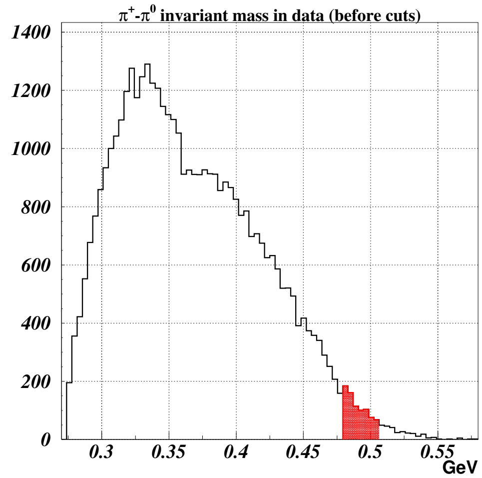

Figure 6.8: Cut on the $\pi^\pm\pi^0$ invariant mass. The colored area is excluded by the cut.

$MM^2_{\pi^\pm-\pi^0}$, which are respectively the missing mass squared of $e^\pm$-π^0 and of $\pi^\pm$-π^0 pairs (in the latter the charged track is given the mass of the charged π) and the $\pi^\pm\pi^0$ invariant mass. The nominal cuts for these variables are:

- -0.0015 GeV^2/c^4 $< MM^2_{e-\pi^0} <$ 0.017 GeV^2/c^2;
- -0.025 GeV^2/c^4 $< MM^2_{\pi^\pm-\pi^0} <$ 0.013 GeV^2/c^4;
- $M_{\pi^\pm\pi^0} <$ 0.48 GeV/c^2 or $M_{\pi^\pm\pi^0} >$ 0.505 GeV/c^2.

The data distribution in the bidimensional plane $M^2_{e-\pi^0}$-$M^2_{\pi^\pm-\pi^0}$, together with the cut applied, is shown in fig. 6.7, while in fig. 6.8 the $M_{\pi^\pm\pi^0}$ cut in the Ke3γ distribution for this variable is shown. As it can be seen in fig. 6.9 and 6.10, these cuts are effective only on some BG's: for example the cut in $M^2_{\pi^\pm-\pi^0}$ eliminates much of the Kpi3n BG, as this BG peaks around M$^2_{\pi^+} \simeq 0.019$ GeV^2/c^4.

It was mentioned that most part of the BG from Ke3 comes from photon conversion after DCH1, with the outgoing tracks which are not reconstructed since the DCH1 hit is missing, or by electron bremsstrahlung, with the additional photon reproducing the fourth cluster needed. For what concerns the conversion, after the splitting by the magnetic field, the electron-positron pair is seen as a photon pair; a π^0 can be reconstructed from one of these leptons and the unconverted photon, while the remaining lepton is seen as the radiative photon. In the electron bremsstrahlung the additional photon can either be reconstructed as the radiative photon from Ke3γ, or it can be considered as coming from the π^0, with one of the photons produced by

π^0 seen as radiative photon. None of the cuts mentioned before is very effective in reducing this kind of BG; however a two-dimensional cut based on the kinematics of the conversion can be devised in each of the two cases.

Regarding the first case, the two clusters coming from a photon conversion after DCH1 and before the magnet are such that:

- Their Y-coordinates are the same (within the resolution), since the magnetic field, being oriented in the Y-direction, bends charged particles in the X plane;
- The invariant squared mass of the two clusters computed using the formula exposed in Chapt. 4 for the neutral vertex (assuming the distance to be equal to the magnet position D_{mag} with respect to the LKr):

$$M_A^2 = \frac{E_1 E_2[(x_1 - x_2)^2 + (y_1 - y_2)^2]}{D_{mag}^2} \tag{6.3}$$

must equal the change from 0 (i.e. the invariant mass of the photon) of the

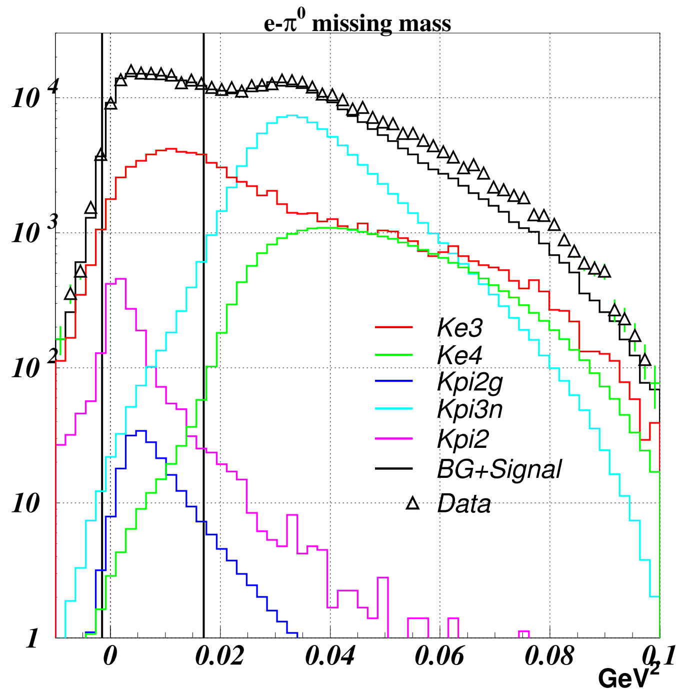

Figure 6.9: Distribution of signal and of analyzed BGs in the $MM^2_{e-\pi^0}$ variable. The black vertical lines mark the cut applied.

invariant squared mass induced by the P_t kick of the magnet, which is:

$$M_B^2 = P_t^2 (2 + \frac{E_1}{E_2} + \frac{E_2}{E_1}) \tag{6.4}$$

If now one defines the variable:

$$R_{conv} = M_A^2 / M_B^2$$

for this kind of events $R_{conv} \sim 1$.

In fig. 6.11 the distribution of the variable R_{conv} in data and MC is shown, while in fig. 6.12 the correlation between this variable and the Y-coordinate difference between clusters can be seen.

Events were rejected if the Y-coordinate difference of the cluster associated with the radiative photon and that of any of the two clusters associated with the π^0 was within ± 4 cm and, simultaneously, the R_{conv} variable built using these two clusters was within $\pm 3\ \sigma$ from the computed R_{conv} central value. The latter and the value of σ was estimated through a gaussian fit of the R_{conv} distribution in Ke3 MC events.

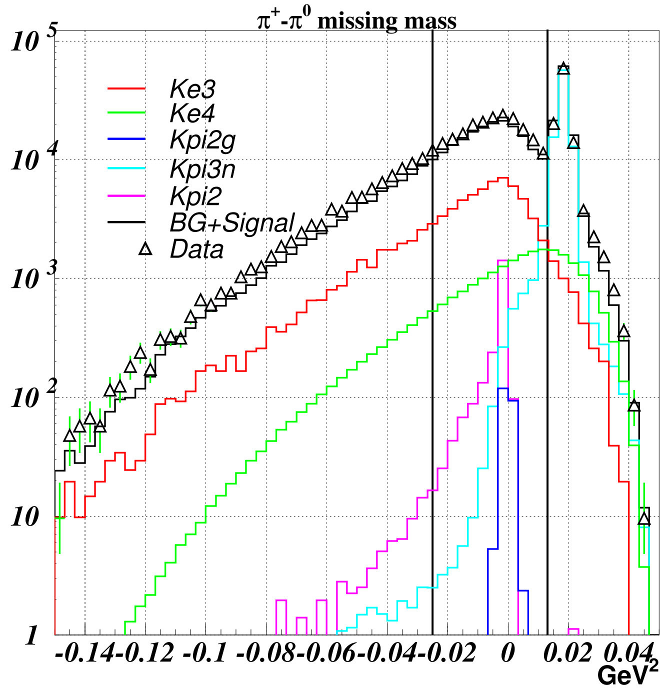

Figure 6.10: Distribution of signal and of analyzed BGs in the $MM^2_{\pi^\pm - \pi^0}$ variable. The black lines mark the cut applied.

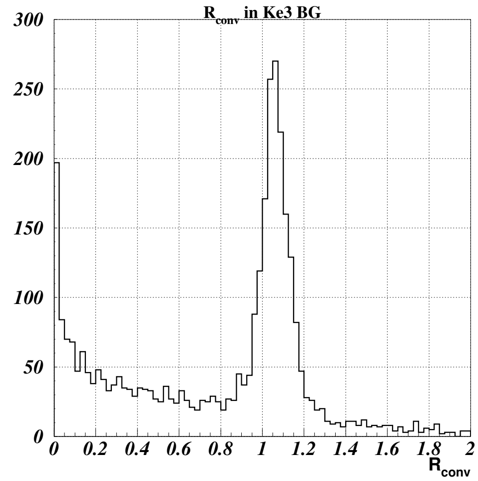

Figure 6.11: Distribution of R_{conv} variable for MC Ke3 data (left) and real data (right) selected with the Ke3γ analysis. The R_{conv} variable computed using the radiative photon cluster and each of the photons forming the π^0 is plotted. The BG detected in MC events is also seen in real data; the signature of conversions is more evident in MC because in real data events from the signal itself and from other BG channels are present.

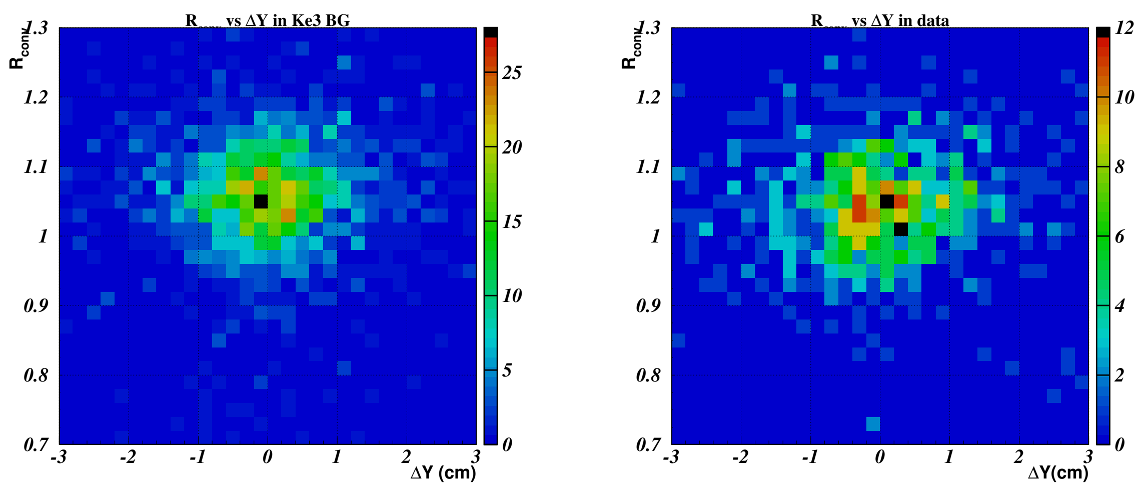

Figure 6.12: Distribution of the R_{conv} variable vs ΔY of the clusters for MC Ke3 data (left) and real data (right) selected with the Ke3γ analysis. The R_{conv} variable computed using the radiative photon cluster and each of the photons forming the π^0 is plotted. The BG detected in MC events is also seen in real data.

For the electron bremsstrahlung, it was mentioned that the produced cluster can either be reconstructed as coming from the π^0 or from the radiative photon. It can be seen from the study of MC Ke3 events that only in the first case there's a relevant

BG production: this is because the cut (15 cm) applied on the distance between photon and electron clusters on LKr surface cuts away the BG events belonging to the second case.

The conditions which must be simultaneously fulfilled are the same as in the case of conversions, with the clusters now belonging to the charged lepton and to one of the π^0 clusters. The change from the electron mass (which can be neglected and set to 0) of the particles' invariant squared mass induced by the P_t kick of the magnet is:

$$M_C^2 = \frac{P_t^2 E_{brem}}{E_{electron}}$$

where E_{brem} is the energy of the bremsstrahlung photon and $E_{electron}$ is the deposited by the selected electron in the LKr. The variable defined as:

$$R_{brem} = M_A^2 / M_C^2$$

is then peaked to $\simeq 1$.

The distribution of the R_{brem} variable in data and MC events is shown in fig. 6.13, while in fig. 6.14 the correlation between the R_{brem} and the ΔY variable is pictured, for both data and MC Ke3 events.

As in the case of photon conversion, it was chosen to reject the event if ΔY (the difference between the Y coordinates of the two clusters) is within $\pm$ 4 cm and, at the same time, R_{brem} is within $\pm\, 3\sigma$ of the R_{brem} central value. The latter and the value of σ were estimated through a gaussian fit of the MC Ke3 events.

The final cut performed to reject the BG is that on the missing squared mass. In fig. 6.15 it is shown the residual BG coming from the various channels before the cut, which is set to be $|M_\nu| < 0.003$ GeV^2/c^4.

In tab. 6.1 the acceptances for the analyzed BG channels after the cut applied are shown.

Channel	BR	Acceptance	
		positive	negative
Kpi2	$(20.92\pm0.12)\cdot10^{-2}$	$(8.002\pm0.028)\cdot10^{-8}$	$(7.395\pm0.026)\cdot10^{-8}$
Kpi3n	$(1.757\pm0.024)\cdot10^{-2}$	$(2.7748\pm0.0098)\cdot10^{-6}$	$(2.7264\pm0.0096)\cdot10^{-6}$
Kpi2g	$(2.75\pm0.15)\cdot10^{-4}$	$(4.479\pm0.016)\cdot10^{-5}$	$(4.444\pm0.016)\cdot10^{-5}$
Ke3	$(4.98\pm0.07)\cdot10^{-2}$	$(9.58\pm1.15)\cdot10^{-7}$	$(9.17\pm1.60)\cdot10^{-7}$
Ke4	$(2.2\pm0.4)\cdot10^{-5}$	$(2.061\pm0.029)\cdot10^{-4}$	$(2.104\pm0.042)\cdot10^{-4}$

Table 6.1: BG channels for Ke3γ and their acceptance after selection cuts.

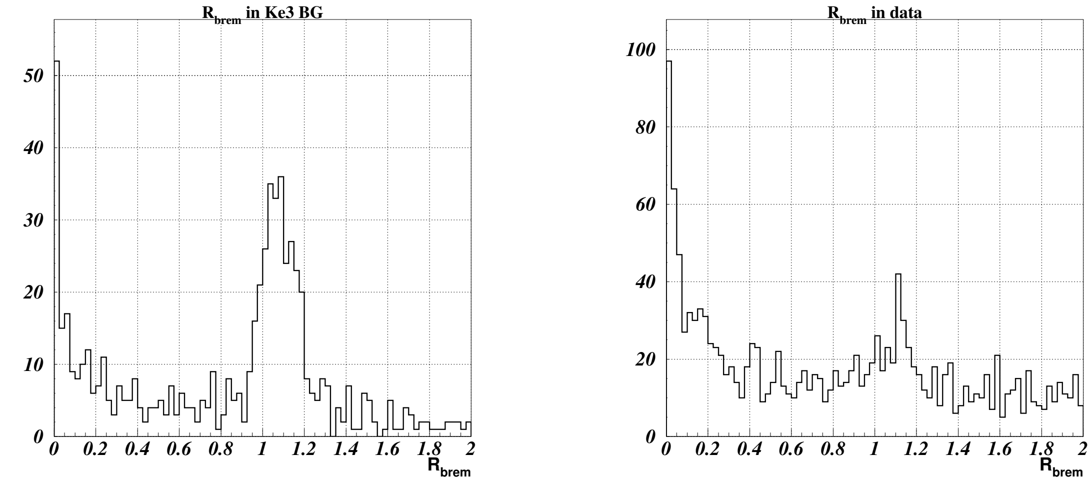

Figure 6.13: Distribution of R_{brem} variable for MC Ke3 data (left) and real data (right) selected with the Ke3γ analysis. The two plots show the R_{brem} variable computed using the electron cluster and each of the photons forming the π^0. The BG detected in MC events is also seen in real data; the signature of bremsstrahlung events is more evident in MC because in real data events from the signal itself and from other BG channels are present.

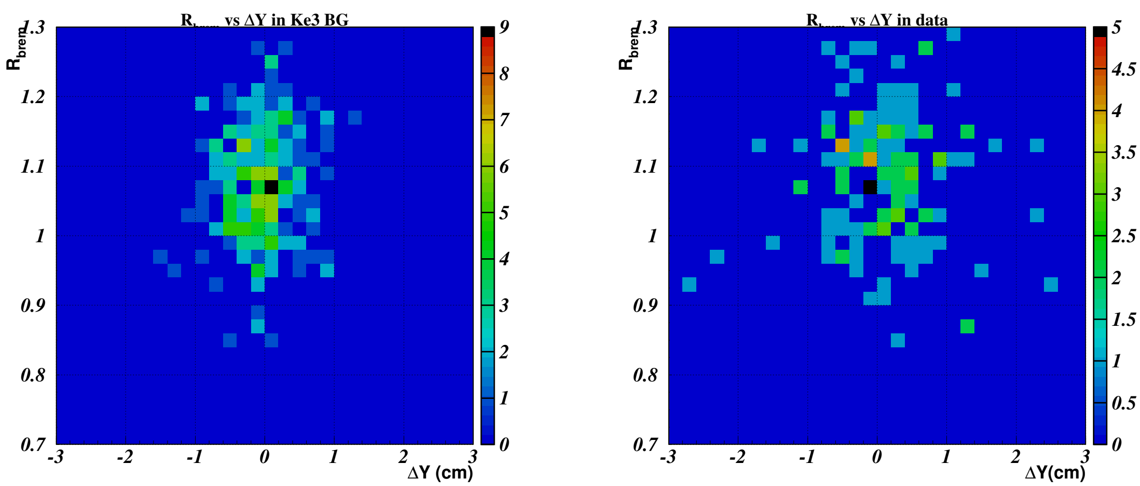

Figure 6.14: Distribution of the R_{brem} variable vs ΔY of the clusters for MC Ke3 data (left) and real data (right) selected with the Ke3γ analysis. The two plots show the R_{brem} variable computed using the electron cluster and each of the photons forming the π^0. The BG detected in MC events is also seen in real data.

6.4 Background channels to the Ke3 decay

Since the Ke3 has a much larger BR with respect to the Ke3γ, not all the BG's

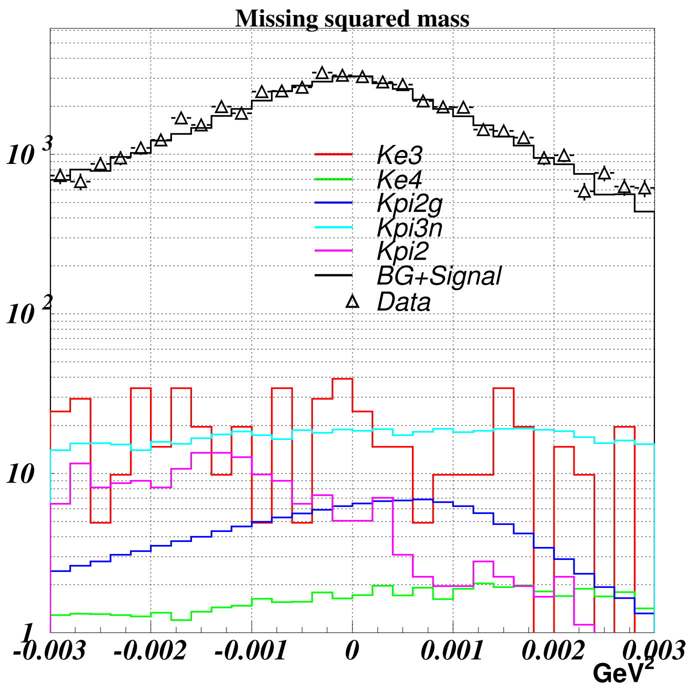

Figure 6.15: Missing squared mass of signal and BG's for Ke3γ signal. The BG contribution is reweighted according to the relative BR.

considered for the Ke3γ play a relevant role. The only channels which can give a sizable contribution are Kpi2 (BR $\simeq$ 21%) and neutral Kpi3n (BR $\simeq$ 1.7%), as their BR's are of the same order of magnitude than the Ke3 BR.

6.4.1 $K^{\pm} \to \pi^{\pm}\pi^{0}$ decay

The only difference between Kpi2 and Ke3 final state is that the charged track is a pion rather than an electron. BG contribution can be highly reduced with the requirement on E/p. Neverthless a residual contribution is left, that can be eliminated by cutting on the $\pi^{\pm} - \pi^{0}$ invariant mass, corresponding to the charged kaon mass. The nominal cut chosen is $M(\pi^{\pm}\pi^{0}) < 0.48$ GeV/c^2 or $M(\pi^{\pm}\pi^{0}) >$ 0.505 GeV/c^2, as shown in fig. 6.16.

6.4.2 $K^{\pm} \to \pi^{\pm}\pi^{0}\pi^{0}$ decay

The Kpi3n final state can fake Ke3 if the two photons from one of the π^0 are lost, e.g. because they are outside the geometrical acceptance. The E/p cut is such

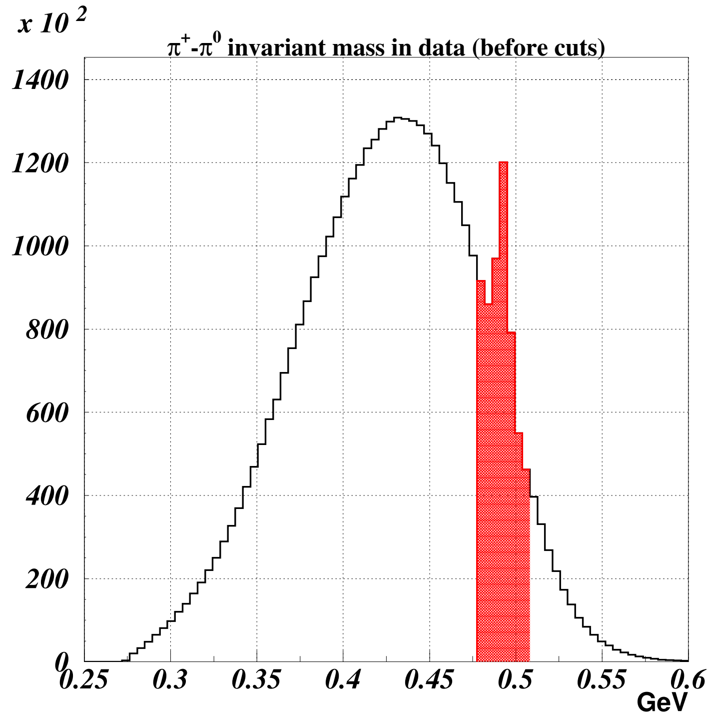

Figure 6.16: Cut on the $\pi^{\pm}\pi^{0}$ invariant mass for Ke3 events. The colored area is excluded by the cut.

that the relative BG is reduced to a negligible level without imposing any additional cut.

In the table 6.2 the acceptances for the different BG channels after the applied cuts are shown, while in fig. 6.17 the residual BG is shown.

Channel	BR	Acceptance	
		positive	negative
Kpi2	$(20.92\pm0.12)\cdot10^{-2}$	$(1.244\pm0.022)\cdot10^{-4}$	$(1.198\pm0.031)\cdot10^{-4}$
Kpi3n	$(1.757\pm0.024)\cdot10^{-2}$	$(6.573\pm0.052)\cdot10^{-4}$	$(6.498\pm0.074)\cdot10^{-4}$

Table 6.2: BG channels for Ke3 and their acceptance after selection cuts.

It is clear that this method of estimating the BG heavily relies on MC. In case the MC tuning on data is not perfect, systematic errors associated to the BG estimation could arise; this aspect will be discussed in Chapt. 8.

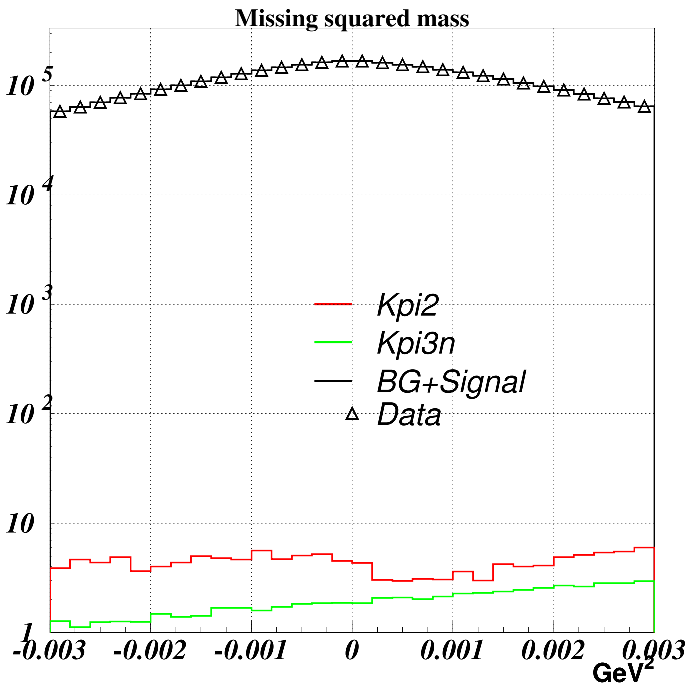

Figure 6.17: Missing squared mass of signal and BGs for Ke3 signal. The BG contribution is reweighted according to the relative BR.

6.5 BG subtraction

Once the MC events were produced and passed through the Ke3γ or Ke3 analysis, the BG events passing the selection can be used to give an estimation of how many events of those selected on data come from a BG channel.

Let N_{tot} be the total number of events obtained in real data with an analysis which aims at selecting a given decay. This number will be in general the sum of the events N_{sig} belonging to this decay and of events N^i_{BG} coming from the different BGs:

$$N_{tot} = N_{sig} + \sum_i N^i_{BG} \tag{6.5}$$

Using MC events it is possible to relate the number of events from the i-th BG channel to the signal events:

$$N^i_{BG} = \alpha_i N_{sig} \qquad \text{where:} \qquad \alpha_i = \frac{Acc^i_{BG} \cdot BR^i_{BG}}{Acc_{sig} \cdot BR_{sig}} \tag{6.6}$$

where the computed acceptances include both geometric and selection efficiencies.

Using 6.6 in 6.5, the total number of signal events can be expressed in terms of the number of events selected and the BG contribution:

$$N_{sig} = \frac{N_{tot}}{1 + \sum_i \alpha_i} \tag{6.7}$$

In tab. 6.3 the number of expected BG events on data for every channel using this method is exposed, together with the number of selected events before and after BG subtraction. The quoted errors include the statistical error and the error due to the precision on the BG channels' BR's, used in 6.6.

BG channel	Expected BG events	
	positive	negative
Ke3	34.6±5.9	18.7±4.3
Ke4	3.3±1.8	1.90±1.4
Kpi3n	35.4±5.9	19.7±4.4
Kpi2	12.1±3.5	6.4±2.5
Kpi2g	8.9±3.0	5.0±2.2
Total	94.3±9.7	51.6±7.2
Ke3γ Selected events	3248±57	1853±43
Events after BG subtraction	3154±58	1801±44

Table 6.3: Estimation of Ke3γ signal events after subtraction of BG events estimated through MC.

The number of BG events expected in the events selected for the normalization channel is shown in table 6.4. After the selection cuts applied, the Ke3 is almost BG free, with residual BG below the per mille level.

BG channel	Expected BG events	
	positive	negative
Kpi3n	33.6±5.8	18.7±4.3
Kpi2	75.8±8.7	41.1±6.4
Total	109.4±10.5	59.8±7.7
Ke3 Selected events	$(21894\pm15)\cdot10^2$	$(12100\pm11)\cdot10^2$
Events after BG subtraction	$(21893\pm15)\cdot10^2$	$(12100\pm11)\cdot10^2$

Table 6.4: Estimation of Ke3 signal events after subtraction of BG events estimated through MC.

6.6 Conclusions

The BG isolation cuts described in this chapter allowed to reduce the residual BG on Ke3γ to the level of $\sim$3%; the main decay channels contributing to this number being the Ke3 and the Kpi3n. For what concerns the normalization channel, the residual BG after the cuts is totally negligible.

Chapter 7

Trigger issues

In this chapter the trigger used to select the Ke3γ and Ke3 samples described in the former chapters will be discussed and the way in which trigger efficiency has been taken into consideration for both signal and normalization channels will be described.

7.1 The Ke3γ and Ke3 trigger chain

The trigger used in the usual 2003 and 2004 NA48/2 data-taking implies, as it was discussed in Chapt. 2, the presence of a level 1 and a level 2, the latter being commonly referred to as Massbox. The use of these data-taking periods would allow a much higher available statistics but, as mentioned in par. 3.2, some drawbacks related to possible trigger bias would arise.

The present analysis has been performed on the 2004 special run. For these events, collected between August 12th and August 14th (12 runs), the trigger used is Q1$\times$E$_{LKr}$ > 10 GeV. One of the advantages of this trigger configuration is that it prevents possible biases on collected data, e.g. coming from L2 trigger cuts on track fake mass (see Chapt. 2). The trigger used in the special run only requires at least one hit in a hodoscope quadrant (Q1) and a minimum amount of energy in the LKr (E$_{LKr}$ > 10 GeV). This configuration has some important advantages in the present analysis, as one can use the same trigger configuration for signal and normalization channel. In case of normal data-taking, on the other hand, the triggers have different efficiencies: for example the NT-peak, which is based on the number of peaks in the X and Y views of the LKr, yields different efficiencies for Ke3γ and Ke3 events because of the different number of LKr clusters, and hence of peaks.

The most serious drawback of this configuration is represented by the statistics accumulated: even if the 2004 SR trigger configuration was specifically designed to collect this kind of events, the number of events that can be selected is of the order of few thousands, compared to some 10^5 which can be selected from the 2003 data only.

7.2 Trigger efficiency

In order to compute the efficiency associated with each element of the trigger chain, some control triggers were used. A control trigger must not be correlated to the trigger whose efficiency it must measure: for this reason the detectors originating the signal must be different from those producing the trigger. Some downscaled triggers are acquired together with the main triggers, with the purpose to be used as control triggers.

Once a control trigger T_c has been chosen to control the main trigger T_m, it must be checked, among the events triggered by T_c, how many of them fired the trigger T_m as well. These information are recorded in a digital register called Pattern Unit (PU), where for each of the 25 ns time slices of the event it is reported whether or not the trigger T_m has fired. To account for possible time offsets, it is assumed that the trigger T_m has fired if its signal is present either in the time slice of the control trigger or in the two time slices preceding and following the control trigger time slice. The PU inefficiency has been measured in previous analyses and found to be negligible. The efficiency of trigger T_m is then:

$$Eff_{T_m} = \frac{N_{evts}(T_c(TW) \times T_m(PU))}{N_{evts}(T_c(TW))} \tag{7.1}$$

where T_c(TW) (TW stands for "Trigger Word", already defined in Chapt. 2) and T_m(PU) are respectively the control trigger and the trigger whose efficiency has to be estimated. In the BR computation only the total number of events is important, this justifying the use of integrated trigger efficiency (the ratio defined in 7.1). However, if one has to measure quantities (e.g. form factors) for which the shape of the distributions is important, trigger efficiency should be considered on a bin-by-bin basis as it could affect the shape of the distribution and hence the result.

Another common problem for the control triggers is that they are usually heavily downscaled with respect to main triggers: this implies that, especially for rare channels, the statistics of the sample used to compute trigger efficiency is very small. A possible solution in these cases is to increase the sample using decays from other channels which have a similar topology.

In the following the efficiency computation of the two triggers Q1 and $\mathrm{E}_{LKr} >$ 10 GeV, used to select events in the present analysis, will be presented.

7.2.1 Q1 efficiency

The Q1 efficiency was estimated on the Ke3γ and Ke3 sample, using T0N, i.e.

the control trigger with the highest statistics. The efficiency was also recomputed using $E_{LKr} > 10$ GeV control trigger as a cross-check. The computed efficiencies are:

$$EFF_{Q1}^{Ke3\gamma}(T0N) = (99.35 \pm 0.46)\% \qquad EFF_{Q1}^{Ke3\gamma}(E_{LKr} > 10GeV) = (96.8 \pm 1.8)\%$$

$$EFF_{Q1}^{Ke3}(T0N) = (99.753 {\pm} 0.012)\% \qquad EFF_{Q1}^{Ke3}(E_{LKr} > 10GeV) = (99.716 {\pm} 0.022)\%$$

7.2.2 $E_{LKr} > 10$ GeV efficiency

The $E_{LKr} > 10$ GeV efficiency was measured taking Q1 as control trigger. The only difference between Ke3γ and Ke3 events in relation to the $E_{LKr} > 10$ GeV trigger lies in the different energy distribution of the events, because of the different topology and number of particles in the final state of the two decays. One expects that in a region close to 10 GeV of total energy deposited in the LKr the trigger efficiency will have a slope because of resolution effects. If both Ke3γ and Ke3 total energy distributions are far away from the trigger cut region, it is reasonable to expect that the $E_{LKr} > 10$ GeV trigger efficiency of the two channels will be compatible.

The energy distribution of selected Ke3γ and Ke3 events is shown in fig. 7.1 and 7.2 respectively; the $E_{LKr} > 10$ GeV trigger efficiency distribution in bin of total energy, shown in fig. 7.3 for the Ke3 channel, is flat over the whole energy spectrum. The trigger efficiency for Ke3γ and Ke3 events is:

$$EFF_{E_{LKr}>10GeV}^{Ke3\gamma} = (100.000 - 0.69)\%$$

$$EFF_{E_{LKr}>10GeV}^{Ke3} = (99.888 \pm 0.013)\%$$

where the error on $\mathrm{EFF}_{E_{LKr}>10GeV}^{Ke3\gamma}$ is determined using a lower limit for binomial distribution at 10$ C.L. [18] (all events triggered by Q1 resulted efficient).

The total trigger efficiency, which directly enters the BR measurement (see Chapt. 3) is the product of the two computed trigger efficiencies for each of the two channels:

$$EFF^{Ke3\gamma} = EFF_{Q1}^{Ke3\gamma} \times EFF_{E_{LKr}>10GeV}^{Ke3\gamma} = (99.35 \pm 0.83)\%$$

$$EFF^{Ke3} = EFF_{Q1}^{Ke3} \times EFF_{E_{LKr}>10GeV}^{Ke3} = (99.641 \pm 0.018)\%$$

Regarding the A_ξ measurement, in principle one should apply a differential trigger efficiency over the whole ξ spectrum. However this would imply a very sizable

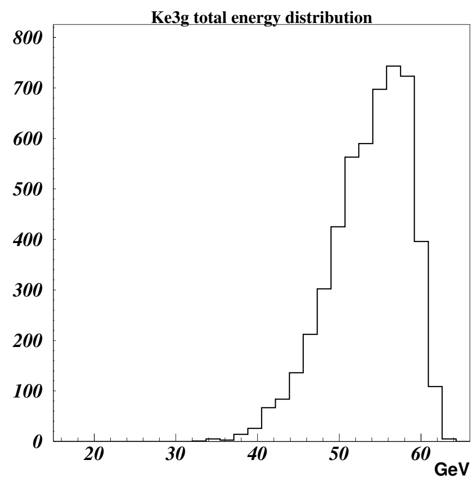

Figure 7.1: Total LKr energy ($e^{\pm}+\pi^0+\gamma$) of selected Ke3γ events.

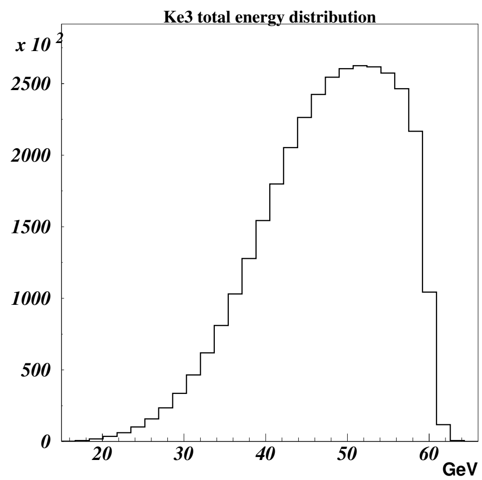

Figure 7.2: Total LKr energy ($e^{\pm}+\pi^0$) of selected Ke3 events.

associated error, since the number of events per bin would be very reduced. However it can be shown using MC data that the trigger efficiency cancels in the ratio. In order to obtain such a cancellation the efficiency ϵ_{trig} in the formula 3.3 should be equal for ξ-positive and ξ-negative events. As stated before, the trigger used is Q1 $\times$ $E_{tot} > 10$ GeV.

Since a fixed value of ξ is obtained through different combinations of orientations and momentum of the three measured particles, it is unlikely that an inefficiency of the triggers used could bias the A_ξ measurement; neverthless a check using MC-generated events was performed to obtain an upper limit of this eventual bias, which was then added as a systematic effect to the final result.

The bias induced on the A_ξ measurement by possible inefficiencies of the $E_{LKr} > 10$ GeV trigger was estimated turning off the LKr columns onto which the total energy is summed: indeed, as stated in Chapt. 2, the energy distribution momenta (the total energy is the order 0 momentum) are computed on 64 strips, 2 cells (4 cm) wide, in both X and Y projections. The 32 Y-columns belonging to the right half of the LKr were alternatively turned off and the asymmetry was recomputed excluding those events for which at least one cluster fell into the excluded column. The associated systematic was taken as the biggest difference between the nominal value (i.e. that computed without excluding any column) and the A_ξ values computed excluding one column. The values of A_ξ obtained in this way are shown in fig. 7.4 for positive events; the associated error will be included in the estimation of systematic effects, discussed in the next chapter.

For what concerns the Q1 efficiency, one could argue that possible inefficient hodoscope slabs could bias the result. For this reason the MC simulation was used

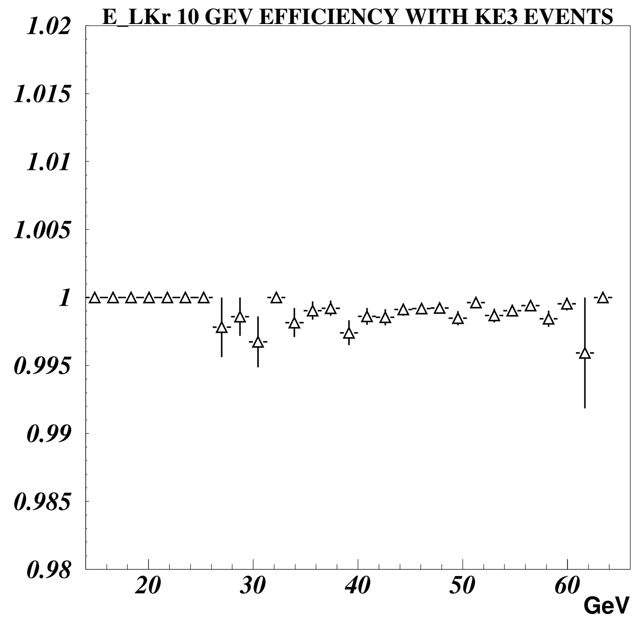

Figure 7.3: Efficiency of the $E_{LKr} > 10$ GeV trigger as a function of total energy for Ke3 events. No evidence of an efficiency decrease in the energy region of Ke3γ and Ke3 events can be seen.

and the A_ξ parameter was recomputed excluding the electron tracks going into the geometric acceptance of each of the 16 hodoscope slabs of the upper right quadrant (quadrant 2). The systematic associated with a possible effect of an inefficient slab was then taken as the biggest difference between the nominal value (i.e. that computed without excluding any slab) and the A_ξ values computed excluding one slab. This error corresponds to consider a 100% inefficiency for the slab under analysis and is therefore an upper limit. The values of A_ξ obtained in this way are shown in fig. 7.5 for positive events; the associated error will be included in the estimation of systematic effects, discussed in the next chapter.

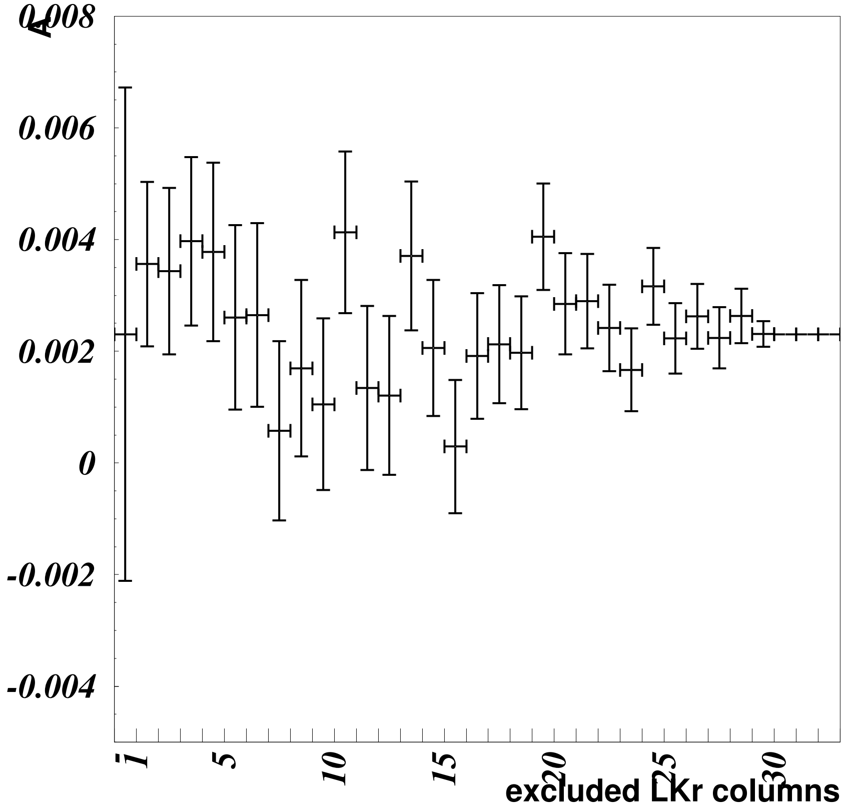

Figure 7.4: A_ξ MC measurement with all columns included (first bin) and excluding each of the 32 Y-columns belonging to the right half of the LKr. Only uncorrelated errors are shown for the measurements with excluded columns.

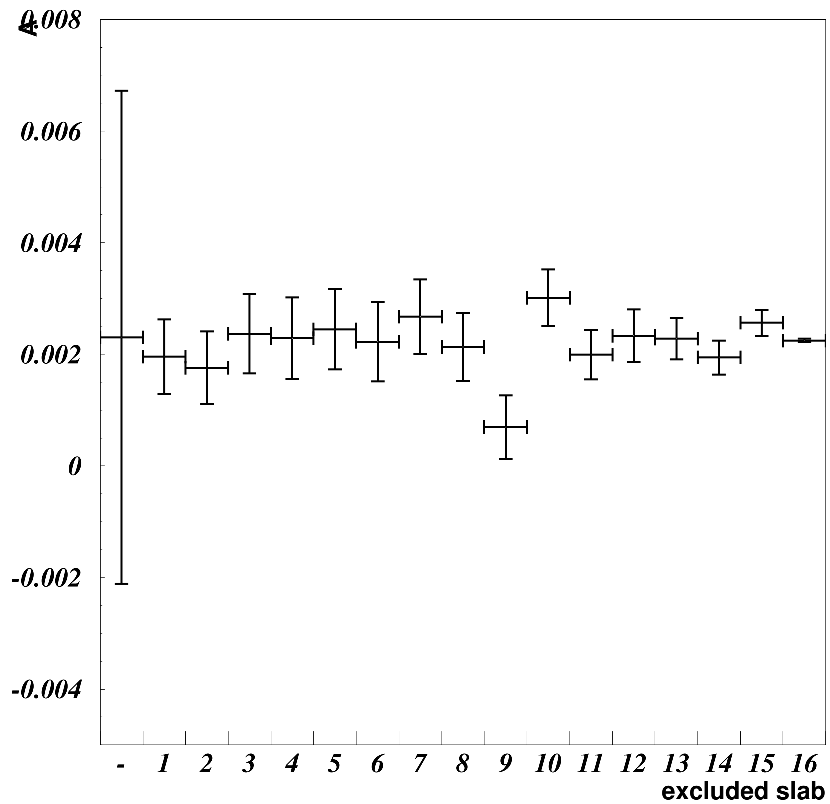

Figure 7.5: A_ξ MC measurement with all slabs included (first bin) and excluding each of the 16 slabs belonging to the second vertical hodoscope quadrant (see fig. 2.13). Only uncorrelated errors are shown for the measurements with excluded slabs.

Chapter 8

Estimation of systematic effects and additional checks

The use of a normalization channel sharing the same trigger chain and whose final state is very similar to that of Ke3γ reduces the presence of systematic effects in the measurement performed. Neverthless some residual systematics are still present; in this chapter this problem will be addressed and a way to compute this kind of error will be presented. Some additional checks, described in the last paragraph, were also performed.

8.1 Systematic errors' computation procedure

The results obtained for Ke3γ BR and A_ξ should not depend on the applied selection cuts; if this happens there is something out of control in the analysis, and this turns into the presence of a systematic uncertainty in the final result. The origin of systematics can be manyfold: they can be originated by some unaccounted instrumental effect, by a wrong tuning of the MC simulation, or by some unaccounted BG.

The computation of systematic effects has been made by varying the cuts applied in both Ke3γ and Ke3 selections and computing the "new" values of the relative BR and of A_ξ. A cut variation has as a consequence a modification of the selection's acceptance, with the result that the statistical error of the measurement is also modified. The cut variation was such to determine a change in the statistics of the analyzed sample between 10% and 20% with respect to the nominal cut. Given a specific cut, it was chosen to add an associated systematic error if the absolute value of the difference between the measurement obtained with the nominal cut and with the varied cut was bigger than the difference of the associated statistical uncertainties squared, the so-called uncorrelated error. In formulae, if happens that:

$$|R(nom) - R(var)| > \sqrt{|\sigma^2_{stat}(nom) - \sigma^2_{stat}(var)|} \tag{8.1}$$

The value taken as systematic error for a given cut is the biggest value of $|R(nom) - R(var)|$ among the values obtained varying the cut, provided condition 8.1 is fulfilled; if not, the variation is within the uncorrelated error and no systematic error is assumed.

The cuts applied to both signal and normalization channels were varied in both selections when estimating the associated systematic error: this allows to reduce "fake" systematics due, for example, to the MC simulation not reproducing well some kinematical variables in both channels. For cuts applied only to the Ke3γ channel (e.g. the distance between electron and photon clusters on LKr) the variation is only in the Ke3γ events, for both data and MC. The BG events were also recalculated and subtracted according to the varied cut.

8.2 Cut variation effects

In tab. 8.1 the varied analysis cuts are reported, together with their variation range. Where possible, the cut was varied in both directions, in such a way to increase and decrease statistics; otherwise, e.g. in the case of the DCH radius, the cut was moved only in one direction.

Cut	Nominal value	Variation range
Track momentum (upper)	35 GeV/c	25/37 GeV
Track momentum (lower)	5 GeV/c	3/11 GeV
Track position at DCH1	12 cm	12/20 cm
e-γ distance on LKr	15 cm	12/18 cm
Charged-neutral vertex distance	400 cm	250/550 cm
Cluster energy (lower)	3 GeV	3/4 GeV
Missing mass	0.003 GeV^2/c^4	0.0021/0.0039 GeV^2/c^4
Charged vertex (upper)	7000 cm	5500/8000 cm
Charged vertex (lower)	-1000 cm	-2500/500 cm
e-π^0 missing mass (upper)	0.017 GeV^2/c^4	0.015/0.019 GeV^2/c^4
e-π^0 missing mass (lower)	-0.0015 GeV^2/c^4	-0.0045/0.0015 GeV^2/c^4

Table 8.1: Varied cuts for systematic checks.

In the following paragraph some of the varied cuts are analyzed in detail. In each table the difference between the values (BR and A_ξ) computed with nominal and varied cuts are reported, together with the uncorrelated error.

8.2.1 Track momentum

The track momentum was varied in its upper and lower limit. The stability results for BR and A_ξ are reported in tab. 8.2 and 8.3, while in fig. 8.1 and 8.2 the corresponding trends are shown.

Lower P_{track} cut			
Cut (GeV/c)	$\lvert\Delta BR\rvert(\cdot 10^{-5})$	$\lvert\Delta A_\xi^+\rvert(\cdot 10^{-2})$	$\lvert\Delta A_\xi^-\rvert(\cdot 10^{-2})$
3	0.49	0.066	0.0089
7	1.8	0.24	0.030
9	2.4	0.33	1.1
11	5.9	0.38	1.4

Table 8.2: Differences of Ke3γ/Ke3 BR, A_ξ^+ and A_ξ^- from nominal values as a function of track momentum lower cut. Only varied cuts are quoted.

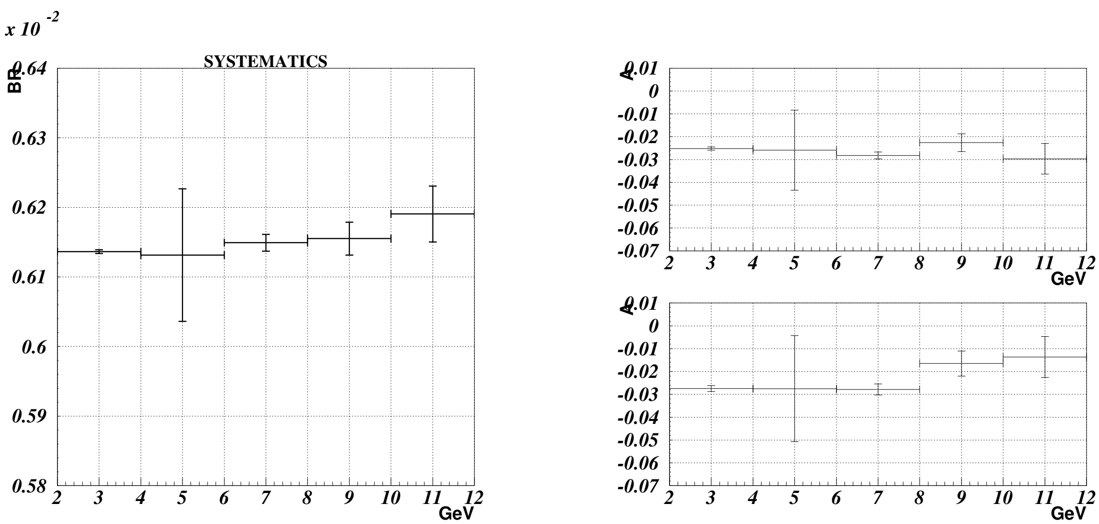

Figure 8.1: BR (left) and A_ξ (right, A_ξ^+ top, A_ξ^- bottom) variation as a function of track momentum lower cut. The nominal value (5 GeV/c) is reported with the statistical error, while only uncorrelated errors are reported for varied cut.

8.2.2 Track position on DCH1

The track position cut on DCH1 was varied from 12 up to 20 cm; no cut under 12 cm was considered because these values correspond to the beam pipe radius. The stability result for BR and A_ξ is reported in tab. 8.4, while in fig. 8.3 the corresponding trend is shown.

Upper P_{track} cut			
Cut (GeV/c)	$\lvert\Delta BR\rvert(\cdot 10^{-5})$	$\lvert\Delta A_\xi^+\rvert(\cdot 10^{-2})$	$\lvert\Delta A_\xi^-\rvert(\cdot 10^{-2})$
25	2.0	0.46	0.74
27	2.8	0.68	0.65
29	1.6	0.11	0.42
31	0.18	0.093	0.20
33	0.20	0.068	0.24
37	0.45	0.025	0.10

Table 8.3: Differences of Ke3γ/Ke3 BR, A_ξ^+ and A_ξ^- from nominal values as a function of track momentum upper cut. Only varied cuts are quoted.

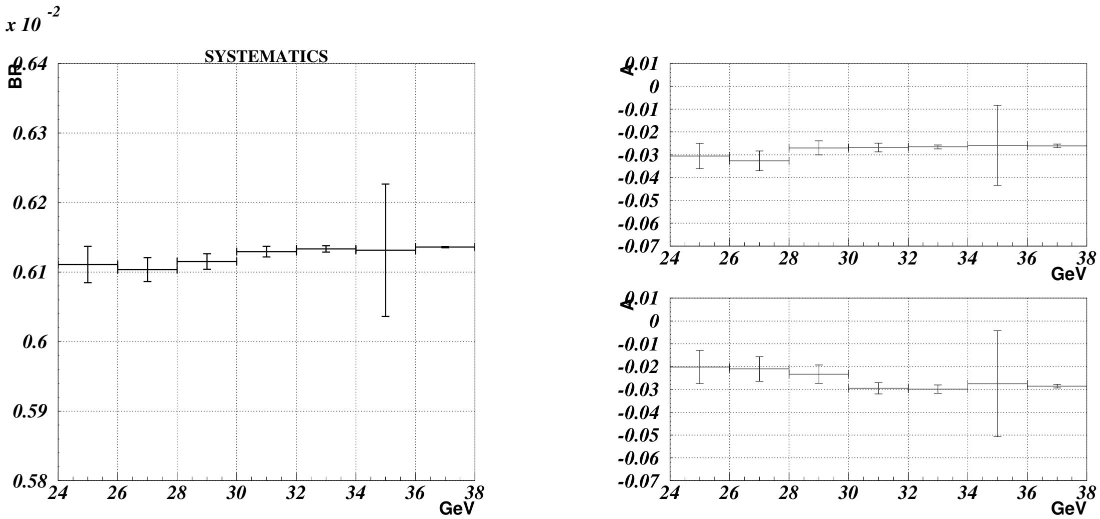

Figure 8.2: BR (left) and A_ξ (right, A_ξ^+ top, A_ξ^- bottom) variation as a function of track momentum upper cut. The nominal value (35 GeV/c) is reported with the statistical error, while only uncorrelated errors are reported for varied cut.

8.2.3 Electron-photon distance on LKr

The cut on distance between electron and photon was varied between 12 and 18 cm. The stability result for BR and A_ξ is reported in tab. 8.5, while in fig. 8.4 the corresponding trend is shown.

8.2.4 Distance between neutral and charged vertex

The cut on distance between neutral and charged vertex was varied between 250 and 550 cm. The stability result for BR and A_ξ is reported in tab. 8.6, while in fig. 8.5 the corresponding trend is shown.

Track position cut on DCH1			
Cut (cm)	$\lvert\Delta\text{BR}\rvert(\cdot 10^{-5})$	$\lvert\Delta A_\xi^+\rvert(\cdot 10^{-2})$	$\lvert\Delta A_\xi^-\rvert(\cdot 10^{-2})$
14	0.31	0.26	0.38
16	1.2	0.14	0.31
18	1.1	0.12	0.14
20	3.2	1.06	0.30

Table 8.4: Differences of Ke3γ/Ke3 BR, A_ξ^+ and A_ξ^- from nominal values as a function of track position cut on DCH1. Only varied cuts are quoted.

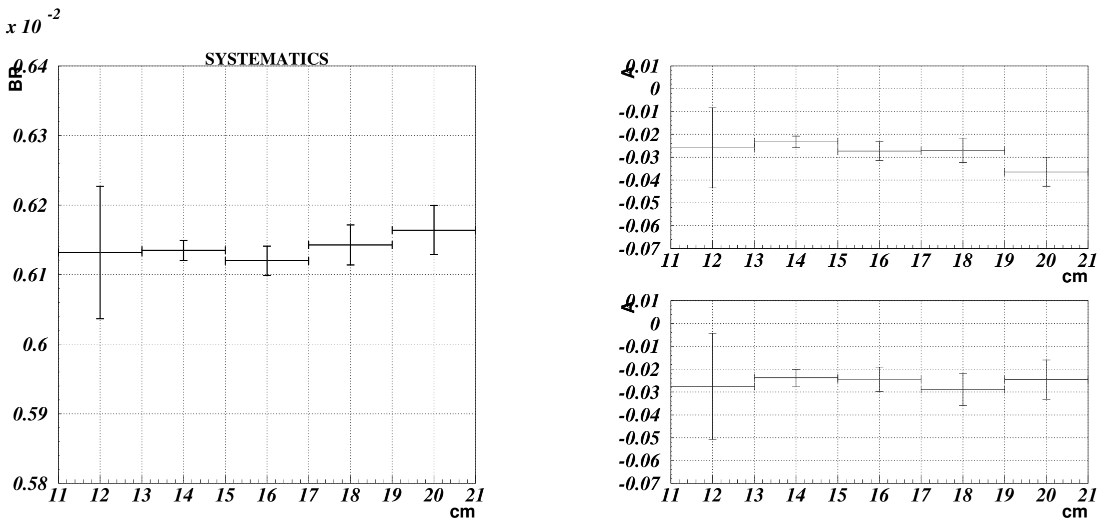

Figure 8.3: BR (left) and A_ξ (right, A_ξ^+ top, A_ξ^- bottom) variation as a function of track position cut on DCH1. The nominal value (12 cm) is reported with the statistical error, while only uncorrelated errors are reported for varied cuts.

8.2.5 Cluster energy

The lower energy limit of selected clusters was varied from 3 up to 4 GeV. The limit was not set under the 3 GeV threshold because of the known LKr non-linearities in that energy range (see Chapt. 5). The stability result for BR and A_ξ is reported in tab. 8.7, while in fig. 8.6 the corresponding trend is shown.

8.2.6 Missing mass cut

The cut on missing mass squared was varied around its nominal value at 0.003 GeV^2/c^4. The stability result for BR and A_ξ is reported in tab. 8.8, while in fig. 8.7 the corresponding trend is shown.

Electron-photon distance cut on LKr			
Cut (cm)	$\lvert\Delta\text{BR}\rvert(\cdot 10^{-5})$	$\lvert\Delta A_\xi^+\rvert(\cdot 10^{-2})$	$\lvert\Delta A_\xi^-\rvert(\cdot 10^{-2})$
12	0.27	0.014	0.33
13	0.24	0.014	0.33
14	0.35	0.22	0.080
16	0.15	0.21	0.20
17	1.4	0.62	0.094
18	3.2	1.2	0.17

Table 8.5: Differences of Ke3γ/Ke3 BR, A_ξ^+ and A_ξ^- from nominal values as a function of electron-photon distance cut on LKr. Only varied cuts are quoted.

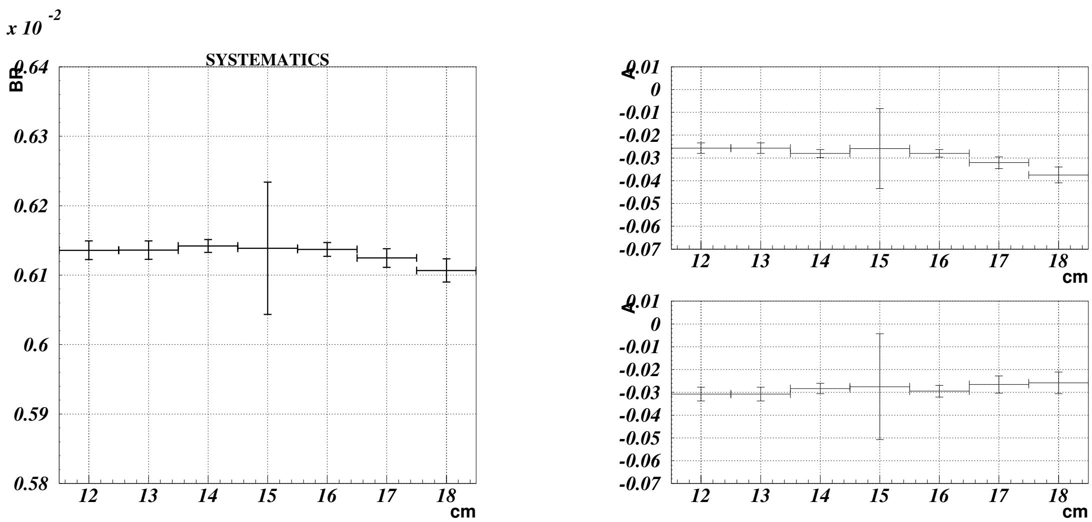

Figure 8.4: BR (left) and A_ξ (right, A_ξ^+ top, A_ξ^- bottom) variation as a function of electron-photon distance cut on LKr. The nominal value (15 cm) is reported with the statistical error, while only uncorrelated errors are reported for varied cuts.

8.2.7 Vertex position cut

The cut on the charged vertex position was varied in both its lower (-1000 cm) and upper (7000 cm) bound. For the latter, no events with a charged vertex greater than 8000 cm were considered, because in these cases the reconstructed vertex is very close or beyond the final collimator. The stability results for BR and A_ξ are reported in tab. 8.9 and 8.10, while in fig. 8.8 and 8.9 the corresponding trends are shown.

Distance between neutral and charged vertex			
Cut (cm)	$\lvert\Delta\mathrm{BR}\rvert(\cdot 10^{-5})$	$\lvert\Delta\mathrm{A}_{\xi}^{+}\rvert(\cdot 10^{-2})$	$\lvert\Delta\mathrm{A}_{\xi}^{-}\rvert(\cdot 10^{-2})$
250	1.7	0.19	0.41
300	1.5	0.068	0.13
350	0.28	0.089	0.14
450	0.52	0.027	0.14
500	1.4	0.045	0.044
550	1.4	0.0026	0.10

Table 8.6: Differences of Ke3γ/Ke3 BR, A_{ξ}^{+} and A_{ξ}^{-} from nominal values as a function of the distance between neutral and charged vertex. Only varied cuts are quoted.

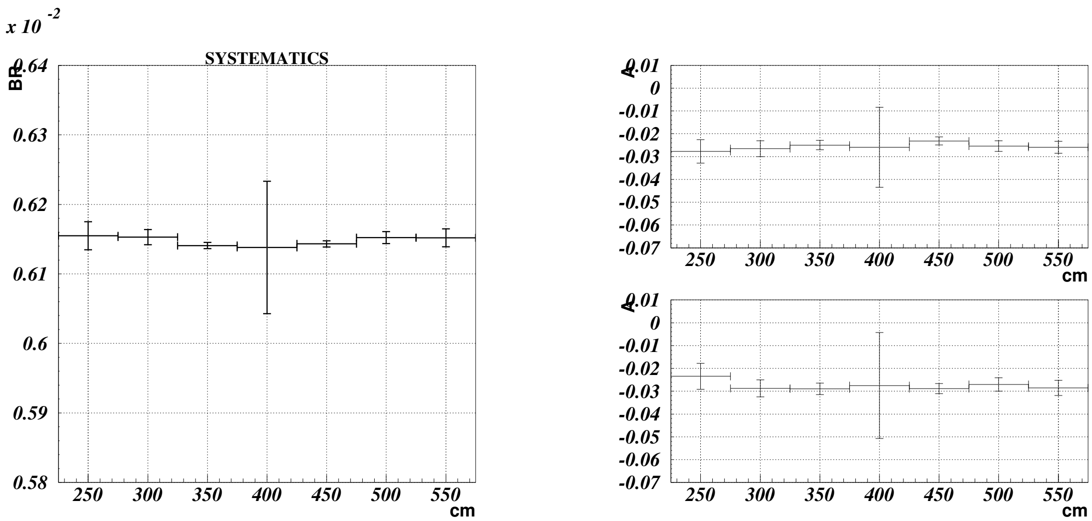

Figure 8.5: BR (left) and A_{ξ} (right, A_{ξ}^{+} top, A_{ξ}^{-} bottom) variation as a function of distance between neutral and charged vertex. The nominal value (400 cm) is reported with the statistical error, while only uncorrelated errors are reported for varied cuts.

8.2.8 Missing e-π^0 mass

The cut on the e-π^0 missing mass (see Cap. 6) was varied in its upper and lower limit. The stability results for BR and A_{ξ} are reported in tab. 8.11 and 8.12, while in fig. 8.10 and 8.11 the corresponding trends are shown.

8.3 Summary of systematic uncertanties

In tab. 8.13 the contributions of all evaluated systematic uncertanties are reported. The contribution on A_{ξ} systematic error due to possible Q1 and $\mathrm{E}_{LKr} >$ 10 GeV bias on A_{ξ} measurements, estimated in Chapt. 7, are reported as well.

LKr cluster energy lower cut			
Cut (GeV)	$\lvert\Delta \mathrm{BR}\rvert(\cdot 10^{-5})$	$\lvert\Delta \mathrm{A}_\xi^+\rvert(\cdot 10^{-2})$	$\lvert\Delta \mathrm{A}_\xi^-\rvert(\cdot 10^{-2})$
3.25	1.2	0.38	0.73
3.5	2.8	0.15	1.3
3.75	5.6	0.012	0.20
4	6.6	0.48	0.58

Table 8.7: Differences of Ke3γ/Ke3 BR, A_ξ^+ and A_ξ^- from nominal values as a function of LKr cluster energy lower cut. Only varied cuts are quoted.

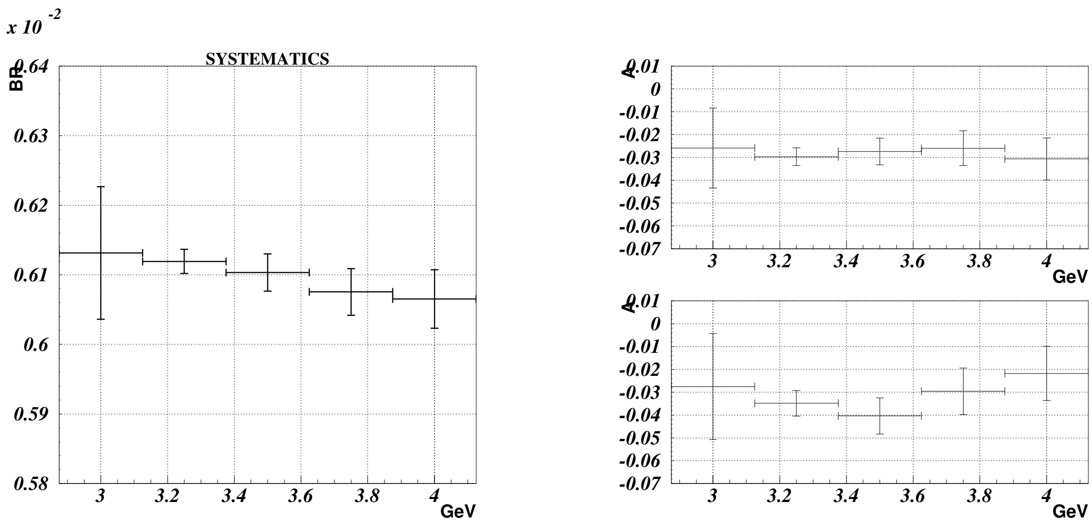

Figure 8.6: BR (left) and A_ξ (right, A_ξ^+ top, A_ξ^- bottom) variation as a function of LKr cluster energy lower cut. The nominal value (3 GeV) is reported with the statistical error, while only uncorrelated errors are reported for varied cut.

The systematics associated to A_ξ^+ and A_ξ^- for each cut were computed averaging the values obtained for the two signs using the method described before. The total systematic error is computed adding in quadrature the computed systematics, as they are assumed to be independent.

8.4 Additional checks

Some additional studies were performed on the BR measurement in order to check for possible biases.

According to SM, the BR for positive and negative Ke3γ events should be the same: therefore the experimental results for positive and negative events should coincide within the errors. The BR of positive and negative events was then measured

Squared M_ν cut			
Cut (GeV^2/c^4)	$\lvert\Delta BR\rvert(\cdot 10^{-5})$	$\lvert\Delta A_\xi^+\rvert(\cdot 10^{-2})$	$\lvert\Delta A_\xi^-\rvert(\cdot 10^{-2})$
0.0021	0.96	1.1	0.0091
0.0024	3.0	1.1	0.57
0.0027	0.31	0.42	0.51
0.0033	0.39	0.29	0.39
0.0036	1.2	0.47	0.47
0.0039	0.64	0.45	0.15

Table 8.8: Differences of Ke3γ/Ke3 BR, A_ξ^+ and A_ξ^- from nominal values as a function of missing mass squared cut. Only varied cuts are quoted.

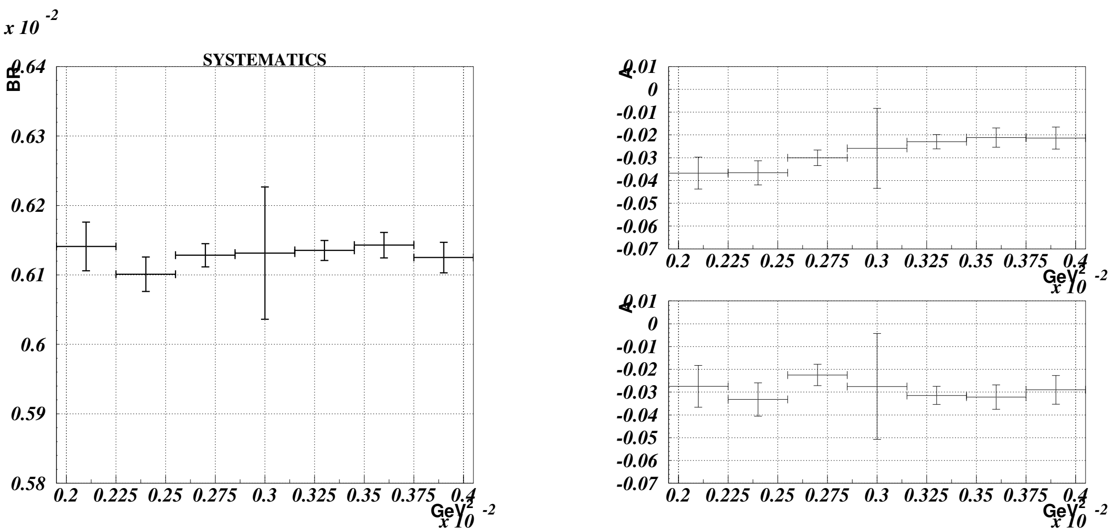

Figure 8.7: BR and A_ξ variation as a function of missing mass squared cut. The nominal value ($|M_\nu^2|$ <0.003 GeV^2/c^4) is reported with the statistical error, while only uncorrelated errors are reported for varied cut.

separately and found to be compatible within less than one standard deviation. The two results were initially $\sim 2\sigma$ far away: this triggered some checks, which led to a better tuning of the MC sample and, as a consequence, to a correction in the acceptance computation [54]. After this correction the two computed BR's are consistent within the statistical error:

$$BR(Ke3\gamma)^+/BR(Ke3)^+ = (6.12 \pm 0.12) \cdot 10^{-3} \tag{8.2}$$

$$BR(Ke3\gamma)^-/BR(Ke3)^- = (6.15 \pm 0.15) \cdot 10^{-3} \tag{8.3}$$

The BR was also computed on a run-by-run basis for positive and negative events, in order to check if the results were compatible within the statistical error: they are

Charged Vertex position lower cut			
Cut (cm)	$\lvert\Delta \mathrm{BR}\rvert(\cdot 10^{-5})$	$\lvert\Delta \mathrm{A}_\xi^+\rvert(\cdot 10^{-2})$	$\lvert\Delta \mathrm{A}_\xi^-\rvert(\cdot 10^{-2})$
-2500	0.20	0.076	0.28
-2000	0.23	0.073	0.18
-1500	0.54	0.13	0.30
-500	0.87	0.10	0.29
0	1.48	0.32	0.41
500	0.46	0.42	0.47

Table 8.9: Differences of Ke3γ/Ke3 BR, A_ξ^+ and A_ξ^- from nominal values as a function of charged vertex position lower cut. Only varied cuts are quoted.

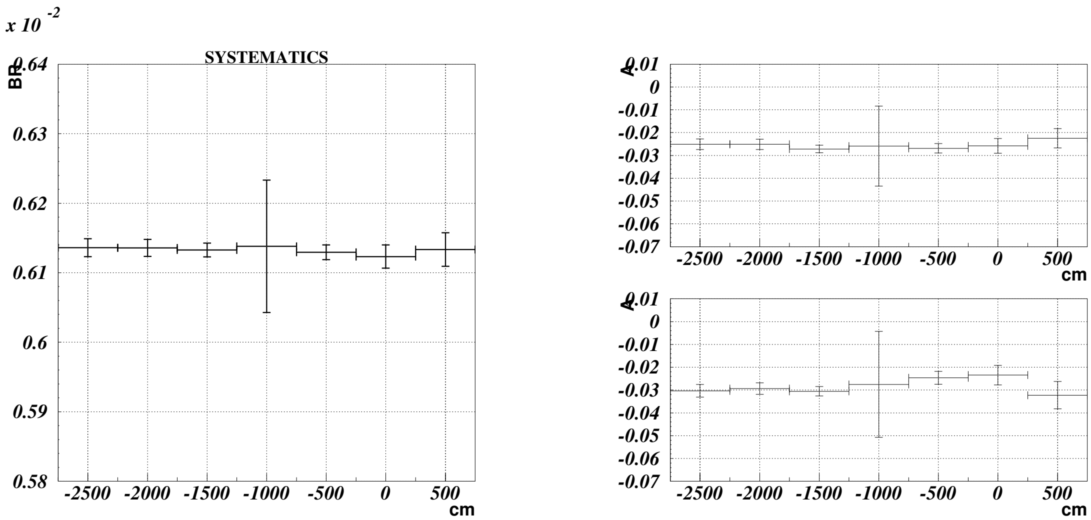

Figure 8.8: BR and A_ξ variation as a function of charged vertex position lower cut. The nominal value (> -1000 cm) is reported with the statistical error, while only uncorrelated errors are reported for varied cut.

plotted in fig. 8.12. A fit with a constant yields a reduced χ^2 of 1.115 for positive events and 0.944 for negative events.

8.5 R$^+$/R$^-$ measurement

As it was said before, during NA48/2 data-taking the achromat and DCH magnet polarities were frequently swapped in order to minimize possible systematic effects due to the detector asymmetries. In particular, the data analyzed in this work were collected keeping the achromat magnet fixed (so that positive and negative kaon beams always crossed different areas of the beam line), while the DCH magnet was

Charged Vertex position upper cut			
Cut (cm)	$\lvert\Delta\text{BR}\rvert(\cdot 10^{-5})$	$\lvert\Delta\text{A}_\xi^+\rvert(\cdot 10^{-2})$	$\lvert\Delta\text{A}_\xi^-\rvert(\cdot 10^{-2})$
5500	1.1	1.4	0.11
6000	0.39	0.80	0.38
6500	1.2	0.70	0.75
7500	2.2	0.090	0.033
8000	1.1	0.11	0.047

Table 8.10: Differences of Ke3γ/Ke3 BR, A_ξ^+ and A_ξ^- from nominal values as a function of charged vertex position upper cut. Only varied cuts are quoted.

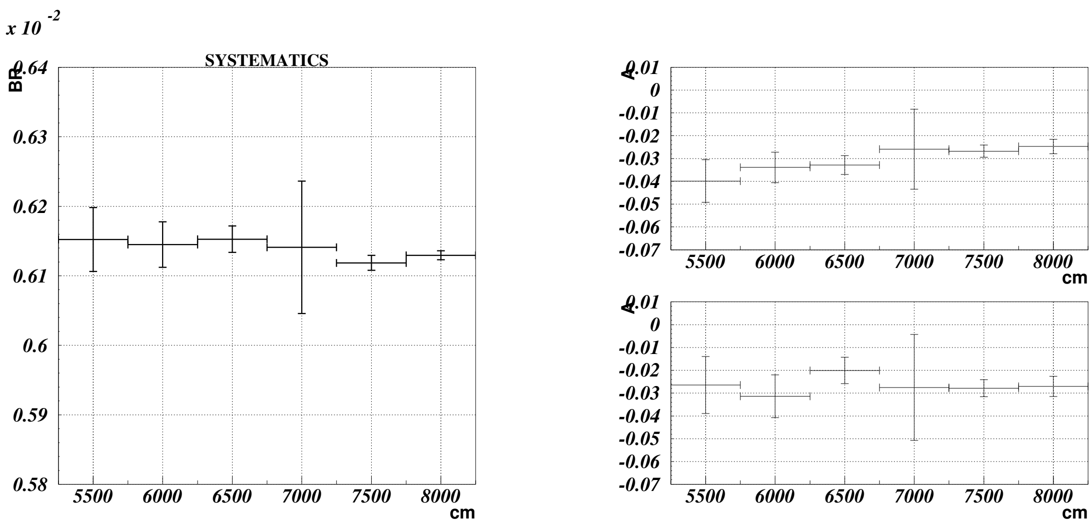

Figure 8.9: BR and A_ξ variation as a function of charged vertex position upper cut. The nominal value (< 7000 cm) is reported with the statistical error, while only uncorrelated errors are reported for varied cut.

swapped. This means that, given a magnetic field direction (e.g. "up"), positive events with magnetic field "up" ($\Uparrow$) and negative events with magnetic field "down" ($\Downarrow$) will go in the same side of the experimental apparatus. If one then computes:

$$\tau_1 = (R^+/R^-)_1 = \frac{BR(Ke3\gamma^+(\Uparrow))}{BR(Ke3^+(\Uparrow))} / \frac{BR(Ke3\gamma^-(\Downarrow))}{BR(Ke3^-(\Downarrow))} \tag{8.4}$$

$$\tau_2 = (R^+/R^-)_2 = \frac{BR(Ke3\gamma^+(\Downarrow))}{BR(Ke3^+(\Downarrow))} / \frac{BR(Ke3\gamma^-(\Uparrow))}{BR(Ke3^-(\Uparrow))} \tag{8.5}$$

their error, up to the first order, is not affected by systematic effects, since they cancel in the ratio. As a results, only statistical error can be considered when computing the total error. The ratio R^+/R^- is foreseen to be 1 within the SM.

Lower missing e-π^0 mass cut			
Cut (GeV^2/c^4)	$\lvert\Delta BR\rvert(\cdot 10^{-5})$	$\lvert\Delta A_\xi^+\rvert(\cdot 10^{-2})$	$\lvert\Delta A_\xi^-\rvert(\cdot 10^{-2})$
-0.0045	0.85	0.22	0.30
-0.0030	0.31	0.0.10	0.19
0.	1.4	0.37	0.016
0.0015	1.5	1.1	0.50

Table 8.11: Differences of Ke3γ/Ke3 BR, A_ξ^+ and A_ξ^- from nominal values as a function of missing e-π^0 mass lower cut. Only varied cuts are quoted.

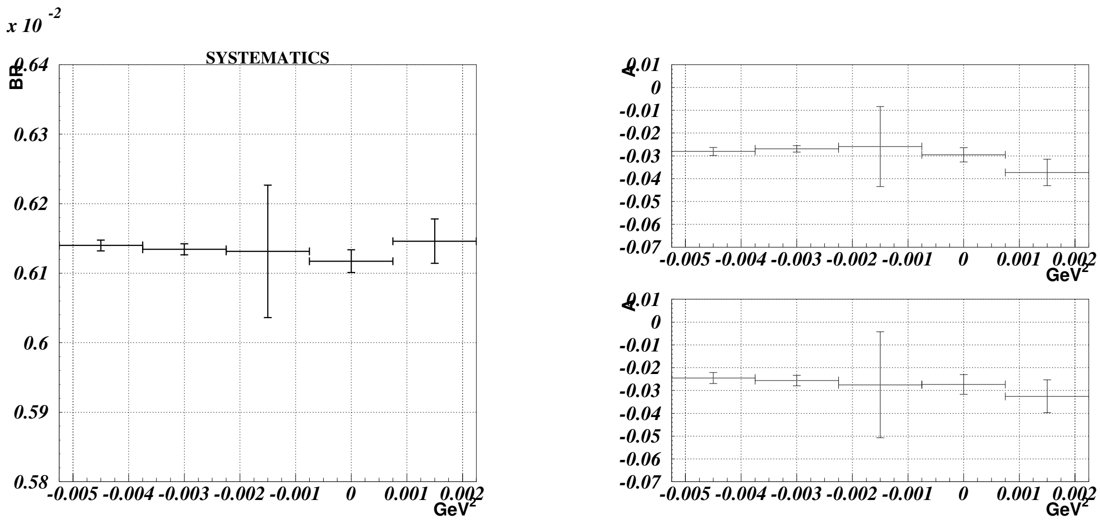

Figure 8.10: BR (left) and A_ξ (right, A_ξ^+ top, A_ξ^- bottom) variation as a function of missing e-π^0 mass lower cut. The nominal value (-0.0015 GeV^2/c^4) is reported with the statistical error, while only uncorrelated errors are reported for varied cut.

The numerical results computed for $\tau_{1,2}$ will be shown in the last chapter.

Upper missing e-π^0 mass cut			
Cut (GeV^2/c^4)	$\lvert\Delta$BR$\rvert(\cdot 10^{-5})$	$\lvert\Delta A_\xi^+\rvert(\cdot 10^{-2})$	$\lvert\Delta A_\xi^-\rvert(\cdot 10^{-2})$
0.015	2.9	0.033	0.55
0.016	1.4	0.096	0.75
0.018	1.7	0.49	0.28
0.019	2.0	0.62	0.27

Table 8.12: Differences of Ke3γ/Ke3 BR, A_ξ^+ and A_ξ^- from nominal values as a function of missing e-π^0 mass upper cut. Only varied cuts are quoted.

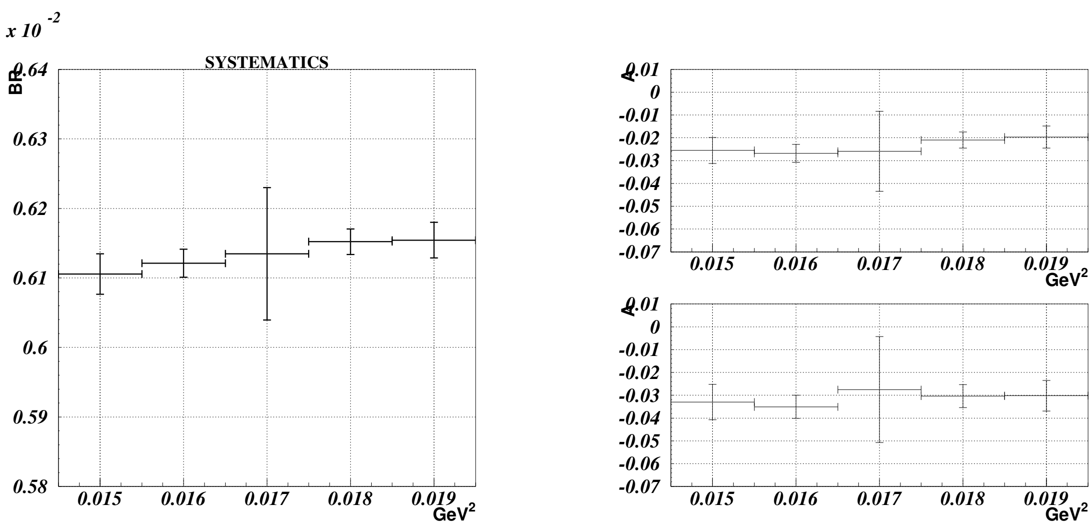

Figure 8.11: BR (left) and A_ξ (right, A_ξ^+ top, A_ξ^- bottom) variation as a function of missing e-π^0 mass upper cut. The nominal value (0.017 GeV^2/c^4) is reported with the statistical error, while only uncorrelated errors are reported for varied cut.

Cut	Associated Systematics	
	BR($\cdot 10^{-5}$)	$A_\xi(\cdot 10^{-2})$
Track momentum (upper)	2.8	0.71
Track momentum (lower)	5.9	0.82
Track position at DCH1	0	0.32
e-γ distance on LKr	3.2	0.77
Charged-neutral vertex distance	1.5	0.14
Cluster energy (lower)	6.6	0.65
Missing mass squared	3.0	0.8
Charged vertex (upper)	2.2	1.1
Charged vertex (lower)	0	0.15
e-π^0 missing mass (upper)	0	0.69
e-π^0 missing mass (lower)	0.85	0.70
E_{Lkr} >10 GeV (see Chapt. 7)	-	0.25
Q1 (see Chapt. 7)	-	0.15
Total	10.6	2.3

Table 8.13: Summary of systematics associated to Ke3γ/Ke3 BR, A_ξ^+ and A_ξ^- measurements.

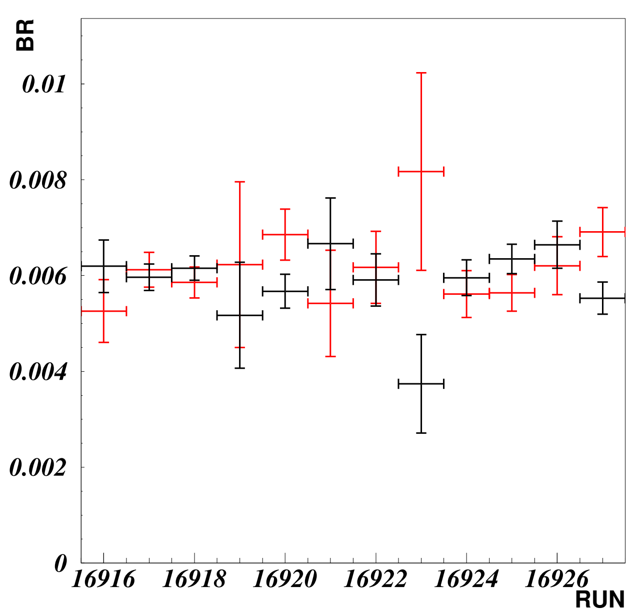

Figure 8.12: Ke3γ/Ke3 BR for each of the 12 analyzed runs (black for K^+, red for K^-).

Chapter 9

Results and conclusions

In the present work the measurement of the Ke3γ/Ke3 BR and of the T-violation probing parameter A_ξ was performed. The sample used represents the world's largest sample of Ke3γ events collected so far.

The BR result, including both positive and negative events, is:

$$R = (6.146 \pm 0.092_{(stat)} \pm 0.11_{(syst)} \pm 0.028_{(trig)}) \cdot 10^{-3} = (6.15 \pm 0.15) \cdot 10^{-3} \quad (9.1)$$

The theoretical result, computed in [28], is:

$$R = (6.40 \pm 0.08) \cdot 10^{-3} \quad (9.2)$$

The quoted error includes an upper limit on radiative and isospin breaking corrections, whose calculation was not explicitly performed in the cited paper. In figure 9.1 the BR measurement is compared to the theoretical result and to former experimental results (see Chapt. 1).

For what concerns the A_ξ measurement, as mentioned in Chapt. 1 the effect of a possible T violation can be seen by measuring the value of A_ξ for positive and negative events, provided one can precisely subtract non CP-violating ξ asymmetric effects. Otherwise the sum $A_\xi^+ + A_\xi^-$ only depends on CP-violating effects, other effects cancelling:

$$A_\xi^+ = (-2.7 \pm 1.8_{(stat)} \pm 2.3_{(syst)}) \cdot 10^{-2} = (-2.7 \pm 2.9) \cdot 10^{-2} \quad (9.3)$$

$$A_\xi^- = (-2.6 \pm 2.4_{(stat)} \pm 2.3_{(syst)}) \cdot 10^{-2} = (-2.6 \pm 3.3) \cdot 10^{-2} \quad (9.4)$$

$$A_\xi^+ + A_\xi^- = (-5.3 \pm 4.7) \cdot 10^{-2} \quad (9.5)$$

The only available measurement of the aforementioned is that of A_ξ^-, performed by ISTRA (see Chapt. 1).

For what concerns the quantities $\tau_{1,2}$, introduced in Chapt. 8, their measurements yield:

$$\tau_1 = 0.996 \pm 0.044 \qquad \tau_2 = 1.002 \pm 0.043 \tag{9.6}$$

Future possible developments include the analysis of 2003 and 2004 NA48/2 data in order to reach a precision on the BR measurement at the permille level (with respect to the present percent level) and to put more precise limits on the $A_\xi^\pm$ measurements. A higher statistics will also probably allow to better understand and reduce systematic uncertainties. Another possible issue to be addressed is the

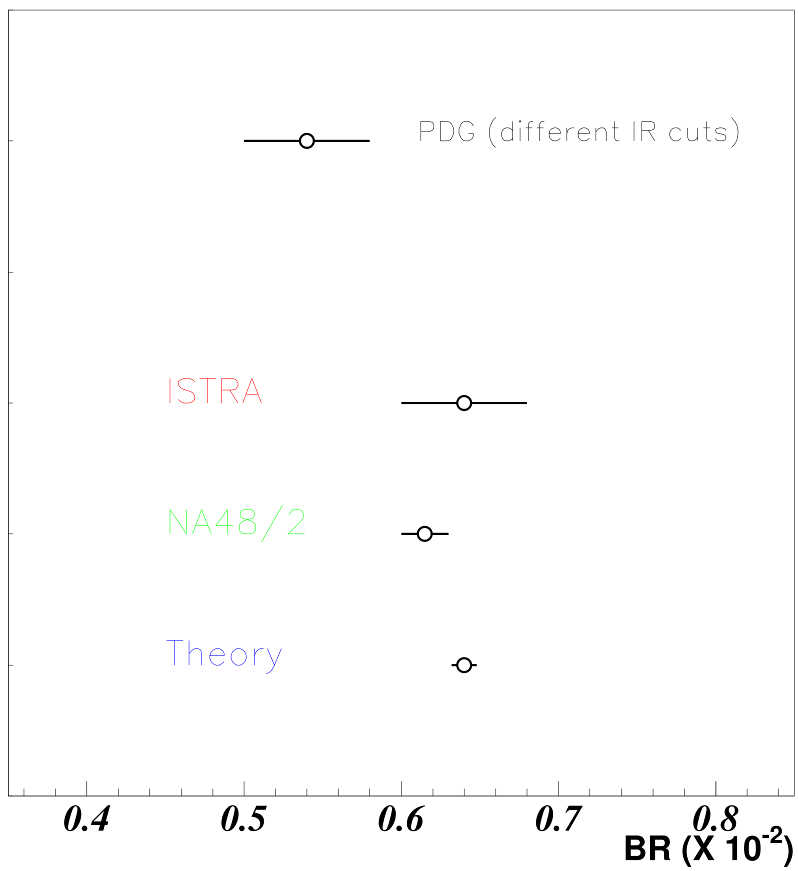

Figure 9.1: Ke3γ/Ke3 BR measurements and predictions. As stated in Chapt. 1 the PDG result is obtained for $E^*_\gamma > 10$ MeV and $0.6 < \cos\theta^*_{e\gamma} < 0.9$.

estimation of the DE component of the decay [28]: for this task, however, it is mandatory to analyze the full NA48/2 data-sample, given the smallness ($\simeq 1\%$) of this component with respect to the IB one.

Bibliography

[1] J.H. Christenson, J.W. Cronin, V.L. Fitch, R. Turlay, *Phys. Rev. Lett.* **13** (1964) 138-140.

[2] G. Barr et al., *Phys. Lett. B* **317** (1993) 233.

[3] J.R. Batley et al., *Phys. Lett. B* **544** (2002) 97-112.

[4] A. Alavi-Harati et al., *Phys. Rev. Lett.* **83** (1999) 22-27.

[5] B. Aubert et al., *Phys. Rev. Lett.* **93** (2004) 131801

[6] K. Abe et al., *Phys. Rev. Lett.* **93** (2004) 021601

[7] A.J. Buras, F. Schwab and S. Uhlig arXiv:hep-ph/0405132 (2004)

[8] T.D. Lee and C.N. Yang, *Phys. Rev.* **104** (1956) 254.

[9] C.S. Wu et al., *Phys. Rev.* **105** (1957) 1413.

[10] F. Mandl, G. Shaw *Quantum Field Theory*, pagg. 261-268.

[11] G. D'Ambrosio and G. Isidori, *Int.J.Mod.Phys.A* **13** (1998) 1-94.

[12] N. Cabibbo, *Phys. Rev. Lett.* **10** (1963) 531.

[13] S.L. Glashow, J. Iliopoulos and L. Maiani, *Phys. Rev. D* **2** (1970) 1285.

[14] M. Kobayashi, T. Maskawa, *Prog. Theory Phys.* **49** (1973) 652.

[15] J.J. Aubert et al., *Phys. Rev. Lett.* **33** (1974) 1404.

[16] J.-E. Augustin et al., *Phys. Rev. Lett.* **33** (1974) 1406.

[17] L. Wolfenstein, *Phys. Rev. Lett.* **51** (1983) 1945.

[18] Particle Data Group *Jour. of Phys.* **33** (2006).

[19] J.R. Batley et al., *Eur. Phys. Jour. C* **52** (2007) 875-891.

[20] E. Gàmiz, J. Prades, I. Scimemi, *JHEP* **10** (2003) 042.

[21] G. Fäldt, E. Shabalin, *Phys. Lett. B* **635** (2006) 295.

[22] J.R. Batley et al., *Eur. Phys. Jour. C* **54** (2008) 411-423.

[23] J.R. Batley et al., *Phys.Lett. B* **633** (2005) 173-182.

[24] J.R. Batley et al., *Eur. Phys. Jour. C* **50** (2007) 329-340.

[25] M. Raggi, PhD Thesis, University of Perugia (2006)

[26] L. Fiorini, PhD Thesis, University of Pisa & SNS (2005)

[27] A. Masiero, P. Paradisi, R. Petronzio, *Phys. Rev. D* **74** (2006) 011701.

[28] B. Kubis, E. H. Muller, J. Gasser, M. Schmid, *Eur. Phys. Jour. C* **50** (2007) 557-571.

[29] F.E. Low *Phys. Rev.* **110** (1958) 974.

[30] G. 't Hooft, *Phys. Rev. Lett.* **37** (1976) 8.

[31] M. Gell-Mann, *Phys. Rev.* **106** (1957) 1296.

[32] H. Georgi, A.V. Manohar, *Nucl. Phys. B* **234** (1984) 189.

[33] V. Braguta, A. Likhoded, A. Chalov, hep-ph/0105111 (2001).

[34] V. Braguta, A. Likhoded, A. Chalov, *Phys. Rev. D* **65** (2002) 054038.

[35] J. Gasser, B. Kubis, N. Paver, M. Verbeni, *Eur. Phys. J. C* **40** (2005) 205.

[36] B. Kubis, E. H. Muller, U.G. Meissner, *Eur. Phys. Jour. C* **48** (2006) 427-440.

[37] V. Braguta, A. Likhoded, A. Chalov, *Phys. Rev. D* **68** (2003) 094008.

[38] S.A. Akimenko et al., hep-ex/0510064 (2005).

[39] F. Romano et al., *Phys. Lett. B* **36** (1971) 525-527.

[40] D. Ljung et al., *Phys. Rev. D* **8** (1973) 1307-1330.

[41] V.N. Bolotov et al., *Sov. J. Nucl. Phys.* **44** (1986) 68.

[42] V.V. Barmin et al., *Sov. J. Nucl. Phys.* **53** (1991) 606-608.

[43] V. Fanti et al., *Nucl. Instrum. Meth. A* **574** (2007) 433-471.

[44] N. Angert Proc. Fifth CERN Acc. Phys. Course, CERN 94-01 (1994) 619

[45] B. Peyaud, *Nucl. Instrum. Meth. A* **535** (2004) 247-252.

[46] Y. Giomataris et al., *Nim* **376** (1996) 29.

[47] J. Derre, NA48 Internal Note 7 (2004).

[48] G. Unal, NA48 Internal Note 19 (2000).

[49] A. Bevan, B. Hay, NA48 Internal Note 17 (1998).

[50] PAW official webpage http://paw.web.cern.ch/paw/

[51] G. Unal, NA48 Internal Note 1 (1998).

[52] NA48 Internal Note 23 (2000).

[53] H. Leutwyler, M. Roos, *Z. Phys.* **C25** (1984) 91.

[54] Dmitri Madigozhin, Private communications.